DEVELOPMENT OF HYBRID PHOTONIC AND PLASMONIC LIGHT MANAGEMENT INTERFACES FOR THIN FILM SEMICONDUCTOR DEVICES

A THESIS SUBMITTED TO
THE GRADUATE SCHOOL OF NATURAL AND APPLIED SCIENCES
OF
MIDDLE EAST TECHNICAL UNIVERSITY

BY

HISHAM NASSER

IN PARTIAL FULFILLMENT OF THE REQUIREMENTS
FOR
THE DEGREE OF DOCTOR OF PHILOSOPHY
IN
MICRO AND NANOTECHNOLOGY

AUGUST 2015

Approval of the Thesis:

DEVELOPMENT OF HYBRID PHOTONIC AND PLASMONIC LIGHT MANAGEMENT INTERFACES FOR THIN FILM SEMICONDUCTOR DEVICES

submitted by **HISHAM NASSER** in partial fulfillment of the requirements for the degree of **Doctor of Philosophy in Micro and Nanotechnology Department, Middle East Technical University** by,

Prof. Dr. Gülbin Dural Ünver
Dean, Graduate School of **Natural and Applied Sciences**

Prof. Dr. Tayfun Akın
Head of Department, **Micro and Nanotechnology Dep., METU**

Prof. Dr. Raşit Turan
Supervisor, **Physics Dep., METU**

Prof. Dr. Macit Ahmet Özenbaş
Co-Supervisor, **Metallurgical and Materials Eng. Dep., METU**

Examining Committee Members:

Prof. Dr. Raşit Turan
Physics Dept., METU

Assoc. Prof. Dr. Alpan Bek
Physics Dept., METU

Assoc. Prof. Dr. Zaki M Saleh
Physics Dept., Arab American University

Prof. Dr. Oğuz Gülseren
Physics Dept., Bilkent University

Assoc. Prof. Dr. Cumali Sabah
Electrical and Electronics Eng. Dep., METU-NCC

Date: *31.08.2015*

I hereby declare that all information in this document has been obtained and presented in accordance with academic rules and ethical conduct. I also declare that, as required by these rules and conduct, I have fully cited and referenced all material and results that are not original to this work.

Name, Lastname: Hisham NASSER

Signature :

ABSTRACT

DEVELOPMENT OF HYBRID PHOTONIC AND PLASMONIC LIGHT MANAGEMENT INTERFACES FOR THIN FILM SEMICONDUCTOR DEVICES

Nasser, Hisham
Ph.D., Micro and Nanotechnology
Supervisor : Prof. Dr. Raşit Turan
Co-Supervisor: Prof. Dr. Macit Ahmet Özenbaş

August 2015, 171 pages

Hydrogenated amorphous silicon (a-Si:H) is a versatile and an attractive material of photovoltaics whose manufacturing has reached an immense and advanced level of maturity. Owing to its moderate conversion efficiency compared to its crystalline counterparts, it should target either power plants with miniature installation cost or applications with added value like building-integration. Since this photovoltaic technology is based on very thin films of a weakly light-absorbing material, light-management is, and always has been, a vital and indispensable aspect of the a-Si:H thin film solar cells technology. The highest conversion efficiencies of a-Si:H solar cells produced today basically involve light trapping approaches which employ randomly textured transparent substrate and a highly reflective rear contact. Obtaining new alternative approaches for light management in a-Si:H thin film solar cells is a great challenge. In this thesis, I propose to use plasmonic metal nanoparticles to enhance the light absorption in a-Si:H thin film solar cells.

In the first part of this thesis, I demonstrate fabrication of plasmonically active interface consisting of silver nanoparticles (AgNPs) embedded in aluminum doped zinc oxide (Al:ZnO) that has the potential to be used at the front surface and at the back reflector of a thin film solar cell to enhance light-trapping and increase conversion efficiency.

Then several single and double plasmonically active interfaces embedded in dielectric spacer thin films of different dielectric constant were successfully constructed and integrated to the front and at the rear device-quality a-Si:H thin films to investigate their light management potentials in terms of enhanced spectral dependence of photocurrent driven by a constant bias in the a-Si:H thin films use as indicators for an effective plasmonic effect. Single plasmonic interfaces exhibit plasmonic resonances whose frequency is redshifted with increasing particle size and with the thickness of a dielectric spacer layer. Double plasmonic interfaces consisting of two different particle sizes exhibit resonances consisting of double minima in the transmittance spectra. I investigate the enhancement of photocurrent in a-Si:H as a function of nanoparticle size and spacer layer thickness placed to the front and at the rear of the a-Si:H absorber. By comparing the photocurrent enhancement due to plasmonic interfaces integrated to the front and at the rear of a-Si:H thin films, we were able to judge that the true position of plasmonic AgNPs is at the rear of a-Si:H and with an optimum spacer layer of at most 30 nm thick film.

A new advanced light trapping concept is constructed for the first time. In this concept, I merge the scattering potentials of Al:ZnO surface texturing and AgNP plasmonics in a single light trapping interface. The results show that surface texturing by wet etching of Al:ZnO combined with AgNPs produces the highest optical extinction of a-Si:H thin film at the band edge and the measured photocurrent shows a clear increase not only at AgNPs resonance wavelength but over the entire wavelength range.

In parallel to the study related to the integration of plasmonic structures in a-SiH: thin films; the effect of SiO_2 spacer layer thickness on the optical response of AgNPs of potential integration in crystalline silicon solar cells has been investigated. By

carefully studying the thickness of the spacer layer, I have identified the critical thickness that defines the border between plasmonic and photonic regimes.

Keywords: silver nanoparticles, plasmonic resonance, aluminum doped zinc oxide, texturing, light tapping, thin film silicon solar cells, dewetting

ÖZ

İNCE FİLM YARI İLETKEN AYGITLAR İÇİN HİBRİD FOTONİK VE PLAZMONİK IŞIK YÖNETİMİ ARAYÜZLERİ GELİŞTİRİLMESİ

Nasser, Hisham
Doktora, Mikro ve Nanoteknoloji
Tez Yöneticisi : Prof. Dr. Raşit Turan
Ortak Tez Yöneticisi: Prof. Dr. Macit Ahmet Özenbaş

2015, 171 sayfa

Hidrojenlendirilmiş amorf silisyum (a-Si:H) üretim yöntemleri oldukça ileri düzeylere ulaşmış, fotovoltaik uygulamaların çok yönlü ve etkileyici malzemelerinden bir tanesidir. Kristal silisyum ile karşılaştırıldığında görece düşük olan verim değerleri nedeniyle a-Si teknolojisinin hedefinde düşük kurulum maliyetli enerji santralleri veya bina entegrasyonu gibi uygulamalar yer almaktadır. İnce film fotovoltaik teknolojisi ışık soğurumu oldukça zayıf olan çok ince filmler temeline dayalı olduğu için, ışığın uygun şekilde kontrol edilip kullanılabilmesi geçmişte olduğu gibi bugün de a-Si:H ince film güneş gözesi teknolojisinin çok önemli ve kaçınılmaz bir parçasıdır. Günümüzde en yüksek verim değerine sahip olan a-Si:H güneş gözleri, hem yüzeyinde rastgele dağılmış piramitler içeren optik geçirimli alttaşların hem de yüksek kırılma indisli arka kontakların olumlu etkilerini değerlendirmişlerdir. a-Si'da ışığın daha iyi kullanılabilmesi için yeni alternatif yöntemlerin geliştirilmesi büyük bir zorluktur. Bu tez çalışmasında a-Si:H ince film güneş gözelerinde ışık soğurumunun iyileştirilmesi için plazmonik metal nano-parçacıkların kullanılması önerilmiştir.

Tez çalışmasının ilk kısmında alüminyum katkılı çinko oksit (Al:ZnO) içine yerleştirilmiş gümüş nanoparçacıkların (AgNPs) oluşturduğu plazmonik olarak etkin

olan bir arayüz üretilmiştir. Bu yapı potansiyel olarak ince film güneş gözelerinin ön yüzeyinde ve arka yüzeyinde geri yansıtıcı olarak kullanım olanağına sahiptir.

Daha sonra, farklı dielektrik sabitlerine sahip farklı ince film ayırıcı tabakalar içine yerleştirilmiş çok sayıda tek ve ikili etkin arayüz başarıyla oluşturulmuştur. Bu arayüzler hem ön hem de arka yüzeyde kullanılan a-Si:H ince filmlerle tümleştirilmiş ve ışığın yüzeydeki davranışını nasıl etkilediği gözlemlenmiştir. Tek plazmonik arayüzler plazmonik çınlama frekanslarının kırmızıya doğru kaymasına sebep olur ve bu kayma miktarı, parçacık büyüklüğü ve dielektrik ayırıcı tabakanın kalınlığıyla orantılı olarak artar. İkili plazmonik arayüzler ise iki farklı parçacık boyutuna sahip olup, geçirgenlik tayfında ikili minimum noktası taşıyan çınlamalar sergilerler. Tez çalışmalarım kapsamında a-Si:H'dan elde edilen fotoakımda iyileşme gözlenmiş ve bu iyileşmenin nanoparçacık boyutuna, a-Si:H tabakanın ön ve arkasına yerleştirilen ayırıcı tabakanın kalınlığına bağlı olduğu anlaşılmıştır. Fotoakımlardaki iyileşmeleri kendi aralarında kıyaslayarak, a-Si:H'un arka tarafına yerleştirilen plazmonik gümüş nanoparçacıkların gerçek pozisyonlarına ve ideal ayırıcı tabaka olarak en fazla 30 nm kalınlığında film olması gerektiğine karar verilmiştir.

Çalışmalar süresince, yeni bir ileri seviye ışık hapsetme yöntemi geliştirilmiştir. Bu yöntemde, Al:ZnO rastgele piramitler oluşturulmuş yüzey yapısı ve Ag nanoparçacıkların ışığı saçma özellikleri tek bir arayüzde bir araya getirilmiştir. Sonuçlar göstermiştir ki Al:ZnO tabakasının kimyasal aşındırma ile şekillendirilip Ag nanoparçacıklar ile birleştirilmesi, a-Si:H ince filmin bant kenarında yüksek optik sönümlenime neden olmaktadır. Ayrıca, ölçülen fotoakım sadece Ag nanoparçacık çınlama dalga boyunda değil bütün dalga boyu aralığında belirgin bir artış göstermiştir.

Plazmonik nanoyapıların a-Si:H ince filmlerle tümleştirilmesi çalışmasına paralel olarak, SiO_2 ayırıcı tabaka kalınlığının kristal silisyum güneş gözelerine tümleştirilen Ag nanoparçacıkların optik tepkisi üzerindeki etkisi de incelenmiştir. Ayırıcı tabaka kalınlığının dikkatle çalışılmasından sonra, plazmonik ve fotonik rejimlerin birbirinden ayrıldığı sınırı tanımlayan kritik kalınlık tanımlanmıştır.

Anahtar kelimeler: gümüş nanoparçacıklar, plazmonik resonans, alüminyum katkılı çinko oksit, yüzey şekillendirme, ışığı hapsetme, ince film silisyum güneş gözeleri, topaklanma.

To my family

ACKNOWLEDGMENTS

First and foremost I offer my sincerest gratitude to my supervisor Prof. Dr. Raşit Turan for his encouragement, his inspiration, his understanding, and his knowledge whilst during my graduate academic life. I am also highly honored to be one of his PhD graduate candidates and for giving me the opportunity to be a member of GÜNAM family. I attribute the level of my PhD degree to his informative discussions, his creativeness, his positive attitude toward me, his patience, and the excellent guidance during my study. I have learned many things from him that have helped me in both my academic and my daily life.

It is a pleasure to offer my sincere thanks to all people who helped me to carry out this research.

I would like to thank Prof. Dr. Macit Özenbaş for having given me the opportunity to have him as my co-advisor for this research.

My deepest thanks belong to Associate Prof. Dr. Alpan Bek for his continuous encouragement and guidance throughout this research. Without his creativeness, his humor, his positive attitude, the several hours we spent together to improve the quality of publications or posters, his contagious passion for plasmonics and nano-optics, this research would be tough. He put me on the right track by the several hours he spent with me to introduce and discuss every aspect of the fascinating world of light trapping via plasmonic metal nanoparticles. You and all your efforts and support are not and for sure will never be forgotten!

I am highly grateful to Associate Prof. Dr. Zaki Saleh for his general interest in this work and for having carefully read and corrected this thesis and other manuscripts and proceedings. Illuminating discussions we had together and his many critics have had a great impact on the high quality of the work presented in this thesis. I have acquired many scientific capacities from him. I thank Dr. Zaki for his professionalism and his good mood every time I asked for help (very often, indeed!).

I would like to express my warm thanks to my loyal colleagues in the 'Thin Film Group'. Dr. Engin Özkol, a brother in Turkey no words can describe the friendship we developed during the last five years. We spent joyful time in GÜNAM and off campus. I thank him for his creative ideas both in academic and daily life, and his support to do most of the depositions needed for this work. His kind help to play the role of a Turkish-English translator and vice versa is greatly appreciated (Thank you!). Zeynep Demircioğlu was always very patient and kind. I also would like to thank her for the time she invested to format my thesis, which may be a burden for me without her help. It was nice to witness the birth of her cute little princess Arya in my last year of PhD studies. Dr. Tahir Çolakoğlu although joined the group lately, I am grateful to him for his presence and pieces of productive discussions. Lastly I wish to thank our ex-members Gizem Nogay and Burcu Barutçu.

I would like to thank my classmate and my friend Fırat Es not only for enduring me since 2004, but also his creative ideas, friendship and helping me with SiO_2 deposition needed for the thesis. Our friendship goes back to 2004, the year I started my academic life in ODTÜ.

I wish to express my deep thanks to Mona Zolfaghari Borra and Hande Çiftpınar for their support, kindness, understanding, and for having shared with me many nice moments of these last three years. Conducting research and discussions with Mona was amazing indeed. Hande Çiftpınar also helped me for the translation of the abstract in Turkish.

To would like to acknowledge my colleague Mete Günöven for having helped me at the sun simulator and for having shared his knowledge about optical measurements.

GÜNAM would be a monotonous research center without my dear friends and colleagues; Associate Prof. Dr. Mustafa Kulakçı for his good pieces of advices, Mehmet Karaman for his wonderful friendship, our pretty Gülsen Baytemir, Mustafa Ünal for sharing his knowledge in glass texturing and for AFM measurements, Yasin Ergunt for his kindness and friendly discussions, Yusuf Kasap for sharing his knowledge in colloidal nanoparticle lithography, Dr. Serim İlday, Serra Altınoluk, Ergi Dönerçark, Salar Habibpur Sedani, Özden Başar Balbaşı, Olgu Demircioğlu,

Çiğdem Doğru, Merve Pınar Kabukcuoğlu, Idris Candan, Dr. Mücahit Yılmaz, Makbule Terlemezoğlu, Emel Semiz, Gamze Kökbudak, İsmail Kabaçelik, Hasan Hüseyin Güllü, Seda Kayra Güllü, Arezoo Hosseini, Dr. Aydın Tankut, and Kurtuluş Abak. I am grateful to have them by my side during my study.

I am grateful to GÜNAM technicians; Yücel Eke, Nevzat Görmez, Tayfun Yıldız, Dursun Erdoğan for technical support and also to Harun Tanık, Tuncay Güngör and Buket Gökbakan for their support in administrative things in GÜNAM.

The financial support from the Scientific and Technological Research Council of Turkey (TUBITAK BIDEB-2215) is highly acknowledged.

It is impossible for me to forget my dearest friend Dr. Mohamad Al Zamil who introduced me to the mysterious academic life with all its complications even before starting my PhD studies. His creative plans and experience helped me much to organize my graduate studies. I am very thankful to Prof. Dr. Jihad Al Zaboat for his motivation and positive attitude. I am grateful to our intelligent mathematics doctors Fahd Jarad and Thabet Abdul Jawad. Their permanent success motivates me to catch up with their superior academic records. I wish to thank my cousin Mr. Mohamad Nasser, Mr. Mohamad Khalil, and Mr. Mohamad Al Kurd for their continuous support anytime needed. I acknowledge Ahmed Serdah for the professional help in Photoshop to draw some of the diagrams presented in this thesis.

Last but not the least I am endlessly grateful to my lovely family, my mother and my father in particular, for their unconditional love, understanding, endless support and encouragement during my 'long student' life. Special genuine thanks reward goes to my dearest brother Medical Doctor Mohamad Nasser and his handsome son, Majed, who has made my life fruitful and brilliant. Dr. Mohamad has always been supportive and has always given me superior pieces of advice and helped me to find my way. I would like to extend my thanks to my eldest brother Mr. Ahmad Nasser for his support, his positive attitude, and his wealth life experience he shared with me. I owe a debt gratitude to my brother Bilal. I never had the feeling of eeriness when he was here in Turkey. It is weird to miss my sweet sisters Hiyam, Ghada, Bushra, and Ghalieh for their warm feelings and tender.

TABLE OF CONTENTS

CHAPTERS

LIST OF TABLES

TABLES

LIST OF FIGURES

FIGURES

NOMENCLATURE

A	Absorption
a-Si	Amorphous silicon
a-Si:H	Hydrogenated amorphous silicon
AFM	Atomic Force Microscopy
AgNPs	Silver nanoparticles
Al:ZnO	Aluminum Doped Zinc Oxide
AM1.5	Air Mass 1.5
AP-CVD	Atmospheric Pressure Chemical Vapor Deposition
AuNPs	Gold nanoparticles
c-Si	Crystalline silicon
CVD	Chemical Vapor Deposition
E	Extinction
H	Haze
I_{SC}	Short circuit current
J	Current density
J_{SC}	Short circuit current density
LID	Light Induced Degradation
LP-CVD	Low Pressure Chemical Vapor Deposition
LSP	Localized Surface Plasmon
R	Reflectance

R_d	Diffuse Reflectance
SEM	Scanning Electron Microscope
Silicon nitride	Si_3N_4
Silicon dioxide	SiO_2
T	Transmittance
T_d	Diffuse Transmittance
TCO	Transparent Conductive Oxide
V	Voltage
μc-Si:H	Hydrogenated microcrystalline silicon

CHAPTER 1

INTRODUCTION

1.1 Silicon Solar Cells

Photovoltaics (PV) have shown a remarkable and ceaseless growth rate over the last decade and this technology has now surpassed 100 GW-peak of cumulative installed capacity around the world [1]. PV is accordingly well on its way to turning into a traditional wellspring of electrical power, with today's low module costs making it appealing to financial investors and private individuals. More than 90 % of today’s PV market share is dominated by silicon (Si) as shown in Figure 1.1 [2]. Today most industrially accessible solar cells are made of monocrystalline or polycrystalline silicon. Such solar cells can accomplish conversion efficiencies of up to 24.7 % for unconcentrated incident light [3]. However, this high conversion efficiency is offset by the high material and processing costs [2]. This is the basic drawback of crystalline and polycrystalline silicon solar cells.

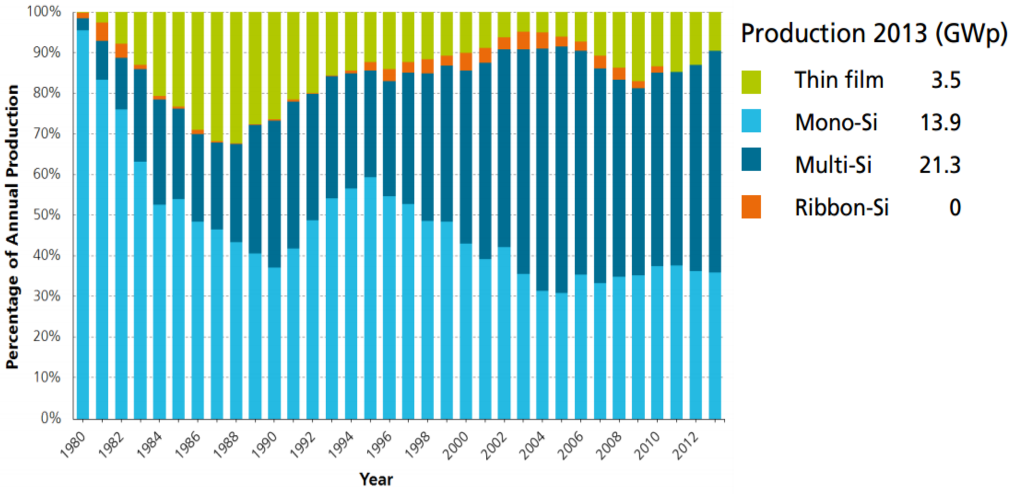

Fig. 1.1 PV annual production in the last two decades, Si based solar cells clearly dominates the market [2]

Following the time when photovoltaics were viewed as genuine methods for power generation, back in the mid-50s of the last century, concerns about the expense of crystalline silicon substrates motivated research in alternative options including thin films. After the interest of the CuS/CdS innovation, CdTe exploration began in the late 60s, followed by $CuInSe_2$ in 1975. Hydrogenated amorphous silicon (a-Si:H) entered the scene in 1976 following the critical breakthroughs of successful a-Si doping by Spear and Le Comber [4] and the first a-Si:H based solar cell by Carlson and Wronski [5]. Thin film silicon is along these lines the most youthful of "old" thin film advances. After the discovery of amorphous field effect transistors by Le Comber, Spear and Ghaith [6] and their subsequence use in liquid crystal displays, photovoltaics and flat panel displays drove the improvement of thin film silicon technology to new frontiers. The astounding in-door implementation of amorphous silicon solar cells made them a suitable option for pocket calculators that some of us still remember from the 80's of last century. Fabrication on larger areas empowered an economy of scale that made flat panel displays turn into a product all through the 90's. Later, in the 2000's, many suppliers of the display industry adjusted their large area tools for solar modules, motivating in the meantime new improvements in research, for example technologies for faster deposition of microcrystalline silicon or the utilization of doped SiO_x films for reduced parasitic absorption [7]. A depiction of the best in class is listed in Table 1.1.

Table 1.1 Highest stabilized efficiencies of state-of-the-art film silicon solar cells (certified, area ≥ 1 cm^2)

	V_{oc} (mV)	J_{sc} (mA.cm^{-2})	FF	ɳ
a-Si on transparent textured SnO_2:F by AIST [8]	896	16.36	69.8	10.22
mc-Si on an Ag back refector with a hexagonal pattern (AIST) [9]	535	29.07	73.1	11.37
Tandem on transparent textured B:ZnO by EPFL [10]	1382	12.82	73.3	12.63
Triple junction on textured/etched Al:ZnO by LG Electronics [11]	1963	9.52	71.9	13.44

Thin film silicon technology provides several advantages including: (i) raw material is abundant and non-toxic [12], (ii) very large, light-weight, flexible and low cost substrates maybe used [13], (iii) its uniform appearance is appropriate for building installation [14]. The improvement of silicon thin film reflects the significance of scalable technologies. Table 1.1 shows that the most research done is on devices with areas ~1 cm^2 though assembling devices in photovoltaics demonstrated plates with sizes somewhere around 1.4 to 5.2 m^2 and further scaling up to 9 m^2 has been used for displays [15]. The fundamental plasma processes are rather unique in their ability of applying just as well to small and large scale areas. Figure 1.2 shows the highest certified efficiencies of different types of solar cells and modules with respect to the reported active cell size [16]. Figure 1.2 also demonstrates the level of reliability and the maturity of silicon thin film solar cells [17].

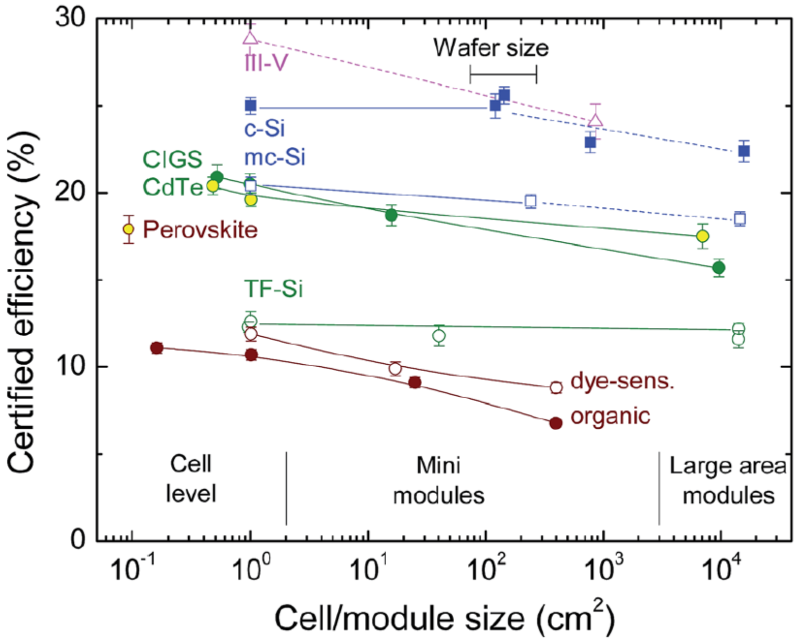

Fig. 1.2 Independently certified efficiencies of different PV technologies, plotted with respect to the cell or module size [16]

With the exception of thin film silicon, the module results of all PV technologies presented in Figure 1.2 are lower than the individual cell efficiencies.

Such a performance match between the cell level and module level is extremely crucial for large scale applications in order to ensure profitable and predictable yield levels. Yet, this is not the case in crystalline silicon as there are inevitable area losses between the wafers to accommodate for series connection and thermal expansion of the ribbons upon integration into modules. These losses are indicated with dashed lines in Figure 1.2. For thin film technologies, the difference between cells and mini-modules is basically constraint to the lost area due to series connection, yet it can likewise be because of the incompatibility of process ventures with large area fabrication, for instance spin coating or lithography. The variation between mini-modules and commercial-modules performance generally indicates the impact of spatial inhomogeneities of the assembly and manufacturing processes on large area. Figure 1.2 demonstrates that thin film silicon fares especially well in both regards; (i) advanced interconnection of individual cells by laser scribing minimizes the area losses, and (ii) scalability of plasma reactors and fabrication regimes brings out little contrasts between individual cell and module features. On module level, the efficiency variations to the crystalline silicon PV technologies, and certainly to the other settled thin film PV technologies, is consequently much less pronounced than that on the cell level.

Basically, thin film silicon solar cells built by hydrogenated amorphous and/or microcrystalline silicon (a-/μc-Si:H), have widely caught the interest of solar cell researchers and manufacturers due to low production cost. Thin film silicon solar cells offer the benefits of reduced materials usage (around 180-1000 nm thick silicon when compared to hundreds of microns for wafer-based solar cells), possibility of large-area fabrication with in line processing (commercial modules are up to 1 m^2 or even more) under moderate production temperatures (150-300 °C) that eliminates high production cost necessary for wafer based silicon modules. Moreover, such thin film modules provide the advantages of using various types of low-cost substrates starting from glass, stainless steel and even other flexible substrates as metal films and plastic [18]. It is worth mentioning that thin film modules are designed with cells connected in series which makes it feasible in terms of fabrication when compared to the external line contacts utilized in wafer-based modules that further reduces production cost.

So far, a-Si:H solar cells have relatively low stabilized conversion efficiency attributed to the light-induced degradation (LID) effect, also called as Staebler-Wronski effect (SWE) of the a-Si:H films. The latter is by far the most serious disadvantage threatening a-Si:H future in PV since LID decreases the initial cell efficiency by 30%. There are three methods of reducing LID; (1) deposition at higher temperatures and (2) hydrogen dilution and (3) deposition of thinner absorber layer to build a solar cell. State-of-the-art devices are produced with absorber layer thicknesses of ~200-300 nm with a stabilized efficiency up to ~90 % of the initial efficiency [19,20]. Photo-generated charge carrier transport in a-Si:H network and LID place an upper limit to the reasonable active layer thicknesses to the cell. However, these thicknesses are too small to allow sufficient absorption of red and infrared photons having energies close to the band gap (~1.65-1.9 eV). Thus, for higher stabilized efficiencies against LID [21,22], thin-film a-Si:H solar cells require efficient light-trapping schemes and increase optical thickness of the active layer without increasing the real thickness.

Finding new structural and/or optical concepts as ersatz approaches for light trapping in solar cells is a hot topic but a great challenge. So far, the most efficient a-Si:H and μc-Si:H solar cells recorded have a light trapping schemes consisting of a randomly textured transparent conducting oxide (TCO) substrate and a highly reflective back contact as shown in Table 1.1. With such light-trapping architecture, incident light scattered at the textured front TCO-silicon interface results in a prolonged absorption path in the active layer of the cell; the intrinsic a-Si:H or the intrinsic μc-Si:H. In other words, optical distance does exceed the active layer thickness and consequently results in an enhanced short circuit current (J_{sc}).

1.2 Literature Survey

Thin film solar cells have gone through a long history of development to improve the conversion efficiency and make it a more competitive source of renewable energy. Optimizing the properties of basic components has reached a fairly mature level, although drawbacks remain [22,23]. While further development in the basic components is still needed, there is a clear need to harvest more of the solar spectrum available. In fact, in a solar cell with a typical bandgap of ~1.8 eV, over 50 % of the solar radiation is transmitted through the cell that is unutilized [24]. Consequently, a great deal of today's research is focused on light management schemes to optimize light trapping and maximize absorption in the active layer. These schemes target almost total utilization of above-bandgap photons and more of the sub-bandgap ones. To maximize absorption, schemes involving cells with different bandgaps in tandem (or even more junctions) and nanostructured materials with variable bandgap have been implemented [25-27]. Efficient utilization of hot carriers through the so-called multiple exciton generation has also been reported [28,29]. Antireflections coating to minimize reflective losses [30], highly reflective back contacts [31], and using layers with matching refractive index to preferentially scatter light into the active layer [32] have all been used to optimize light absorption. However, many of these schemes involve high processing cost leaving a need for other less expensive light trapping schemes to improve efficiency at lower cost. Random pyramidal texturing in potassium hydroxide (KOH) solution commonly used in wafer-based processes, is incompatible with thin film solar cells because the pyramid size exceeds absorber film thickness and a-Si random network does not support the anisotropic KOH texturing [33]. For a-Si:H solar cell, development of alternative light-trapping schemes are therefore essential in capturing the red and near-infrared parts of the solar spectrum [34,35].

One common route to achieve light trapping in a-Si:H solar cell is utilization of rough surfaces. Rough surfaces for a-Si:H are obtained by texturing aluminum doped zinc oxide (Al:ZnO or AZO) in plenty of acidic solutions such as HCl, HNO_3, HF, and HN_4Cl, resulting in random textures with feature and size depending on used acid and on texturing time [36-38], nanoimprint lithography to obtain periodic Al:ZnO [39], utilizing natural textures of Al:ZnO deposited by CVD method (AP-CVD) [40], or by texturing the glass substrate prior to Al:ZnO deposition [41]. Several research groups have made use of rough Al:ZnO to enhance the short circuit current density (J_{sc}) of thin film silicon solar cells [42-44]. Incident light scattered at the rough Al:ZnO-Si interface increases optical path in absorber layer and thus enhances absorption. Randomly textured surface has the potential to increase path length and thus absorption of weakly absorbed photons by a factor of $4n^2$, where n is the refractive index of the absorber material [45]. The enhancement is around 50 for materials with high refractive index such as Si where the density of optical modes is much higher as compared to air. Accordingly, it scatters light forward for front textured Al:ZnO in superstrate configurations of the cell and backward for back reflector in substrate configurations into high index material resulting in large optical absorption enhancement.

More recently, considerable attention has been focused on plasmonic materials to improve the light-trapping efficiency, especially in thin film solar cells [46,47]. Light-trapping by plasmonic materials involves strong interaction of light with conduction electrons in metallic particles with appropriate size and shape integrated to the surface. Plasmonic interfaces consisting of metal nanoparticles (MNPs) placed at interfaces of two media with different dielectric constants or embedded in a dielectric medium have shown a promising potential for enhancing absorption and photocurrent in photovoltaic thin films and devices [46-49]. Using random arrays of silver nanoparticles, Pillai et al. demonstrated a 30 % increase in photocurrent across the solar spectrum in silicon/oxide solar cells [50]. Schaadt et al. obtained up to 80 % enhancement in photocurrent in the 500-nm spectral range using gold nanoparticles on doped wafer-based solar cells [51]. Stuart and Hall claim a factor of 18 enhancements in photocurrent around 800 nm by silver nanoparticle interface integrated to silicon-on-insulator photodetector [52]. Eminian et al. demonstrated a significant photocurrent enhancement in the 600–800-nm region in a-Si:H based n-i-p solar cell structures due to Au nanoparticles positioned at the rear interface of absorber layer [53]. Ho et al. integrated a double layer of gold nanoparticles to a-Si solar cell and obtained an improvement in efficiency by a factor of 18.4 % [54]. Table 1.2 summarizes the highest state-of-the-art efficiencies of thin film silicon solar cells with light trapping interface [21]. These reports illustrate the importance of light trapping interfaces in improving light absorption and consequently the efficiency of thin film solar cells.

Table 1.2 State-of-the art efficiencies of a-Si:H solar cell with light trapping interface

Thin film solar cell type	*V*oc (mV)	*J*sc (mA.cm^{-2})	FF	η	Thickness (nm)
Best reported devices, fabricated on natural TCO textures					
p-i-n/LP-CVD ZnO	885	17.94	71.92	11.4 ini	250
	877	17.28	66.6	10.1 st	
p-i-n/Asahi	901	16.55	75.7	11.3 ini	210
	906	16.05	69.5	10.1 st	
n-i-p/annealed Ag	992	14.65	73.0	10.6 ini	n.a
	965	14.36	67.2	9.3 st	
Best reported devices with plasmonic metallic nanoparticles					
n-i-p/textured reflector	810	15.1	64.5	9.4 ini	300
n-i-p/plasmonic reflector	810	14.8	65.2	9.3 ini	300
n-i-p/textured reflector	927	14.0	67.3	8.7 ini	200
n-i-p/plasmonic reflector	936	13.5	70.9	8.9 ini	200
Best reported devices on high aspect ratio nanowires					
n-i-p/Ag-coated nanowire	893	13.9	65.9	8.2 ini	90
i-n/p+ nanowires	796	15.4	62.9	7.7 ini	100
	782	14.9	62.2	7.2 st	
Best reported devices on moderate aspect ratio textures					
n-i-p/nano domes	955	14.9	68.1	9.7 ini	200
p-i-n/pyramids	913	17.1	69.7	10.9 ini	
p-i-n/nano spikes	866	14.7	65.9	8.4 ini	140
p-i-n reference	914	12.0	72.4	7.9 ini	
p-i-n/nano cavities	915	17.1	69.6	10.9 ini	200

CHAPTER 2

LIGHT MANAGEMENT APPROACHES

Light trapping, can be attained by structuring or texturing the cell surface to confine incident photons inside the semiconductor, thereby allowing for absorption over multiple passes as the case in pyramidal textured c-Si solar cells as shown in Figure 2.1. This is beneficial in terms of lowering material consumption by allowing photon absorption over multiple passes in a thin film rather than a single pass over a thick film. Light management is crucial for many commercial silicon solar cells. Crystalline Si cells exploit pyramidal wafer texturing to refract light from the surface facets into the absorbing bulk while a-Si:H solar cells employ random contact textures to enhance photon absorption. Light management considerations for thick wafers and thin film light trapping architectures are very different. For thick wafers, light management can be illustrated in terms of geometrical optics, while wave optics is needed to explain light trapping in thin films.

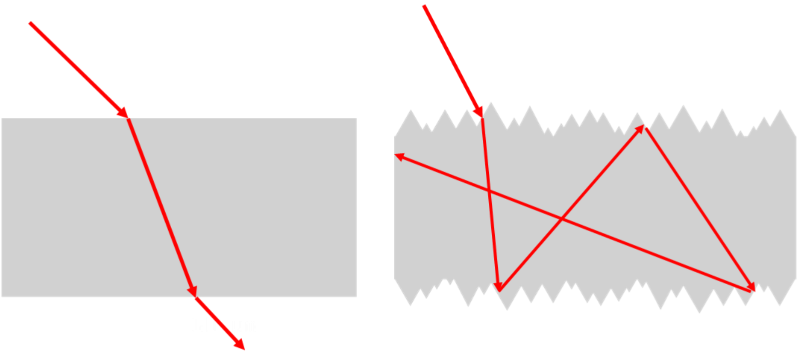

Figure 2.1 Single pass of incident light through planar silicon wafer (left) and multiple passes through textured silicon wafer (right)

2.1 Inspiration from c-Si Solar Cells

In crystalline silicon (c-Si) solar cells, elongating the light path in the absorber layer is attained by fabricating facets atop the surface of the wafers. Surface facets refract light into oblique angles [55] as shown in Figure 2.1 and Figure 2.2. For regular arrays of surface facets, Campbell and Green demonstrated an enhancement of up to 70-fold by applying ray tracing albeit for limited range of incident angles [33].

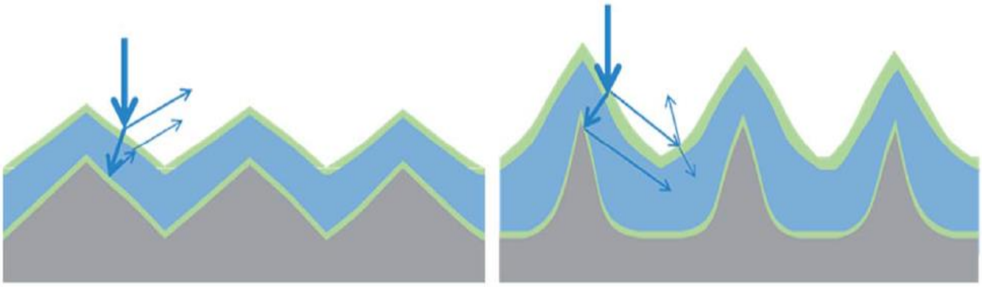

Fig. 2.2 Light scattering textures atop solar cells surface. Shallow textures are subjected to reflection losses (left) whereas high aspect ratio textures allow forward scattering with double incidence on the surface (right)

For random textures, Yablonovitch and Cody suggested a static treatment analogous to the equi-partition theorem, claiming that the intensity of weakly absorbed photon by the considered semiconductor becomes uniformly distributed among all modes within and outside the semiconductor [45]. They derived the $4n^2$ rule as a theoretical upper limit for path enhancement where n is the refractive index of the semiconductor considering the black body radiation mode-density [45]. This enhancement can reach a factor of 50 in the weakly absorbed photons in a material such as silicon which has high density of optical modes. As an expression of alert it ought to be specified that this determined theoretical limits are usually derived by expecting ideal structures with loss-free supporting layers, if any, ideal anti-reflection condition on the front and perfect back reflectors on the rear it is not possible to reach the $4n^2$ limit. For instance, for ideal structure as in PERL [56] and

HIT [57] solar cells the light path enhancement in the very weakly absorbing portion is close to 25 and 30, respectively, rather than 50.

The high price of silicon wafer itself is the prime reason that makes c-Si solar cells costly. Thus to reduce the cost per watt of c-Si solar cells and make a breakthrough in solar cell market, research is targeting ultra-thin c-Si with material thickness ranging between 1-2 µm, that can be fabricated on cheap module-sized substrates such as stainless steel, glass, or plastics [58-60]. Figure 2.3 presents the typical AM1.5 solar spectrum along with a curve that shows the fraction of incident light is absorbed by a 2-µm thick c-Si material on a single pass. It is clear that a large fraction of the solar spectrum is barely absorbed especially in the intense 600-1100 nm spectral range that illustrates the need to use thick c-Si wafers (180-300 µm) [49]. Indeed, high efficiency c-Si solar cells must have minority carrier diffusion lengths much longer than wafer thickness so that all photogenerated carriers can be collected. This requirement is most effectively met for thinner cells leading to a reduced cost. However, in thin c-Si, light trapping becomes a big challenge when working in 1-2 µm thickness range. KOH pyramidal texturing usually results in forming pyramids with size ~10 µm which exceeds the material thickness while structuring c-Si surface with shallower textures results in reflection losses (Figure 2.2, right).

For conventional thick wafer based c-Si solar cell, back reflectors absorb ~5% of the light it receives after transmission through the cell. Furthermore, around 40% of the long weakly absorbed wavelength reflected light from the rear surface of the cell escapes from the front textures after a double pass [61]. To reduce parasitic absorption induced by the rear, it is essential to replace conventional aluminum (Al) contact by a better reflector such as gold (Au) or cupper (Cu) [62]. Losses arising from light escaping through the front can be reduced by integrating more efficient large angle scatter at the rear. The latter can be achieved by means of plasmonic metal nanoparticles (MNPs). In this case, it is possible to maximize scattering beyond semiconductor escape cone allowing total internal reflection condition and thus increasing the optical path length across the solar cell.

In this thesis, the effect of SiO_2 dielectric spacer layer on the excitation of LSP resonance of AgNPs for potential integration in c-Si solar cells will be discussed.

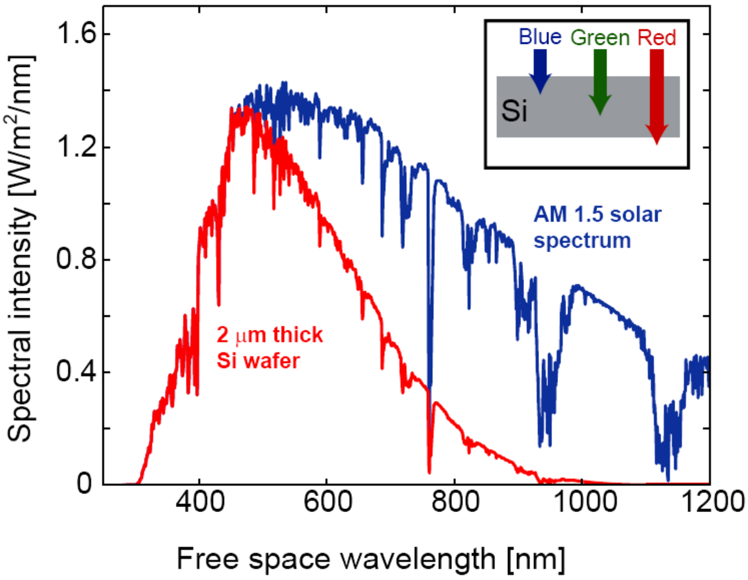

Fig. 2.3 AM 1.5 solar spectrum (Blue) and solar radiation absorbed in 2 µm c-Si thin film, assuming single pass (Red)

2.2 Light Management in Silicon Thin Film Solar Cells

In this thesis, we discuss ways to realize efficient light-trapping designs for silicon thin film solar cell based on a-Si:H absorber layer by using textured TCO and/or plasmonic metal nanoparticles.

2.2.1 Textured Transparent Conductive Oxide (TCO)

Other than low optical parasitic absorption and low electrical sheet resistance, the TCO must afford additional optical capacities that absolutely include (i) reduced light reflection due to refractive index grading which is applicable to the entire wavelength range, and (ii) light scattering and subsequent light trapping in the Si absorber which applies to the weakly absorbed red and infrared light that is transmitted through the cell to the back electrode. This effect is crucial for silicon thin film solar cells, and particularly for µc-Si cells that are preferentially utilized in a-Si/µc-Si micromorph cell design. Light trapping incorporating light scattering interface was demonstrated as early as 1983 by Deckman et al. [63] and light management became an indispensable part of silicon thin film solar cells in the following years. Both optical properties of TCO are achievable via adequate surface texture of the TCO with feature sizes comparable to the wavelengths of interest (divided by the refractive index of the Si absorber layer). As already mentioned in section 1.2, TCO surface texture is usually achieved either during TCO contact deposition, i.e. natural textures, or it is achieved by a chemical texturing process in diluted acid solution after deposition. Depending on these two routes of surface texture, there are two main types of textures: (i) natural pyramids occurring on as-deposited films, such as B:ZnO fabricated by low pressure chemical vapor deposition (LP-CVD) [64], or SnO_2:F deposited by AP-CVD [40] and (ii) craters-like features, formed by wet chemical texturing of sputter-deposited Al:ZnO to generate desired textures [36-38]. From these three different materials, only SnO_2:F can be fabricated both on-line and off-line, while the ZnO materials are always produced off-line. Off-line production affords the opportunity to choose required glass type as well as glass thickness, but it is generally less cost-effective [19]. Figure 2.4, left and right SEM images show examples of natural pyramids and crater-like textures, respectively [21].

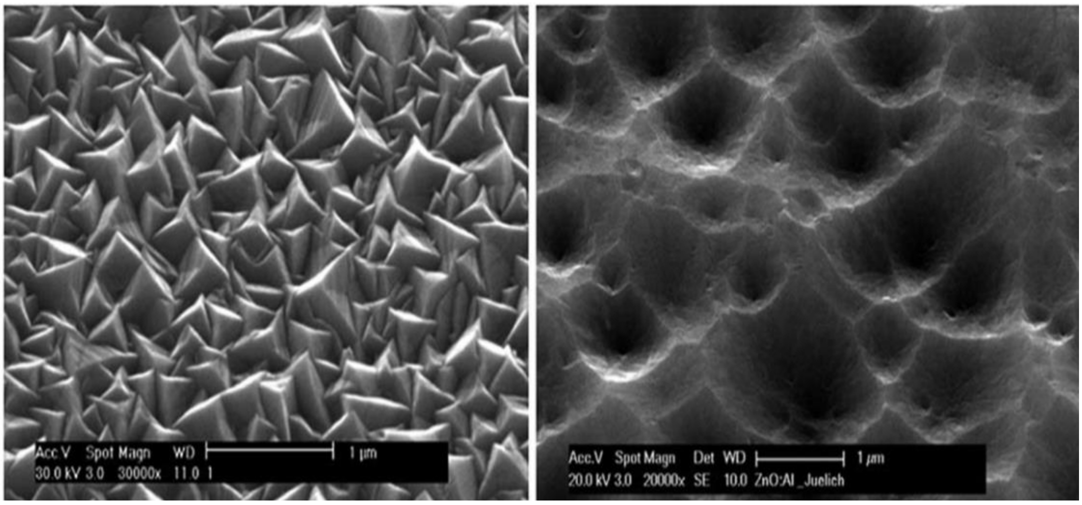

Fig. 2.4 Surface morphologies of B:ZnO deposited by LP-CVD (left) and Al:ZnO textured in diluted HCl (right)

All these TCO textures have randomly distributed features on the surface and their size is comparable to the wavelength of longer weakly absorbed photons by Si absorber. Therefore, incident light is subject to scattering but not to reflection or diffraction at well-defined interfaces. Without going into further details on the fundamental scattering mechanisms of incident light, TCO surface textures are usually characterized by the following two basic quantities [19]:

(i) Root mean square surface roughness (δ_{rms}), is a measure of vertical variations on textured surface. δ_{rms} gives no information regarding horizontal variations thereby it gives information neither about feature heights distribution nor about feature lateral spacing. δ_{rms} is defined as:

$$\delta_{\mathrm{rms}} = \left\{ \frac{1}{L} \int_{0}^{L} [y(x)]^2 \mathrm{dx} \right\}^{\frac{1}{2}} \qquad \text{Eqn (2.1)}$$

where $y(x)$ is defined as the deviation from an average profile height at a position x on the considered surface along the linear surface profile having a length L.

(ii) Transmittance haze or simply haze (H) is an optical measure of surface roughness. Haze is defined as the ratio of the fraction of light diffusely transmitted (T_d) to total transmitted light (T).

The two TCO surface textures characteristic quantities, δ_{rms} and H; are correlated in case of pyramid- and crater-like textures, with some experimental uncertainties as shown in Figure 2.5 [65].

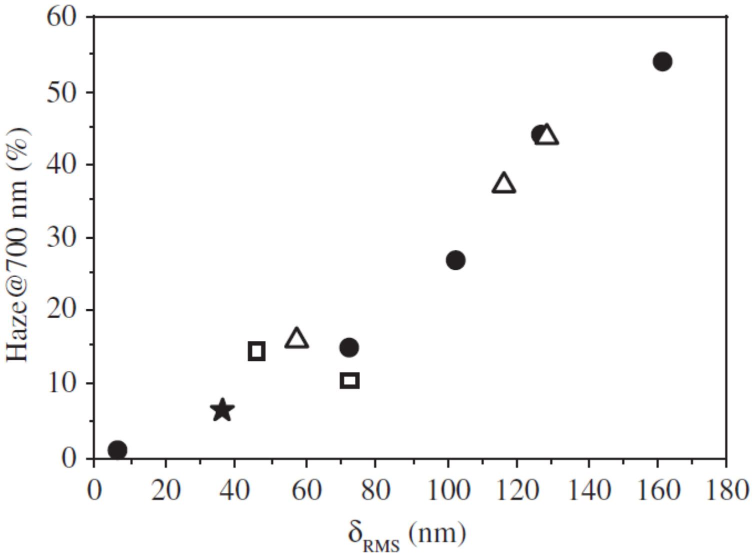

Fig. 2.5 Haze (H) at 700 nm and δ_{rms} for roughened TCO prepared differently [65]

Haze (H) is theoretically wavelength dependent, for a considered root mean square roughness; and this dependency can be expressed by a scalar scattering theory for scattering from TCO, with crater-like textures; to air [66]

$$H = 1 - \exp([-(4\pi C\delta_{\mathrm{rms}}(n_{\mathrm{TCO}} - n_{\mathrm{air}})/\lambda)^2]) \qquad \text{Eqn (2.2)}$$

$C = 0.5$ is an empirical constant. For TCO with pyramid-like textures the λ^2 dependence is replaced by phenomenological λ^3. Figure 2.6 demonstrates experimentally this wavelength dependence for crater- and pyramid-like textures of TCO with identical δ_{rms} of 55 nm [67]. This difference in wavelength dependence of the haze for different types of textures is a clear indication that TCO surface texture cannot be described solely by a single statistical parameter (δ_{rms}).

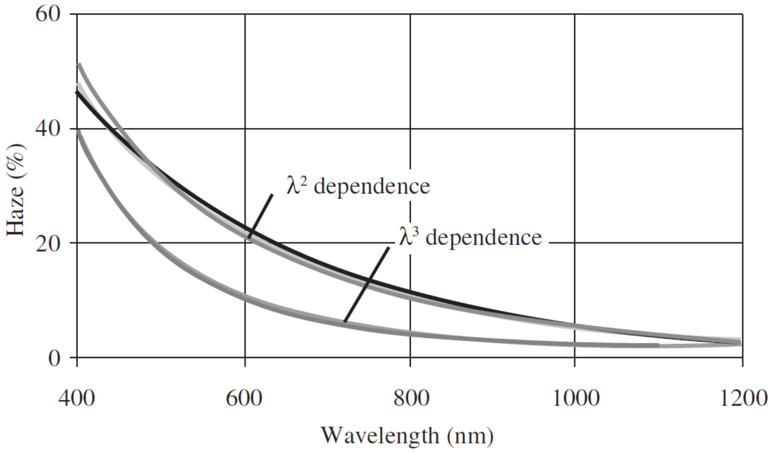

Fig. 2.6 λ^2 and λ^3 wavelength dependencies of haze for crater- and pyramid-like TCO textures, respectively [67]

The effects of textured TCO (high haze) in complete cells as compared to flat TCO (low haze) are shown in Figure 2.7 by analyzing the light reflected from cell structures for different spectral regimes [68].

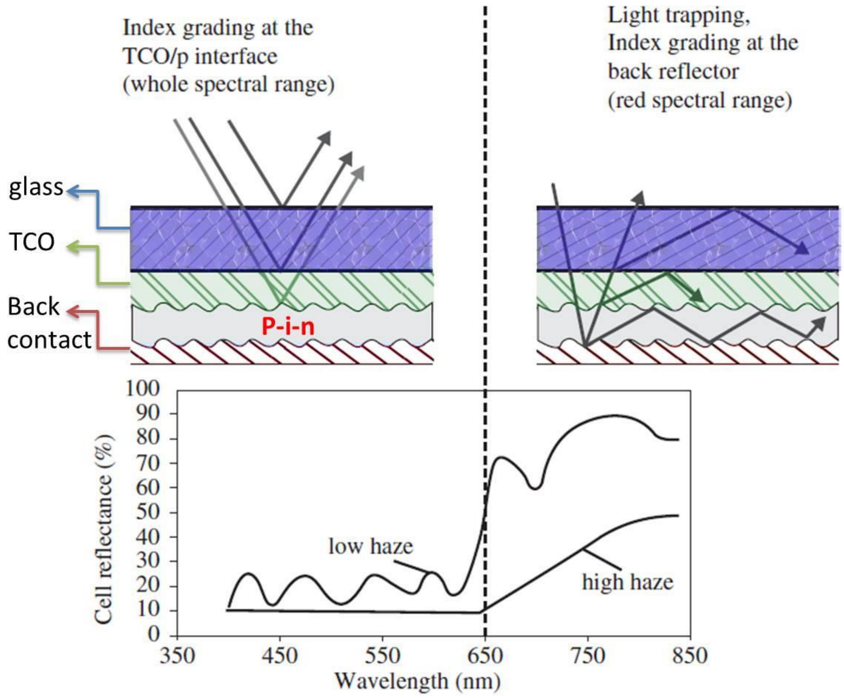

Fig. 2.7 Reflectance from cells with low and high haze TCO. Measurement was performed by illuminating the glass side, in the glass/TCO/p–i–n/back contact design [68]

Cell reflectance is reduced throughout the entire spectrum for high haze TCO. For cell fabricated atop high haze TCO, lower total reflectance at shorter wavelengths can be attributed to index gradient resulting from the roughness interface of the front TCO/*p*-layer. For weakly absorbed red and near infrared photons, a substantial fraction is reaching and reflected from the back contact. Compared to cells with lower haze TCO, the large reduction in reflected portion in cells with higher haze TCO stems from a double effect of both (i) index gradient occurring also at the rear and (ii) light trapping. The index grading at the rear *n*-layer/back contact occurs because front glass/TCO textures are easily replicated at the *n*-layer/back contact leading to reduced reflectance. Light trapping arises from the roughness of front and rear interfaces and the total internal reflection at the various interfaces adjoining media of lower refractive indices such as the a-Si/TCO interface with typical refractive indices of ~ 3.8/1.9, TCO/glass interface with 1.9/1.5, and the glass/air interface with 1.5/1. From reflectance data alone; Figure 2.7, the contributions of rear reflectance and light trapping cannot be distinguished individually. The cell reflectance for weakly absorbed red and infrared light may be brought down by both means, namely the reduced reflectance at the index graded rear contact interface and/or by light trapping. The degree of either effect is highly related that is light trapping is enhanced dramatically by high reflectivity of the rear [68].

2.2.2 Plasmonic Metal Nanoparticles

Recently, integration of plasmonic MNPs integrated to solar cells has widely sparked the attention of many research groups, due to their superior optical properties [46-51]. The origin of their particular optical behavior was only understood in the mid of the 19th century by Faraday (1857) [69]. Later, in the 20th century, the optical response of a spherical nanoparticle interaction with an incoming electromagnetic wave was calculated by Mie (1908) [70]. Nowadays, vital new optical behaviors of the MNPs have been found. The possibility to modify their optical properties by changing their shape, size, and the refractive index of host environment are at the essence of the very great interest they cause [50,71]. The specific and particular optical properties of metal nanoparticles are due to the presence of an optical resonance in their scattering, absorption and extinction spectra, known as the localized surface plasmon (LSP) resonance [46-51, 72]. AgNPs or AuNPs embedded in a given dielectric material can result in a strong scattering of light at a particular wavelength [46-50,73]. For relatively small (< 20 nm) AgNPs and AuNPs in air the LSP is located in the blue at around 350 nm and in the green at around 520 nm, respectively [74]. This leads to yellowish coloring in air of small AgNPs and red coloring of the small AuNPs. Light trapping by mean of plasmonic metal nanoparticles involves strong interaction of incoming light with electrons in the conduction band in metallic particles incorporated in a solar cell. In this light trapping route, incident light triggers oscillations of the conduction electrons of MNPs placed at interfaces of solar cells. When the natural frequency of the collectively oscillating conduction electrons matches that of the incident light, LSP resonance occurs [72,73]. At LSP resonance, incident light is preferentially scattered by MNPs integrated in solar cell into the absorber layer and thereby improves J_{sc}.

Nanoparticles with sufficiently small diameter < 50 nm, the localized surface plasmon is accompanied by a significant enhancement of the electromagnetic field inside the nanoparticle and in the very close vicinity of it. Upon excitation, the conduction electrons inside the particle oscillate all in phase, resulting in a buildup of polarization charges on the metal nanoparticle surface. The polarization charges act as an effective restoring force; result in resonance occurring at a particular frequency that is the particle dipole plasmon frequency. Consequently, a resonantly enhanced field builds up inside the particle. The enhanced field is homogenous throughout the volume of the particle taking into account the very small particle limit. Thus a dipolar field outside the particle is produced leading to a strongly enhanced near field in the vicinity of the particle [75]. This enhance electromagnetic field is important for solar cell application as it can be utilized to confine the excitation light in the active layer of the thin film solar cell. The fact that the enhanced field is basically localized in the close vicinity of the metal particle, is a powerful technique to enhance light absorption and thus to reduce the active layer of solar cells. Recently, with the use of localized surface plasmon of metal nanoparticles with diameter < 50 nm, several authors have reported enhancements of photocurrent and thus enhancements of solar conversion efficiency of dye-sensitized and organic cells [75]. The enhancement of photocurrent is explained in terms of the following two mechanisms (a) an enhanced light absorption in the main absorber layer of the solar cell, due to an enhanced electromagnetic field in the vicinity of the nanoparticles exactly at the LSP resonance or (b) photoemission from the metal nanoparticles themselves to their surrounding material due to an enhanced electromagnetic field inside the metal nanoparticles.

The fundamentals of MNPs optical response under electromagnetic wave excitation will be presented by introducing a simple description of interaction of light with MNPs. Afterwards, quasi-static field approximation, valid for analyzing the optical response of MNPs having radius much smaller than the excitation wavelength, $R \leq 0.01\,\lambda$, will be described. With this approach, the condition to obtain LSP will be determined. Then, Mie theory will be introduced which can, as opposed to the quasi-static field approximation, be used for spherical MNPs of any size. In the last part of this section, the factors influencing LSP of MNPs will be discussed.

2.2.2.1 Simple Semi-Classical Approach

When the electromagnetic wave encounters a metal particle, it triggers an oscillation of the electronic cloud. The conduction electrons start to oscillate at certain optical frequency with respect to the positive charge of the lattice ions resulting in an oscillating charge at the surface of the particle as illustrated in Figure 2.8, for semi classical approach. This oscillating charge creates a restoring force inside the nanoparticle. When the frequency of incident light is in resonance with the eigen-frequency of the electron's collective oscillation (the conduction electrons inside the particle oscillate all in phase), even a small exciting field will induce a numerous oscillation. The resultant restoring force is basically determined by the particle size which identifies the separation between the surface charges, the polarizability of the conduction electrons and the polarizability of the surrounding medium. For MNPs much smaller than the incident electromagnetic wavelength, the oscillation surface charges create an alternating dipole that can be associated with strong field enhancements within the nanoparticle and in the very close vicinity of the particle. Thus nanoparticle acts as an "optical antenna".

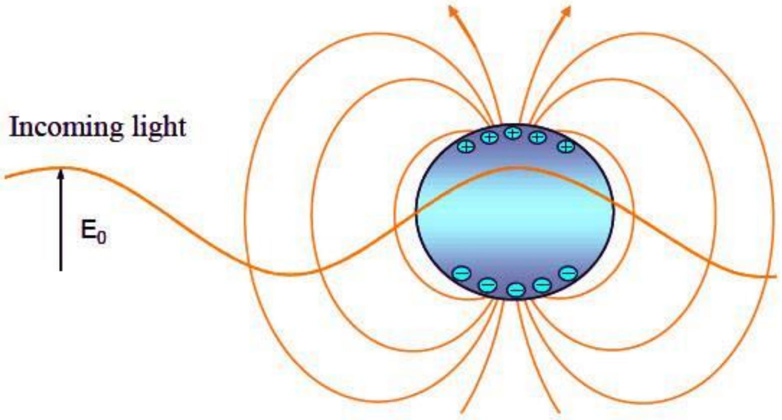

Fig. 2.8 Interaction of an electromagnetic wave with a spherical MNP in the semi-classical model

2.2.2.2 Quasi-Static Optical Response of a Small Sphere

The most feasible geometry to describe the optical response of a particle is by considering a homogeneous and isotropic sphere of radius R, where $R \ll \lambda$. In fact, when $R \ll 0.01\lambda$, the optical response of a particle can be computed in the quasi-static approach approximation. In quasi-static regime, a constant phase of the harmonically oscillating electromagnetic field is considered over the whole particle volume and only first order plasmon mode are examined. Thus, spatial field distribution can be calculated by simply considering the problem of a particle located in an electrostatic field. Harmonic time dependence can be added to the solution where the field distributions are known and the electrostatic field is considered to vary at a frequency equal to the frequency of incident light. For visible portion of incident light, the quasi-static regime refers to particles with radii of R below 5 nm [74]. On the other hand, for larger particle sizes, dynamic depolarization and radiation damping become important corrections to the quasi-static approximation and thereby, the interaction of the excitation light with the particle problem was treated by Mie theory. Furthermore, for larger particle sizes, the excitation higher-order plasmon modes have to be considered. Still, the quasi-static approximation has succeeded in describing the optical properties of particles of sizes less than 20 nm properly for various purposes [75].

2.2.2.2.1 Determination of the Localized Surface Plasmon Resonance of a Spherical Metal Nanoparticle

Consider a metallic sphere of radius $R = a \ll \lambda$ placed at the center of a uniform and static electric field, E_o; pointing along the z axis as shown in Figure 2.9. The embedding medium is non-absorbing and isotropic with a dielectric constant ε_m. The optical response of the metallic sphere can be described by the complex dielectric function $\varepsilon = \varepsilon_1 + i\varepsilon_2$, together with the complex index of refraction $n + ik = \sqrt{\varepsilon}$.

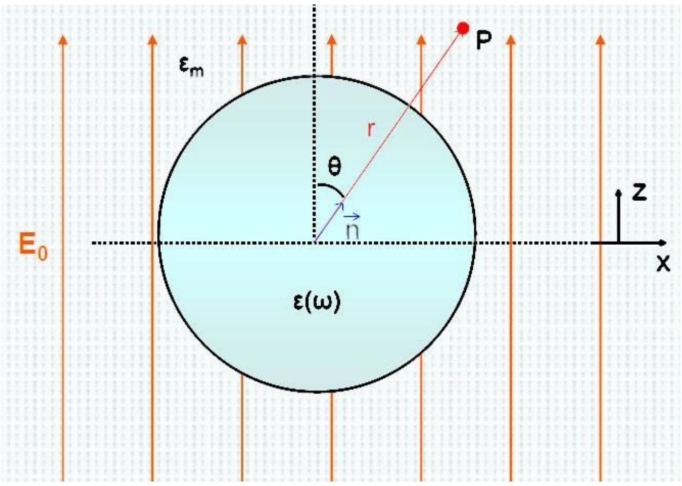

Fig. 2.9 Sketch of a homogenous metallic sphere in an isotropic medium interacting with an electrostatic field in case of quasi-static approximation

In electromagnetic theory, the electric field $\boldsymbol{E}$ is defined in terms of the electric potential $\boldsymbol{\phi}$ by

$$\boldsymbol{E} = -\boldsymbol{\nabla}\phi \qquad \text{Eqn (2.3)}$$

One of Maxwell's equations states that $\boldsymbol{E}$ satisfies

$$\boldsymbol{\nabla}.\boldsymbol{E} = \rho/\varepsilon_{\mathrm{o}} \qquad \text{Eqn (2.4)}$$

where ρ denotes the charge density. Thus, the electric potential $\boldsymbol{\phi}$ satisfies Poisson's equation

$$\nabla^2\phi = \rho/\varepsilon_{\mathrm{o}} \qquad \text{Eqn (2.5)}$$

In charge free region, $\rho = 0$ and Poisson's equation is reduced to Laplace's equation

$$\nabla^2\phi = 0 \qquad \text{Eqn (2.6)}$$

In electrostatic regime, Laplace's equation for the electric potential, Equation 2.6 is solved and the electric field is calculated using Equation 2.3. Due to azimuthal symmetry, the general solution of Laplace's Equation 2.6 is of the form [76]

$$\phi(r,\theta) = \sum_{l=0}^{\infty}\left[A_l r^l + B_l r^{-(l+1)}\right]P_l(\cos\theta) \qquad \text{Eqn (2.7)}$$

where $P_l(\cos\theta)$ are Legendre Polynomials of order l, and θ is the angle between the z-axis and the position vector **r** at an arbitrary point P as sketched in Figure 2.9. The constants A_l and B_l are determined by imposing boundary conditions that (i) the electric potentials remain finite at the origin and (ii) that the tangential and normal components of the electric potentials are continuous. The solutions of ϕ_{in} and ϕ_{out} designating the potentials inside and outside the sphere, respectively; can be written as follows

$$\phi_{\mathrm{in}}(r,\theta) = \sum_{l=0}^{\infty} A_l r^l P_l(\cos\theta) \qquad \text{Eqn (2.8)}$$

$$\phi_{\text{out}}(r,\theta) = \sum_{l=0}^{\infty}\left[B_l r^l + C_l r^{-(l+1)}\right]P_l(\cos\theta) \qquad \text{Eqn (2.9)}$$

The coefficients A_l, B_l, and C_l are determined from the boundary conditions as $r \to \infty$ and at the metallic sphere surface $r = a$. The first requirement that $\phi_{\text{out}} \to -E_{\text{o}}z = -E_{\text{o}}r\cos\theta$ as $r \to \infty$ dictates that $B_1 = -E_{\text{o}}$, while $B_l = 0$ for all $l \neq 1$. The other coefficients A_l and C_l are determined from the second bounday condition requirements at $r = a$. The tangantial compontents of the electric field are equal and thus

$$-\frac{1}{a}\frac{\partial\phi_{\text{in}}}{\partial\theta}\bigg|_{r=a} = -\frac{1}{a}\frac{\partial\phi_{\text{out}}}{\partial\theta}\bigg|_{r=a} \qquad \text{Eqn (2.10)}$$

and the normal components of the displacement of field are also equal, thus

$$-\varepsilon_{\text{o}}\varepsilon\frac{\partial\phi_{\text{in}}}{\partial\theta}\bigg|_{r=a} = -\varepsilon_{\text{o}}\varepsilon_{\text{m}}\frac{\partial\phi_{\text{out}}}{\partial\theta}\bigg|_{r=a} \qquad \text{Eqn (2.11)}$$

These two boundary condition requirements result in $A_l = C_l = 0$ for all $l \neq 1$, and from the evaluation of the remaining A_l and C_l, the electic potentails are [76]

$$\phi_{\text{in}} = -\frac{3\varepsilon_{\text{m}}}{\varepsilon + 2\varepsilon_{\text{m}}}E_{\text{o}}r\cos\theta \qquad \text{Eqn (2.12)}$$

$$\phi_{\text{out}} = -E_{\text{o}}r\cos\theta + \frac{\varepsilon - \varepsilon_{\text{m}}}{\varepsilon + 2\varepsilon_{\text{m}}}E_{\text{o}}a^3\frac{\cos\theta}{r^2} \qquad \text{Eqn (2.13)}$$

The electric potential ϕ_{out} in Equation 2.13 represents the superposition of the applied electric field E_{o} and that of a dipole at the center of the metallic particle and can be written by inserting the dipole moment **p** as

$$\phi_{\text{out}} = -E_{\text{o}}r\cos\theta + \frac{\mathbf{p}.\mathbf{r}}{4\pi\varepsilon_o\varepsilon_{\text{m}}r^3} \qquad \text{Eqn (2.14)}$$

$$\mathbf{p} = 4\pi\varepsilon_o\varepsilon_{\text{m}}a^3\frac{\varepsilon - \varepsilon_{\text{m}}}{\varepsilon + 2\varepsilon_{\text{m}}}\mathbf{E}_{\text{o}} \qquad \text{Eqn (2.15)}$$

It is seen that the applied electric field induces a dipole moment p inside the metallic sphere where the magnitude of p is proportional to $|\mathbf{E}_\mathrm{o}|$. By introducing the polarizability α defined as $\mathbf{p} = \varepsilon_o \varepsilon_\mathrm{m} \alpha \mathbf{E}_\mathrm{o}$, α can be written as

$$\alpha = 4\pi a^3 \frac{\varepsilon - \varepsilon_\mathrm{m}}{\varepsilon + 2\varepsilon_\mathrm{m}} \qquad \text{Eqn (2.16)}$$

α is the complex polarizability of a metallic nanoparticle with sub-wavelegnth diameter in an electrostatic regime which shows the same fundamental form as the Clausius Mossotti relation [76].

The electric field $\boldsymbol{E} = -\boldsymbol{\nabla}\phi$ can be computed by the potential in Equation 2.12 and Equation 2.13 for inside and outside the metallic sphere, respectively

$$\mathbf{E_{in}} = \frac{3\varepsilon_\mathrm{m}}{\varepsilon + 2\varepsilon_\mathrm{m}} \mathbf{E}_\mathrm{o} \qquad \text{Eqn (2.17)}$$

$$\mathbf{E_{out}} = \mathbf{E}_\mathrm{o} + \frac{3\mathbf{n}(\mathbf{n}.\mathbf{p}) - \mathbf{p}}{4\pi\varepsilon_o\varepsilon_\mathrm{m}} \frac{1}{r^3} \qquad \text{Eqn (2.18)}$$

where $\mathbf{n}$ is the unit vector in the direction of an arbitrary point P as shown in Figure 2.9. The obtained solutions are also valid for metal nanospheres located in oscillating electromagnetic fields in quasi-static approximation. In this approach, the nanospheres experiences spatially constant yet time dependent phase field. Still, the dielectric function of embedding medium ε_m is considered a real constant while the dielectric function of the metal nanosphere ε has to be replaced by its frequency dependent function, $\varepsilon(\omega)$. Both dipolar and internal electric fields experience a resonance, named as Localized Surface Plasmon (LSP) resonance also named as dipolar surface plasmon resonance under the condition

$$|\varepsilon(\omega) + 2\varepsilon_\mathrm{m}| = \text{minimum} \qquad \text{Eqn (2.19)}$$

Thus, a negative real part ε_1 is a must to achieve the LSP resonance which can be achieved for metals as shown in Figure 2.10, data taken from SEA, Semilab [77].

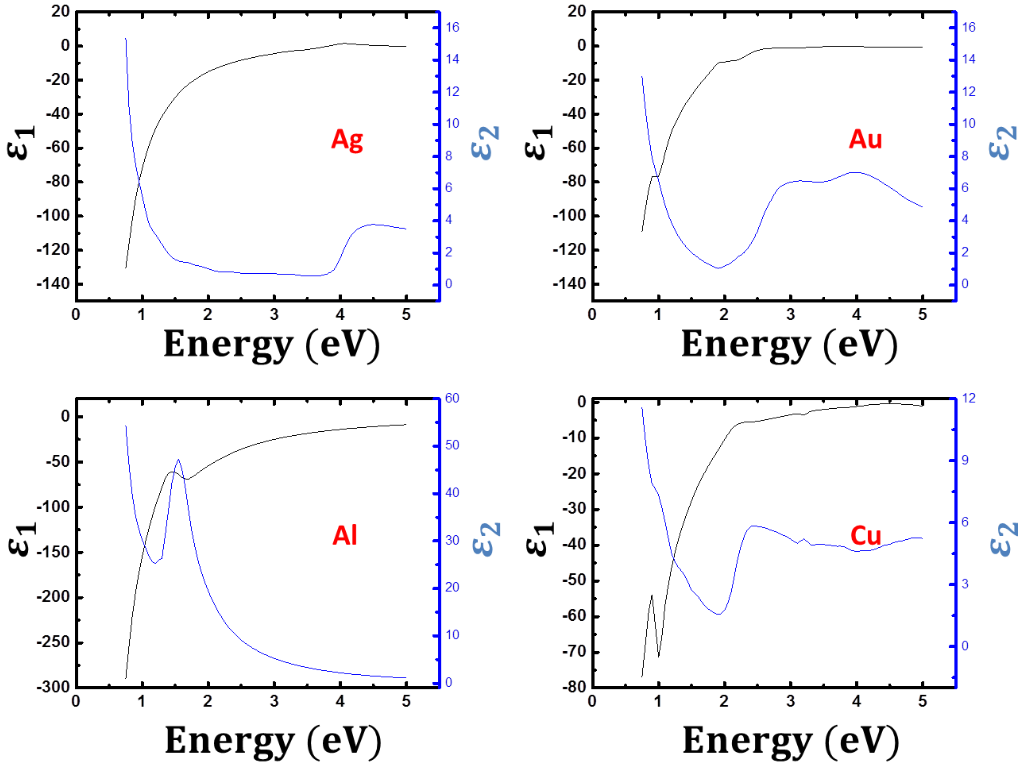

Fig. 2.10 Complex dielectric functions of (a) Ag, (b) Au, (c) Aluminum (Al), and (d) Cupper (Cu) with real part (ε_1) and the imaginary part (ε_2)

Equation 2.19 can be written as

$$[\varepsilon_1(\omega) + 2\varepsilon_\mathrm{m}]^2 + [\varepsilon_2(\omega)]^2 = \text{minimum} \qquad \text{Eqn (2.20)}$$

which for *small or slowly-varying* $\mathrm{Im}[\varepsilon]$ around resonance simplifies to

$$\mathrm{Re}[\varepsilon(\omega)] = -2\varepsilon_\mathrm{m} \qquad \text{Eqn (2.21)}$$

Relation 2.21 is known as Fröhlich condition and the associated mode (in case of oscillating field) is known as dipole surface plasmon (or LSP) of the metal nanoparticles.

In the case when $\mathrm{Im}\varepsilon(\omega) \neq 0$ or strongly varies close to resonance, the external and internal electric fields as well as the light absorption in the MNP at the LSP resonance will be limited by the partial vanishing of $|\varepsilon(\omega) + 2\varepsilon_{\mathrm{m}}|$.

Figure 2.11 shows the absolute value and phase of polarizability, α; as a function of frequency ω in electron volt (eV) for a dielectric constant varying as $\varepsilon(\omega)$ of the Drude form

$$\varepsilon(\omega) = 1 - \frac{\omega_{\mathrm{p}}}{\omega^2 + i\gamma\omega} \qquad \text{Eqn (2.22)}$$

where $\omega_{\mathrm{p}} = \frac{ne^2}{\varepsilon_0 m}$ is the plasma frequency of the free electron gas and $\gamma = 1/\tau$ is the characteristic collision frequency oscillating electrons in response to the applied electromagnetic field. The motion of these oscillating electrons is damped due to collisions occurring with this characteristic frequency γ. τ is the relaxation time of free electron gas [75]. n is the free electron density, e is the electron charge, and m is the electron effective mass. $\varepsilon(\omega)$ is taken as a Drude fit to the dielectric function of Ag given by Johnson and Christy [78].

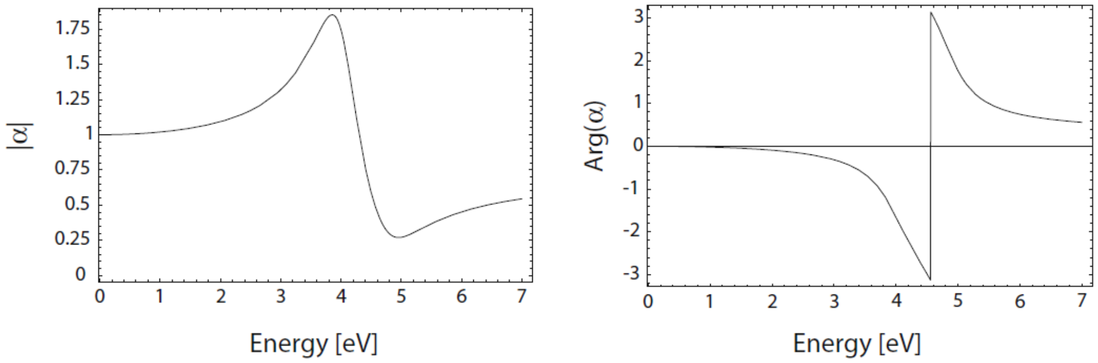

Fig. 2.11 Absolute value and phase of the polarizability of metal particle with sub-wavelength dimension as a function of the driving field energy

It is clear from Figure 2.11 that the polarizability α of Ag nanospheres is enhanced when the resonance condition in Equation 2.21 is satisfied. Under this condition, MNPs exhibit a strong increase in light absorption at LSP resonance. This increase in light absorption is usually accompanied with a sharp enhancement of the localized electric field inside as well as in the close vicinity of the MNP.

Fröhlich condition stated in Equation 2.21 addresses the strong dependence of the LSP resonance frequency on the embedding medium. An increase in ε_{m} will result in a red shift of the LSP resonance frequency. Therefore, MNPs are considered as ideal detector for optical sensing of changes in surrounding medium refractive index.

2.2.2.2.2 Electromagnetic Fields Radiated by a Small Metal Particle at its Plasmon Resonance

A small metal nanosphere with radius $R = a \ll \lambda$ can be treated as an ideal dipole in the above considered quasi-static regime approximation. Under plane-wave illumination characterized by $\mathbf{E}(\mathbf{r}, t) = \mathbf{E}_{\mathrm{o}} e^{-i(kr-\omega t)}$, the fields induce an oscillating dipole moment $\mathbf{p}(\boldsymbol{t}) = \varepsilon_{\mathrm{o}}\varepsilon_{\mathrm{m}}\alpha\mathbf{E}_{\mathrm{o}}e^{-i\omega t}$, where α is given by Equation 2.16. The radiation leads to scattering of the incident plane wave by the nanoparticle and can be represented as radiation by a point dipole. In the particle's vicinity $(kr \ll 1$, where $k = 2\pi/\lambda)$, the electric field of the electrostatic result in Equation 2.17 and Equation 2.18 can be written as [76]

$$\mathbf{E} = \frac{3\mathbf{n}(\mathbf{n}.\mathbf{p}) - \mathbf{p}}{4\pi\varepsilon_o\varepsilon_{\mathrm{m}}}\frac{1}{r^3} \qquad \text{Eqn (2.23)}$$

and the magnetic field is to

$$\mathbf{H} = \frac{i\omega}{4\pi}(\mathbf{n} \times \mathbf{p})\frac{1}{r^2} \qquad \text{Eqn (2.24)}$$

It can be noticed that the electric field given by Equation 2.23 is identical to the second term of the electric field presented in Equation 2.18. The fields are predominantly electric in the nearest zone of the particle since magnetic field is smaller than electric field by about a factor of $\sqrt{\varepsilon_{\mathrm{o}}/\mu_{\mathrm{o}}}\,(kr)$. The magnetic field vanishes in the case of static fields ($kr \to 0$). In the counter limit of the radiation zone (far field: $kr \gg 1$), the dipole fields are those of spherical-wave form

$$\mathbf{E} = \sqrt{\frac{\mu_o}{\varepsilon_o \varepsilon_m}} \mathbf{H} \times \mathbf{n} \qquad \text{Eqn (2.25)}$$

$$\mathbf{H} = \frac{ck^2}{4\pi} (\mathbf{n} \times \mathbf{p}) \frac{e^{ikr}}{r} \qquad \text{Eqn (2.26)}$$

2.2.2.2.3 Absorption, Scattering, and Extinction Cross Section of Small Metal Particle

From the viewpoint of optics, and for particles of all sizes, both scattering and absorption and thus Extinction ($E = \text{scattering} + \text{absorption}$) of the particle are indeed enhanced as a consequence of resonantly enhanced α at the LSP resonance [74], i.e. when the Fröhlich requirement in Equation 2.21 is met; and as expressed in Equation 2.27 and Equation 2.28 for scattering and absorption cross-sections, C_{sca} and C_{abs}, respectively. C_{sca} and C_{abs} of small nanoparticles are calculated via the Poynting-vector, $\mathbf{S} = \mathbf{E} \times \mathbf{H}$. Equations 2.23 and Equation 2.24 are used for $\mathbf{E}$ and $\mathbf{H}$, respectively [79].

$$C_{sca} = \frac{k^2}{6\pi} |\alpha|^2 = \frac{8\pi}{3} k^4 R^6 \left[\frac{\varepsilon - \varepsilon_m}{\varepsilon + 2\varepsilon_m}\right]^2 \qquad \text{Eqn (2.27)}$$

$$C_{abs} = k\text{Im}[\alpha] = 4\pi k R^3 \text{Im}\left[\frac{\varepsilon - \varepsilon_m}{\varepsilon + 2\varepsilon_m}\right] \qquad \text{Eqn (2.28)}$$

It can be seen from scattering and absorption cross-sections that for smaller nanoparticles with $R \ll \lambda$, the absorption efficiency dominates over the scattering efficiency since C_{abs} is proportional to R^3 while C_{sca} is proportional to R^6. At LSP resonance, the scattering cross-section can dramatically exceed the geometric cross-section of the MNP. For example, AgNP in air has an albedo; defined as the scattering cross-section over sum of scattering and absorption cross-sections, exceeding 0.9 [84]

For a spherical particle with volume V and optical dielectric function $\varepsilon = \varepsilon_1 + i\varepsilon_2$ in quasi-static regime approximation, the extinction cross-section, $C_{ext} = C_{sca} + C_{abs}$ is written as

$$C_{ext} = 9\frac{\omega}{c}\varepsilon_{\mathrm{m}}^{3/2}V\frac{\varepsilon_2}{[\varepsilon_1 + 2\varepsilon_{\mathrm{m}}]^2 + \varepsilon_2^2} \qquad \text{Eqn (2.28)}$$

while the polarizability, α; can be written as

$$\alpha = V\left[\frac{\varepsilon/\varepsilon_m - 1}{\varepsilon/\varepsilon_m + 2}\right] \qquad \text{Eqn (2.29)}$$

2.2.2.3 Mie Theory

The quasi-static approximation regime avails as a first rough estimation when sufficiently vanishing small sized nanoparticles (diameter ≤ 20 nm) are considered. Still, in practice the calculations presented above provide a vital approximation for spherical or ellipsoidal nanoparticles with diameter ≤ 100 nm illuminated with visible and/or near infrared radiation. Yet, for large particles in these dimensions, retardation effects of the electromagnetic field over the diameter of the particle become significant and multipole contributions to the extinction spectra become important. Thus, the frame of Mie theory has to be used to address the problem of larger nanoparticles for which the quasi-static approximation is not valid due to significant phase-changes of the driving fields over the nanoparticle volume [70]. Mie applied Maxwell’s equations with adequate conditions in spherical coordinates utilizing multipole expansions of incoming magnetic and electric fields and established a complete theory of the scattering and absorption of incident radiations by a sphere to illustrate the phenomena behind the colors of colloidal AuNPs suspended in solution. Indeed, Mie was not the foremost to derive a solution of this problem, but the first who applied this solution to the problem of light scattering of MNPs embedded in a non-absorbing and transparent medium [80]. The necessary parameters to determine the optical response of a particle embedded in a given medium are (i) the particle size, (ii) the particle material optical function, and (iii) the optical function of embedding transparent and non-absorbing medium. Mie theory expands the internal and scattered fields into a set of normal modes termed by vector harmonic and the quasi-static approximation effective for smaller MNPs are recovered by a power series expansion of absorption (Q_{abs}) and scattering (Q_{sca}) coefficients while retaining the first term only. In the Mie theory, the scattering and extinction (Q_{ext}) efficiencies are [79]

$$Q_{sca}^{(\mathrm{p})} = \frac{2}{x^2}(2P+1)\left(\left|a_{\mathrm{p}}\right|^2 + \left|b_{\mathrm{p}}\right|^2\right) \qquad \text{Eqn (2.30)}$$

$$Q_{ext}^{(\mathrm{p})} = \frac{2}{x^2}(2P+1)\mathrm{Re}\left(a_{\mathrm{p}} + b_{\mathrm{p}}\right) \qquad \text{Eqn (2.31)}$$

here, P is the number of multipole extension of the fields proposed by the spherical symmetry of the problem. For instance, $P = 1$ corresponds to the case of dipolar mode just as the one described in quasi-static approximation. $x = kr$ with $k = \frac{2\pi}{\lambda}$, the modulus of the wave vector; r is the radius of the given particle, and a_{p} and b_{p} are known as Mie coefficients given by

$$a_{\mathrm{p}} = \frac{m\psi_{\mathrm{p}}(mx)\psi_{\mathrm{p}}'(x) - \psi_{\mathrm{p}}(x)\psi_{\mathrm{p}}'(mx)}{m\psi_{\mathrm{p}}(mx)\xi_{\mathrm{p}}'(x) - \xi_{\mathrm{p}}(x)\psi_{\mathrm{p}}'(mx)} \qquad \text{Eqn (2.32)}$$

$$a_{\mathrm{p}} = \frac{\psi_{\mathrm{p}}(mx)\psi_{\mathrm{p}}'(x) - m\psi_{\mathrm{p}}(x)\psi_{\mathrm{p}}'(mx)}{\psi_{\mathrm{p}}(mx)\xi_{\mathrm{p}}'(x) - m\xi_{\mathrm{p}}(x)\psi_{\mathrm{p}}'(mx)} \qquad \text{Eqn (2.33)}$$

where m is defined as the ratio of the refractive index of the nanoparticle to that of the embedding medium, $m = n_{particle}/n_{medium}$; and ψ_{p} and ξ_{p} are the Riccati-Bessel cylindrical functions [79].

2.2.2.4 Factors Influencing Plasmonic Enhancement

The plasmonic field is ample and complicated. For decades research groups have shown that plasmons are influenced by a few well known factors which affect their optical and electromagnetic behavior and basic functional properties.

2.2.2.4.1 Size and Shape of Metal Nanoparticles

Size and shape of metal nanoparticles are among the key factors identifying the light coupling efficiencies of plasmons architectures. It refers to the fraction of incident light that can be coupled into the semiconductor absorber layer due to scattering by the nanoparticles. This coupling is illustrated in Figure 2.12a which demonstrates that smaller particles have their effective dipole moment very close to the semiconductor absorber layer and thereby couple a substantial amount of light into the underlying semiconductor as a consequence of enhanced near-field coupling [49].

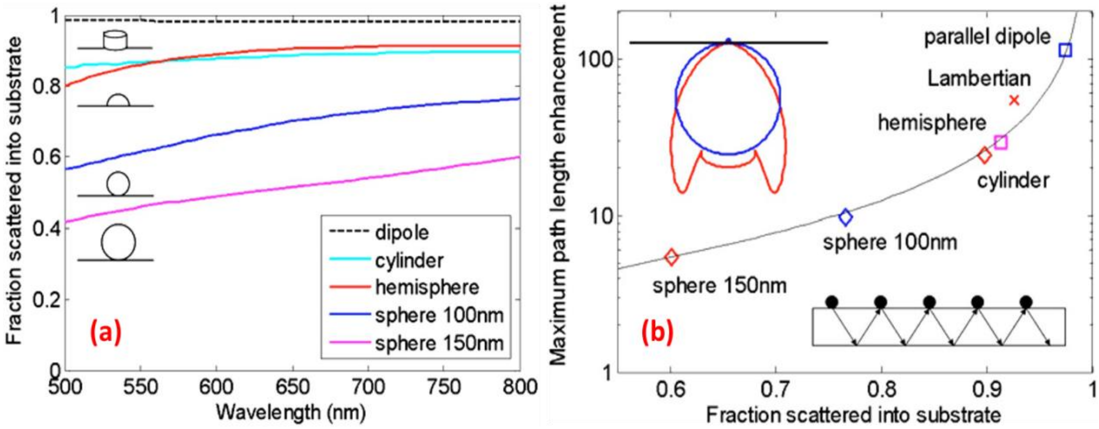

Fig. 2.12 (a) Fraction of light scattered into Si substrate, f_{sub}, for AgNPs on a 10 nm thick SiO_2 atop Si: a cylinder (diameter of 100 nm and height of 50 nm); hemisphere (diameter of 100 nm); and sphere (diameter of 100 nm and 150 nm). f_{sub} of a parallel electric dipole a 10 nm above Si is also plotted (dashed black). (b) Maximum path length at 800 nm wavelength. The line is a guide for the eyes. Insets: (bottom-right) geometry assumed to calculate the path length enhancement; (top-left) angular distribution of scattered power for a parallel electric dipole a 10 nm from Si (red) and Lambertian scatterer (blue)

From Figure 2.12, it is seen that for a point dipole near the substrate, 96 % of incident light is scattered into silicon assuring the enormous power of particle scattering. Figure 2.12b presents the enhancement in the path-length inside the solar cell absorber calculated from Figure 2.12a using the first-order scattering model. Parasitic absorption by the nanoparticles is neglected in the calculations presented in Figure 2.12b, and an ideal rear reflector is considered. Enhancement up to 30-fold is found for hemispherical nanoparticle with 100 nm diameter placed on Si substrate. The addressed light-trapping effects are much pronounced at the plasmon resonance peaks, which can be tuned by well-engineered dielectric constant of the embedding medium [49].

When the nanoparticle shape is considered, it can be seen that hemispherical and cylindrical shaped nanoparticles have better performance than spherical ones. But fabrication of these complicated structures is time consuming and hard to be integrated to solar cells. Spherical MNPs, on the other hand, are easier to fabricate using simple dewetting technique and integrate to the solar. Furthermore, Figure 2.12 explains the advantages of utilizing smaller MNPs since they can create forward scattering anisotropy. Still, smaller MNPs exhibit ohmic losses scaling with a volume of V, while scattering have a term of V^2 as shown in Equation 2.28 and Equation 2.27, respectively. It is worth mentioning that integration of a dielectric spacer layer between MNPs and the absorber layer enhances the effective scattering cross-section drastically. This enhancement can be attributed to the fact that a space layer does hinder destructive interference between the incident excitation and reflected fields, although at the price of reducing the near field coupling. Finally, for wavelength lying off-LSP, fano-resonance effects may cause destructive interference between scattered and non-scattered light radiations leading to reflection rather than incoupling enhancement [49]. MNP of disk shapes have a large fraction of their geometrical volume close to substrate surface and can therefore allow a substantial fraction of photon scattered into semiconductor substrate [81]. Contrariwise and Sundararajan et al. have revealed that MNP aggregates can lead to photocurrent reduction, a crucial issue that must be considered in colloidal fabrication of MNPs

[82]. In this study, they have also revealed that nanoshells cause optical vortexing that lead to photogenerated current reduction.

Figure 2.13 shows the Extinction (E) of spherical AgNPs of different sizes embedded in Al:ZnO (with $n \sim 2$) in a wavelength range relevant for solar cells applications plotted using Mie scattering theory [83]. The polarizability of the particle is dependent on the size as well as on the surrounding medium which is fixed in this calculation [79]. Extinction measures the amount of light scattered by the AgNPs towards the higher refractive index material or absorbed by the particle itself. Thus, E gives a direct estimation of the scattering efficiency of AgNPs fabrication in a certain medium.

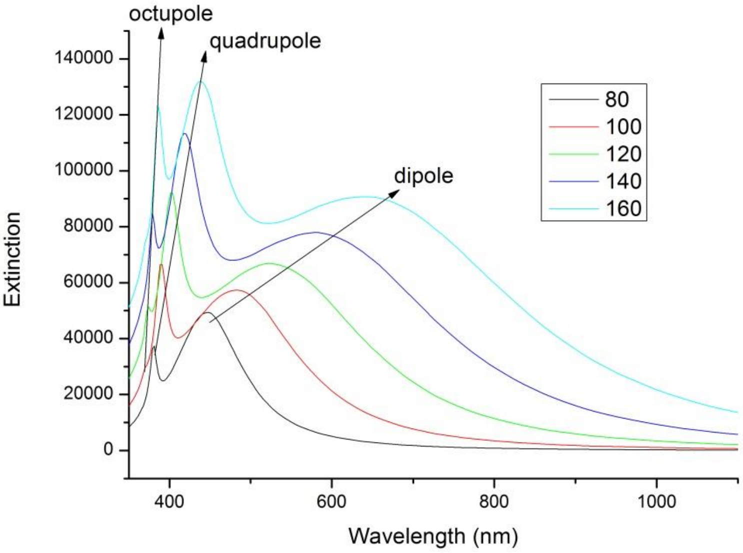

Fig. 2.13 Extinction spectra of spherical AgNPs of different sizes embedded in Al:ZnO medium

Figure 2.13 shows the extinction spectra of different sized spherical nanoparticles in Al:ZnO medium where the subsequent red shift is observed as the particles size increased. This red-shift is attributed to the dynamic depolarization which exists due to the fact that as particle size increases, conduction electrons across the particle no longer move in phase. As a consequence of dynamic depolarization, the accompanied field generated by the polarized matter diminishes at the particle center. Consequently, there is a reduced restoring force and thus a red-shift in the MNPs plasmon resonance. When particle sizes increase to an extent where scattering becomes significant, this re-radiation leads to a radiative damping correction to the quasi-static polarizability, resulting in a significant broadening of the plasmon resonance [49,84]. The resulting broadening of the particle resonance and the red-shift accompanying the increasing particle size is desirable for solar cell devices in general and Si-based solar cells in particular, as increased scattering at longer wavelengths would enable good light trapping close to the bandgap of Si material. Yet, as particle size increases sharp, scattering multipole oscillations are initiated as is clearly seen in Figure 2.13. All the considered particle sizes exhibit quadrupole resonance while octupole resonance appears for particles with diameter above 120 nm. The contribution of multipole oscillations can be neglected since they are present in the UV-Blue wavelength range that can readily be absorbed efficiently by solar cells without the aid of any light trapping interface. Furthermore, those oscillations cannot couple efficiently to the substrate modes and the energy is lost [46,84].

2.2.2.4.2 Metal Nanoparticles Assembly

MNPs assembly on top of the solar cell has a tremendous effect determining the fraction of light scattered into the absorber semiconductor waveguide. The optical scattering by MNPs placed on top of a photodetector results in a coupling of the normally incident photons to the device surface into lateral optical propagation paths within well engineered semiconductor thin film structure. This coupling is due to the introduction of a lateral wave vector component in the scattered wave [85]. In this experiment, structures of Silicon on Insulator (SOI) photodetector were used to investigate the effect of periodic arrays of MNPs on the photon coupling of incoming photons with normal incidence into the SOI waveguide. In this experiment, randomly and periodic arrays of Ti/Au nanoparticles were fabricated on SOI surface by electron beam lithography. Random assembly Ti/Au nanoparticles showed an enhancement in photocurrent response by a factor of ~2.5 in a broad enhancement peak centered at 1000 nm wavelength. On the other hand, in the case of periodic assembly of Ti/Au nanoparticles, the photocurrent enhancement was observed with much sharper peaks with a more dramatic enhancement in the photocurrent by factor of 6. These photocurrent enhancements were observed at wavelengths that correspond to confined waveguide modes of the SOI device and constructive interference of electromagnetic wave components scattered by neighboring nanodots [85]. This experiment clearly demonstrates that enhancements in photocurrent response at required wavelengths can be tuned by appropriate engineering of periodic assembly of MNPs by simply considering specific scattering and momentum conservation associated with MNPs periodic arrays.

2.2.2.4.3 Metal Selection

The dielectric function of metals with lower interband absorption is expressed by the Drude model as indicated by Equation 2.22. In free space, inserting Equation 2.22 into Equation 2.29 leads to

$$\alpha = 3V \frac{\omega_{\mathrm{p}}^2}{\omega_{\mathrm{p}}^2 - 3\omega^2 - i\gamma\omega} \qquad \text{Eqn (2.34)}$$

Thus LSP resonance of a metal sphere in free space occurs at $\omega_{\mathrm{sp}} = \sqrt{3}\omega_{\mathrm{p}}$ which is clearly dependent on the free electron density in the considered particle. The free electron density is the highest in Al and Ag and thus resulting in LSP resonances in the ultra-violet, and lower in Au and Cu resulting in LSP resonance in the visible portion of solar spectrum. Among different metals, Cu is the cheapest but it is much more absorbing than Au and Ag. The effects of native oxide and interband transition at 1.5 eV of the albedo have to be considered [84]. Ag is one of the best materials for solar cells as compared to Au due to its lower cost and because its computed effective maximum path length enhancement in the presence of absorption is more than twice as high as the path length enhancement for Au [81]. Yet Ag experiences oxidation effects that degrade its scattering efficiency and must be encapsulated [61].

2.2.2.4.4 Dielectric Spacer Medium

The spacer between the MNPs and the underlying substrate goes a long way in effecting the coupling of localized surface plasmons [49, 71, 84-86]. In the case of cSi solar cells, the spacer layer of Si_3N4 or SiO_2 is deposited on the Si wafer for surface dangling bond passivation. Indeed, understanding the influence of dielectric spacer on the plasmonic scattering is essential. The incorporation of dielectric spacer layer is not limited to cSi solar cells, but some other semiconductors require a dielectric spacer to enhance the photovoltaic performance. Placing a MNP on a dielectric spacer influence plasmonic scattering in three ways [84,86] (i) modifying the metal nanoparticle polarizability, and consequently the surface plasmon resonance wavelength, (ii) altering the intensity of the electric field driving the surface plasmon resonance, and finally (iii) changing the angular spectrum of the scattered light. These three effects depend strongly on the details of the underlying layer geometry and the location of the nanoparticle [71,73].

The first effect (LSP resonance shift) gives an opportunity to tune the MNPs resonance to wavelength region where transmission losses in the considered semiconductor become significant. The influence of the underlying substrate on surface plasmons of MNPs and nanostructures has been extensively studied by many research groups and the red shifting of the wavelength of plasmon resonance with increasing underlying substrate refractive index is well known [49, 71, 73, 84-86]. This is the essence which makes this effect the corner stone of any enhanced solar cell as the absorption coefficient of semiconductor materials drops significantly close to its bandgap. Shifting the plasmon resonance to wavelengths closer to the bandgap of the semiconductor allows more light to be absorbed via light trapping. Materials with higher refractive index, Si for example, tends to red shift the plasmon resonance as a result of depolarization effects. This indicates that bringing the MNP much closer to higher refractive index semiconductor by reducing the spacer layer thickness shifts the plasmon resonance to longer wavelength, if the thickness of the spacer layer is similar to or smaller than the near field of the surface plasmon excitation; in the order of a few tens of nm. Catchpole et al. calculated the scattering and extinction cross-sections normalized to the geometrical cross-section of spherical AgNP of 100 nm in diameter embedded in air, silicon nitride (Si_3N_4), and Si using Mie theory and utilizing Drude model fitting to experimental data as input of dielectric functions [84]. In these calculations, a dipole resonance is observed at 390 nm for air, 690 nm for Si_3N_4 and 1190 nm for Si. Quadrupole effects at shorter wavelengths and hexadecapole (only observed in the case of Si) resonances were also observed. Higher order multipole resonances have low albedo but still exhibits significant scattering cross-sections. The red shift in LSP resonance as a function of embedding dielectric medium and the contribution of higher order multipoles must be considered in solar cell application. The effectiveness of changing the dielectric spacer layer; between AgNPs or AuNPs and the underlying absorber layer, on tuning enhancements in photocurrent has been demonstrated experimentally and numerically by Beck et al [87].

Secondly, the thickness of the dielectric spacer layer modifies the strength of the scattering cross section [84,86], as a consequence of changes in the electric field driving the resonance. With increasing the thickness of the spacer layer, the driving field increases for MNPs located on the front illuminated surface of the solar cell. This result is closely related to an earlier work done by Drexhage [88] on the influence of substrates on dipole radiation, which was focused on the electromagnetic interactions of fluorescing molecules (treated as radiating dipoles) with metal surfaces. In this work, Drexhage revealed that when a dipole is located in the front side of a mirror, the path difference between the reflected and the direct beam causes the molecules to radiate strongly when constructive interference takes place but suppresses radiation when destructive interference occurs. Another recent report has shown that metal nanoparticles located on the rear surface of substrates with an ultra-thin spacer layers can result in enhanced scattering cross-sections [89].

Finally, the presence of a high refractive index dielectric spacer layer modifies the angular spectrum of metal nanoparticles and leads to an asymmetric scattering profile. A significant fraction of scattered light will be coupled into the semiconductor where the exact fraction of scattered light can be determined by the dielectric spacer layer thickness [86]. This guarantee that larger fraction of the scattered light goes into the semiconductor active layer and thus is trapped by total internal reflection mechanism [84,86]. This effect of dielectric spacer thickness has been studied by S. Pillai et al. [86]. In this experiment, they have demonstrated that, for self-assembled AgNPs located on the front surface of polycrystalline silicon solar cells, thin layers of SiO_2 spacer of thickness around 30 nm are desirable to diminish photocurrent suppression at optical wavelengths and enhance the driving field strength, while still serving light trapping near the bandgap of Si because of broad scattering plasmon resonances of the random AgNPs. Catchpole et al. have demonstrated via numerical calculations that the maximum absorption by a semiconductor is a compromise between the largest scattering cross section, which increases with increasing spacer layer thickness, and the fraction preferentially scattered into a-Si:H which decreases with increasing spacer layer thickness [84].

CHAPTER 3

THIN FILMS DEPOSITION TECHNIQUES, MATERIALS PROPERTIES

In this chapter, the deposition techniques of the starting materials and the fabrication of metal nanoparticles MNPs using the self-assembling dewetting technique will be discussed.. The metal thin films are deposited by filament evaporation and sputtering from metal target. The latter is also used to deposit Transparent Conductive Oxide (TCO) films. The starting metal film for obtaining metal nanoparticles is few nanometers and it will be referred as “metal thin film”. In the following sub-section, general review regarding the optical and structural properties of a-Si:H will be presented and compared with c-Si properties. Thin film a-Si:H is deposited using the standard capacitively coupled Plasma Enhanced Chemical Vapor Deposition (PECVD) which will be briefly discussed. To finalize this chapter, the working principles of a-Si:H thin film and c-Si solar cells will be described together with their basic structures.

3.1 Fabrication of Metal Nanoparticles

MNPs are produced by a large number of techniques. The most common ones are evaporation and sputtering deposition of metal thin film followed by thermal annealing, in a process called dewetting [71-73,90-92]. There are four main advantages of the dewetting technique: i) low processing and material cost, ii) compatibility with solar cells fabrications, iii) ability of large scale production, and iv) fairly good control of MNPs very important parameters such as size, shape, and distribution. Other methods used are citric reduction, scanning tunneling microscopy assisted nanostructure formation, laser ablation, wet chemical synthesis, electron beam lithography and nanosphere lithograph.

In this thesis, the simple dewetting technique is used to fabricate MNPs from a thin metal film deposited either by evaporation or sputtering from Au or Ag targets.

Sputtering is the process of bombarding a pure silver target by heavy Argon atoms in plasma at a chamber pressure of 5 mtorr and a fixed Ar flow rate of 175 sccm. The sputtering process was also used to deposit thick Ag back reflectors used in this study. Details on the sputtering technique to prepare Ag thin films used in this thesis; along with required optimizations parameters are discussed elsewhere [93]. Thermal evaporation is the evaporation of the desired metal from the melt located in a heated tungsten filament in a vacuum environment of $2.5x10^{-5}$ Torr. Depending on the target and the starting metal, it is possible to deposit Ag and Au thin metal films of or even a combination of them with the desired thicknesses as controlled by a quartz oscillator. Different substrates can be used to deposit these metal thin film, like TCO, a-Si:H, Corning glass, Schott glass, and silicon wafers. To obtain nanoparticles, we used the dewetting technique by annealing metal thin films of specified thicknesses in N2 flow of 155 sccm for time duration of 1 hour. The annealing temperature can range from 200 °C to 500 °C for Ag and up to 600 °C for Au depending on the underlying substrate. To produce nanoparticle on a-Si:H it is desired not to exceed the annealing temperature beyond the deposition temperature of a-Si:H of approximately 200 °C. On Corning glass, annealing temperature is safe below 600 °C but above 600 °C some cracking in the glass may take place. Annealing of the metal thin films modifies its structure leading to the formation of MNPs or nanoislands whose size and shape depend on the metal film thickness, the annealing temperature, and time. The annealing temperature, annealing time, underlying substrate, and the metal thin film will be varied throughout this thesis. Each of the above parameters shows specific and different structural and optical behavior of MNPs or nanoisland. The properties of the metal thin film and MNPs can be characterized by Scanning Electron Microscopy (SEM) and Atomic Force Microscopy (AFM). Finally, to better judge the enhancement of the MNPs, it is always preferable to produce the same structure with and without metal nanoparticles. Thus two different and separate substrates having the same experimental history is produced for comparison.

3.2 TCO Deposition by Sputtering, Texturing

Transparent Conductive Oxide (TCO) films are commonly prepared by magnetron sputtering. This work was done at The Centre for Solar Energy Research and Applications (GÜNAM) facilities; the thin film research group in GÜNAM has concentrated on the use of Al:ZnO as TCO layer for a-Si:H solar cells. Indeed, zinc oxide (ZnO) is nontoxic and abundant which provides several advantages: i) moderate temperature processing, ii) good diffusion barriers, and iii) compatibility with subsequent hydrogen rich plasma depositions. The sputtering facility at GÜNAM provides the possibility to deposit Al:ZnO from 2 % aluminum-doped zinc oxide ceramic target on $25 \times 25\ \mathrm{cm}^2$ substrates using RF (13.56 MHz) magnetron sputtering technique. In this process, Argon (Ar) ions are created by low pressure glow discharge and are then accelerated towards the ZnO:Al target by the RF electric field established between the lower and upper electrodes. Once the Ar ions impact the target, the target material is knocked off and accumulates on the substrate. To get the best transparency and electrically optimized ZnO:Al film, the deposition pressure, temperature, and RF power are varied. Only films deposited at higher temperature (200- 400 °C) provide higher transparency and higher conductivity at higher deposition rate. Further details on Al:ZnO sputtering facility in GÜNAM can be found elsewhere [93].

In this thesis work, Al:ZnO coated glasses were prepared, the following considerations were made: i) glass substrates were heated for a total of 30 minutes; in the sputtering chamber before sputtering process started, to attain better crystallinity of sputtered Al:ZnO film, ii) Desired Al:ZnO films thicknesses and sheet resistance were achieved by maintaining the substrate heater temperature at 250 °C while the glass scanned back and forth horizontally below the Al:ZnO cathode [94]. During sputtering, the chamber pressure was maintained at 5 mTorr under a constant Ar flow of 175 sccm flow rate, and a RF target power of 500 watt [91].

The sputtered Al:ZnO films before annealing are basically flat; and referred to as “as deposited (flat)” or “flat” throughout this work, and do not hold any of the light scattering properties required in thin film silicon solar cell front TCO. Still, it is possible to modify their surfaces by nanotexturing using wet chemical texturing making it possible, to obtain the required light scattering properties. Texturing of Al:ZnO coated glasses studied in this work were obtained by one step wet chemical texturing process. After sputtering, the flat Al:ZnO coated glass substrates were dipped in 5 % diluted hydrochloric acid (HCl) agitated with a magnetic stirrer for 30 seconds. During texturing, HCl solution was maintained at a moderate temperature (> 40 °C). The undesired texturing products on the Al:ZnO surface were removed by carefully rinsing the them in deionized water (DIW) at room temperature and then dried by N_2 [91]. In this study, texturing with hydrofluoric acid (HF) was not used for texturing Al:ZnO used as front TCO layer to avoid any unintentional roughening of the glass substrate itself. Utilizing HF in texturing of front Al:ZnO coated glass will roughen the glass surface and thus the resultant light scattering efficiency will be due to contributions of textured Al:ZnO and textured glass. While for Al:ZnO sputtered on thick Ag back reflector, both HCl, HF, and mixtures of both can be used to obtained textured Al:ZnO. In the latter case, the presence of thick Ag back reflector eliminates the scattering contribution of roughened glass.

3.3 Material Properties of Hydrogenated Amorphous Silicon (a-Si:H)

3.3.1 a-Si:H Structural Properties

In a-Si, the local atomic structure resembles that of crystalline phase. Yet, many differences can be seen in Figure 3.1. Crystalline silicon (c-Si) diamond structure is a four-fold coordinated atom that is normally tetrahedrally bonded to four neighboring Si atoms. This tetrahedral structure is extended throughout the whole lattice coordinate giving a well long range ordered lattice. The unit cell in crystalline structure is repeated periodically as shown in Figure 3.1, left. On the other hand, a-Si structure shows variations in both bond lengths and bonding angles the long range order leading to a large density bulk unsatisfied bonds called dangling bonds as shown in the right side of Figure 3.1. Dangling bonds refer to the atomic bonds which are not sharing electrons with the neighbor Si atoms. Dangling bonds are defects, have energies in deep into the forbidden gap and therefore act as traps or recombination centers for photo-generated carriers. A key technique to decrease their density is to passivate them with hydrogen during or after deposition. When hydrogen is introduced in deposition process, it bonds to one of the dangling bond, and thereby can reduce the density of dangling bonds up to several orders of magnitude depending on the hydrogen fraction. It has been reported that it is possible; with hydrogen passivation, to reduce the dangling bonds density from $10^{25} - 10^{26}$ to $10^{21} - 10^{22}$ m^{-3} [93,95]. Amorphous silicon passivated with hydrogen is called hydrogenated amorphous silicon (a-Si:H). Industrial scale a-Si:H has a low defect density in the order of 10^{22} m^{-3}. While hydrogen passivation appears to reduce the density of dangling bonds, prolonged exposure to light or electric bias lead to the regeneration of these defects in the so-called light-induced degradation or the Staebler-Wronski effect [22]. One advantage of a-Si:H when compared with c-Si lies in that a-Si:H simpler and lower cost production technique (see section 3.3.3). Amorphous silicon captured the interest of the photovoltaic community after its successful doping in 1974 by Spear and Le Comber [4]. a-Si can be doped to produce p- or n- layer by the same doping elements as in c-Si.

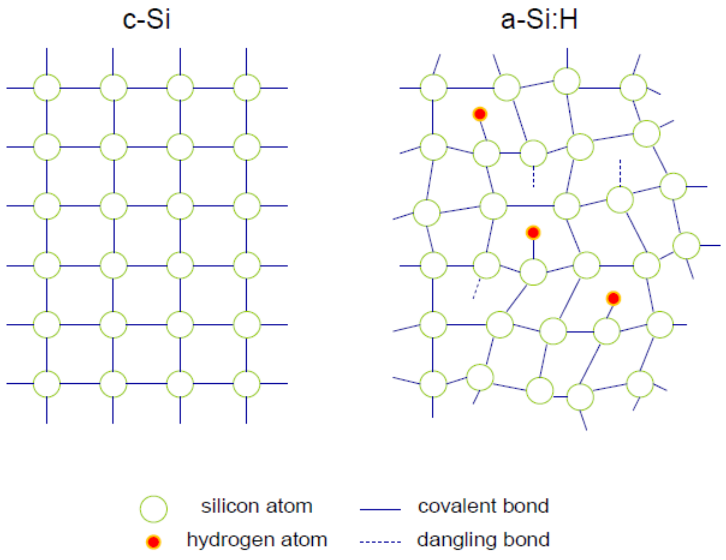

Fig. 3.1 Schematic drawing of cSi (left) and a-Si:H (right) atomic structures

3.3.2 Optical Properties of a-Si:H and c-Si

Light absorption by a semiconductor is accompanied by excitation of electrons from the lower energy state; the valence band (Ev), to the higher energy state, the conduction band (Ec). In the case of direct bandgap material, this transition occurs when the energy of the incoming photon is equal or larger than the band gap (E_{g}) of the semiconductor. (E_{g}) represents the forbidden energy states separating the valence band and the conduction band edges, $E_{\mathrm{g}} = \mathrm{Ec} - \mathrm{Ev}$.

cSi has an indirect band gap of ~1.12 eV; at room temperature, where the lower edge of the conduction band and the upper edge of the valence band correspond to different momentum value, $\mathbf{k}$. Thus absorption of photon with lower energy and the electron transition are attained by a two-step process involving lattice vibrations (phonons). Phonons do conserve the momentum difference between the valence and conduction band states. This indirect transition results in a reduced optical absorption in the visible portion of the spectrum since photon absorption involves phonons for momentum conservation. Direct transition from valence band to conduction band can also occur but such transition requires photon energies much larger than band gap.

On the other hand, a-Si:H is a quasi-direct bandgap semiconductor, so the momentum is conserved. Thus the probability of photon absorption is higher in the visible spectrum with photon energy higher than 1.8 eV as seen in figure 3.2 [96]. As a result, a 500 nm thick a-Si:H can absorb light with wavelength lower or equal to 600 nm efficiently. Lower than 1.8 eV, the density of dangling bonds and tail states govern the a-Si:H absorption of light [19].

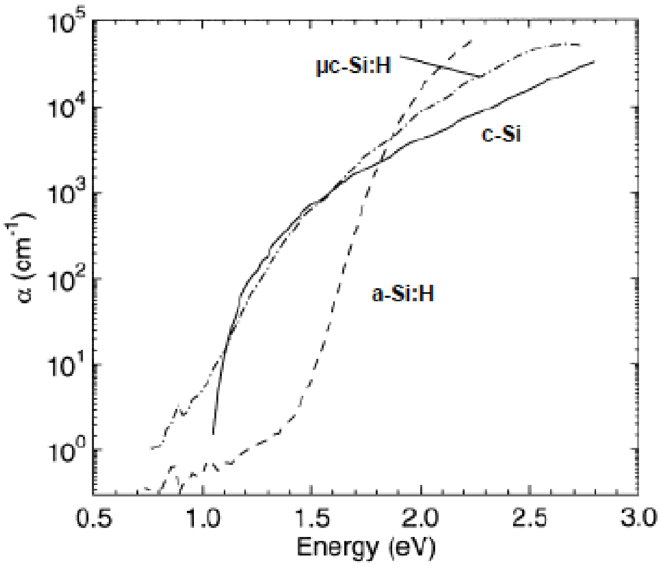

Fig. 3.2 Absorption coefficient of a-Si:H, cSi, and μc-Si:H

3.3.3 Deposition of a-Si:H by PECVD

Plasma enhanced chemical vapor deposition (PECVD) is considered as one of the most prominent techniques for depositing a-Si:H thin films. In this technique, a-Si:H is deposited by the plasma glow discharge decomposition of silane (SiH4) diluted with hydrogen. This technique offers the possibility to deposit thin films at relatively moderate temperatures which allows the usage of wide variety of substrates including glass, plastic, and stainless steel. Plastic foils or stainless steels are promising candidates for roll-to-roll production processes. Furthermore, PECVD technique provides lower energy consumption in industrial-scale compared to c-Si where temperatures higher than 1000 °C are a prerequisite for many cSi production steps. This lower cost production and the high-module scale production can overcompensate the lower electronic outcome of a-Si:H solar cells.

Silane gas can dissociate thermally at temperatures above 450 °C producing films with low poor optoelectronic properties. The PECVD technique gives the sufficient dissociation energy at lower temperatures of 150-200 °C and under vacuum typically in the order of $\sim 10^{-8}$ mbar in a low pressure glow discharge. Plasma is formed by a radio frequency (RF) applied across the two parallel electrodes in the capacitively coupled configuration. At GÜNAM, the PECVD facility is equipped with a 13.56 MHz excitation frequency which is similar to the frequency used for large area devices (RF-PECVD) [93]. Figure 3.3 shows a typical schematic drawing of PECVD process between planar electrodes.

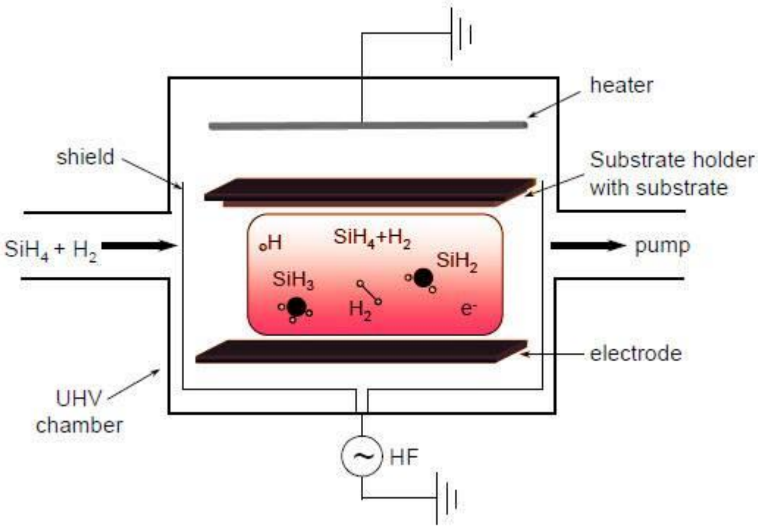

Fig. 3.3 Schematic outline of typical PECVD process

When silane is considered as a source gas in the glow discharge process, ionized species, such as SiH^+, + SiH_2^+ and reactive neutral species such as SiH, SiH_2, SiH_3, Si_2H_6, and H are created inside the plasma by electron impact.

The possible dissociation reactions involved in PECVD deposition process of a-Si:H thin films are [97]:

$$e^- + SiH_4 \rightarrow SiH_2 + 2H + e^- \qquad \text{Eqn (3.1)}$$

$$e^- + SiH_4 \rightarrow SiH_3 + H + e^- \qquad \text{Eqn (3.1)}$$

SiH_2 and SiH_3 resulting as SiH4 dissociates do contribute to solid film deposition. Details on a-Si:H deposition optimization by PECVD used throughout this thesis are found elsewhere [93].

3.4 Working Principles of cSi and a-Si:H solar cells

3.4.1 Working Principle of cSi solar cell

To better understand the working principle of a-Si:H thin film solar cells, it is important to begin with illustrating the functioning principle of c-Si solar cells. Details and precise description of the production line of c-Si solar cells; fabricated in GÜNAM, used in this thesis can be found elsewhere [98]. A c-Si solar cell is obtained when a p-n junction is formed by varying the doping concentrations within Si. Figure 3.4 (left) shows the band diagram of a p-n junction. Upon absorption of light with enough energy, electrons (e^-) are excited from the valence band to the conduction band leaving quasi-holes (h^+) in the valence band. Both of the charge carriers e^- and h^+ move through the crystal and contribute to photocurrent generation. The generated free charge carriers (both e^- and h^+) due to light absorption in the bulk material reach by diffusion the space charge region (with high static electric field) and the back contact, respectively. Since the free charge carriers diffuse to the p-n junction, c-Si solar cells are referred as “diffusion solar cells”. Space charge region is a consequence of the potential difference between n- and p-doped layers. The width of space charge region of p-n junction is highly dependent on the exploited doping level and is typically thinner than 1 μm for a c-Si solar cell [99].

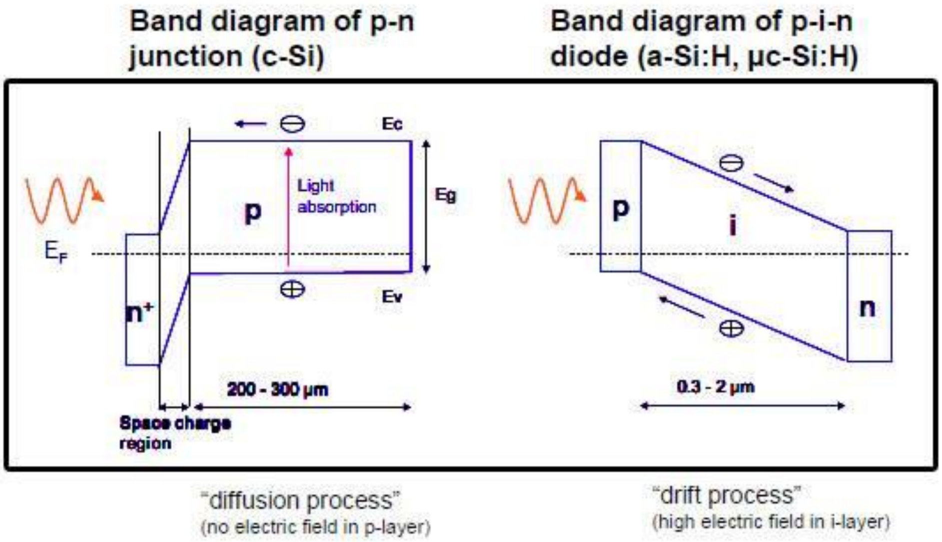

Fig. 3.4 Band diagram of a typical c-Si p-n junction (left) and that of a-Si:H p-i-n diode (right)

3.4.2 Working Principle of a-Si:H solar cell

In contrast to c-Si, photogenerated carriers in a-Si:H encounter many defects and travel a much shorter distance before recombining. The Fermi-level of a-Si:H is highly dependent on defect state distribution. These factors prevent a-Si:H solar cell to be produced as p-n junctions. The a-Si:H solar cells are thus processed as p-i-n or n-i-p layer stack where i refers to the additional intrinsic layer sandwiched between the p and n layers. The intrinsic (i-) is undoped is made thicker and has a much lower defect density to minimize recombination and act as the main absorber layer. The p-doped and n-doped thin layers act to create a static electric field across the i-absorber layer as shown in figure 3.4 (right). A direct separation of the photogenerated carriers is attained by drift in the static electric field established across the junction by the p and n layers. Since the charge carriers generated by absorption of light are driven and separated by the static electric field, the a-Si:H solar cells have gotten the name of "drift solar cells" [100].

3.4.3 a-Si:H Solar Cells in p-i-n and n-i-p Configuration

a-Si:H thin film solar cell can be deposited in two different configurations as shown in figure 3.5, the substrate (n-i-p) and the superstrate (p-i-n).

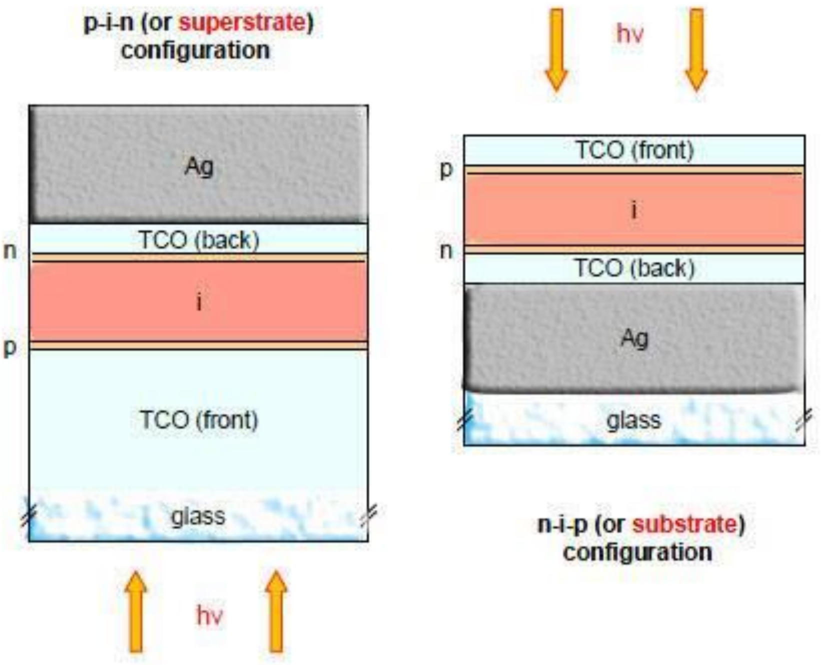

Fig. 3.5 Schematic drawing of a-Si:H solar cell in the superstrate configuration (left) and substrate configuration (right). The Ag front grid of the substrate n-i-p cell, deposited on the front TCO, is not shown here. Layers thicknesses are given in the text

The names substrate or superstrate refer only to the ordering of deposition of the a-Si:H thin films. For superstrate configuration, first p-layer is deposited then i-layer and finally the n-layer thus it takes the name of p-i-n solar cells (figure 3.5; left). On the other hand in the substrate configuration, the first n-layer is deposited then i-layer and finally the p-layer thus it takes the name of n-i-p solar cells (figure 3.5; right). It can be seen from figure 3.5 that in both cases the cell is illuminated from the p-layer rather than the n-layer because defect distribution in the i-layer is highly modified near the interfaces with the doped layers. Thus these regions are crucial in terms of free carrier recombination. The red portion of the spectrum is basically absorbed in the bulk of the solar cell, thus the red response is nearly independent of the side of illumination (either through the p- or the n-layer). On the other hand, the blue is more sensitive to the device side of illumination. In a-Si:H, the hole mobility is lower than electron mobility and therefore: i) holes experience the shortest distance to their corresponding doped layer and ii) the best configuration of the cell have to be selected such that holes resulting from blue light absorption (in the i-layer close to the first interface with p-doped layer) only have to pass through one of the two defect-rich regions of the i-layer, in order to reduce h^+es recombination probability. Taking into account the above mentioned requirements, the best solution would be to illuminate the device through the p-layer. It is worth mentioning that there is not any fundamental difference regarding the operating principle of either configuration; n-i-p or p-i-n.

3.4.4 Gerenal Requirements for an Optimized a-Si:H Solar Cell

To get an optimized working a-Si:H solar cell with good conversion efficiency the following requirements are needed:

i. The front TCO must be transparent, highly conductive, and with a modified surface to reduce the reflection and to improve diffuse transmittance
ii. The a-Si:H films: should be characterized by low defect density, more stabilized, higher electrical conductivity, optimized optical behavior, thin p- and n-layers to reduce absorption but thick to create the static electric field (around 10 nm for p- layer and 20 nm for n-layer). The i- layer has to be thick enough to maximize absorption but thin enough to minimize light-induced degradation and partially relax the low hole mobility. An acceptable thickness is usully in the range of 200-300 nm
iii. The back reflector should consist of a thin TCO (~80 nm) and an Ag mirror. Thin TCO is integrated as a buffer layer to improve the reflection

of the back reflector and thus the light absorption in solar cells. Back reflector surface can be modified to improve the diffuse reflectance

CHAPTER 4

CHARACTERIZATION TECHNIQUES

4.1 Optical Spectroscopy

Optical measurements were performed using an optical setup equipped with an integrating sphere of 8-inch in diameter having 5-ports (Oriel, Model no. 70679NS), a monochromator (Oriel Model no: 74100), a thermal light source, and a UV enhanced Si photodiode detector (Oriel, Model no. 70356) in combination with a lock-in amplifier is utilized to measure the unprocessed signal for the spectral wavelength range of 350-1100 nm. A diffuse reflective material is coated on the internal walls to minimize unwanted reflections. Light source from a 100 W or 250 W halogen lamp is collimated and chopped before it is directed through the sphere input port (known as the transmission port) and the output of the sphere (known as the reflection port). The sample plane of the output port is tilted by 4°, in such a way that all the specular light is reflected away from the surface of the sample, at 8° with respect to the incident light to hit the dedicated specular reflection port. A reference calibration disc of known diffuse and total reflectance is utilized in the measurements. Each of the measurements results in a uniform intensity distribution within the inside of the integrating sphere surface, which is analyzed through the monochromator attached to the detector port of the sphere [90].

The used optical set up is sketched in Figure 4.1 for the case of transmittance measurements. For reflection measurements; the sample is placed in the reflection port instead [91].

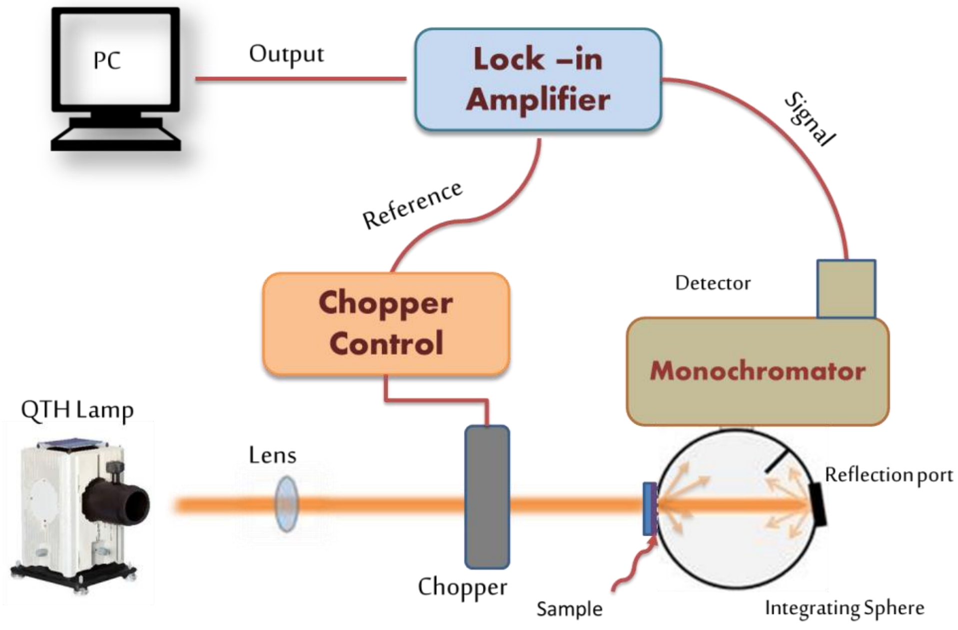

Fig. 4.1 Optical set up used in optical measurements

During total transmittance measurements; defined as $T = T_{\text{direct}} + T_{\text{diffuse}}$, the considered sample is mounted at the integrating sphere front port while the output port is closed by the reference calibration disc as shown in Figure 4.2.

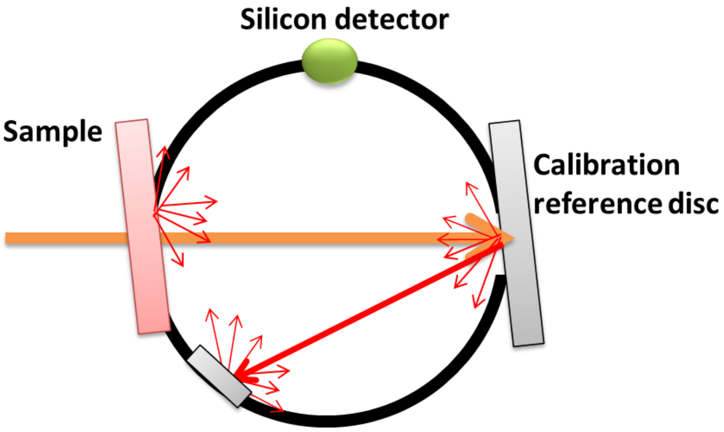

Fig. 4.2 Integrating sphere in total transmittance mode

To calculate T, the measured raw data are processed by considering the following relation.

$$T = \frac{T_{raw}}{R_{calibration\ disk}} \qquad \text{Eqn (4.1)}$$

where, $R_{calibration\ disk}$ is the reflection of the reference calibration disc measured before mounting the sample at the front port and T_{raw} is the raw total transmitted signal from the considered sample.

During diffuse transmittance measurements; T_{d}, the sample is mounted at the integrating sphere front port while the output port is kept empty so that all direct transmitted light through the sample leaves the integrated sphere uninterrupted as shown in Figure 4.3.

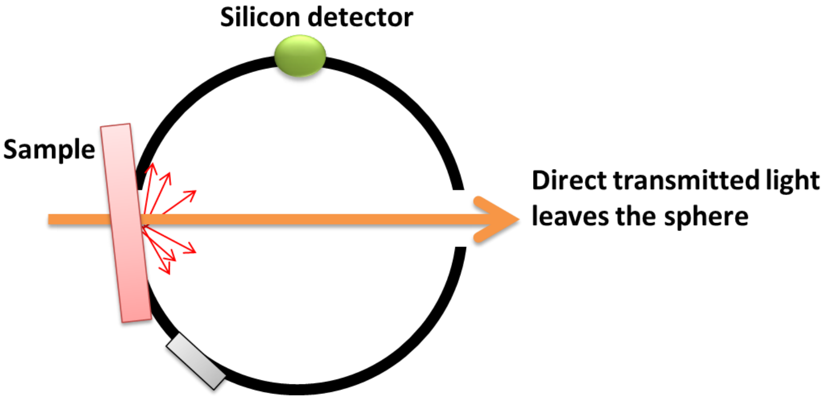

Fig. 4.3 Integrating sphere in diffuse transmittance mode

Diffuse transmittance is calculated according to

$$T_{\mathrm{d}} = \frac{T_{d,raw} - Dark \times T}{R_{calibration\ disk}} \qquad \text{Eqn (4.2)}$$

where, T is calculated from Equation 4.1, $T_{d,raw}$ is the raw diffuse transmitted signal from the considered sample, and $Dark$ is the background measurement with both the input and output ports of the sphere are empty. After calculating the total and diffuse transmittance, haze in transmittance; H, is calculated using the following relation

$$H = \frac{T_{\mathrm{d}}}{T} \qquad \text{Eqn (4.3)}$$

The total reflectance data is collected while placing the sample at the output port of the sphere as shown in Figure 4.4.

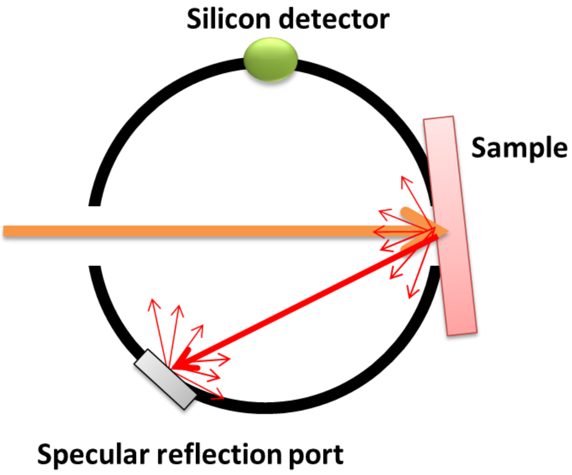

Fig. 4.4 Integrating sphere in total reflectance mode

Total reflectance measurement R is calculated according to

$$R = \frac{R_{raw} - Dark}{R_{calibration} - Dark} \qquad \text{Eqn (4.4)}$$

where R_{raw} is the raw total reflected signal from the considered sample.

During diffuse reflectance measurements; R_{d}, the sample is placed at the output port of the sphere while keeping the specular reflectance port empty so that all specular reflections from the sample leave the sphere without contributing to the measurements and shown in Figure 4.5.

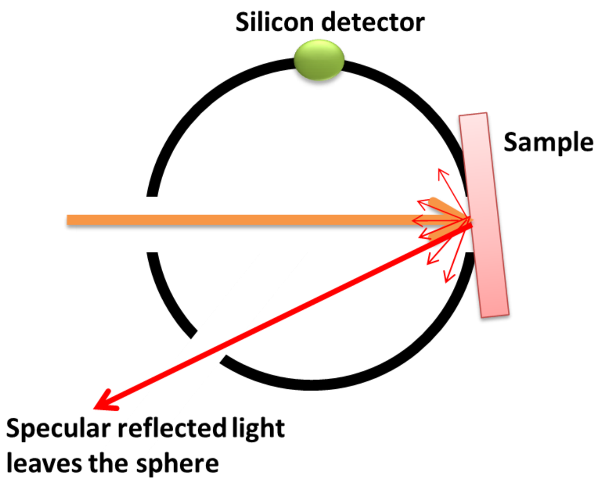

Fig. 4.5 Integrating sphere in diffuse reflectance mode

Diffuse reflectance measurement; R_{d}, is calculated according to

$$R_{\mathrm{d}} = \frac{R_{d,raw} - Dark^{*}}{R^{*}_{calibration} - Dark^{*}} \qquad \text{Eqn (4.5)}$$

where, $R_{d,raw}$ is the raw diffuse reflected signal from the considered sample, and $R^{*}_{calibration}$ and $Dark^{*}$ are the diffuse reflection of the calibration disc and the background measurement, respectively; measured while leaving the specular reflectance port of the sphere empty.

After calculating total transmittance; T, and total reflectance; R, Extinction is calculated according to the following relation

$$E = 1 - R - T \qquad \text{Eqn (4.6)}$$

In the case when the sample has no plasmonic scattering interface, the extinction in Equation 4.6 is called absorption; A. Extinction light is either absorbed by the interface or scattered into neighboring layers. Thus, maximum extinction is recorded when either of the total transmittance and/or the total reflectance is at its minimum. The LSP resonance of MNPs is calculated from the dip in the total transmittance curve for samples with no back reflector and from the maximum in the total reflectance curve for samples with back reflector, where no total transmittance can be measured.

4.2 Spectral Response

Samples are prepared for spectral response measurements by evaporating Al electrodes using shadow masks. Evaporated Al electrodes have standard coplanar geometry with two rectangular electrodes of 1.0 cm in length and 3 mm in widthseparated by 1 mm gap. The total dark and total photocurrents are measured by illuminating the sample using a one-sun solar simulator under applied voltage. The spectral dependence of the photocurrent is measured by illuminating the samples with a 250 W halogen lamp through a monochromator (Oriel Model no: 74100) over 300-1200 nm spectral range. A representative schematic diagram of a sample ready for spectral response measurement under applied voltage (V) as shown in Figure 4.6 yields an a-Si:H resistance of

$$R = g/\sigma l t \qquad \text{Eqn (4.7)}$$

where, σ is the conductivity.

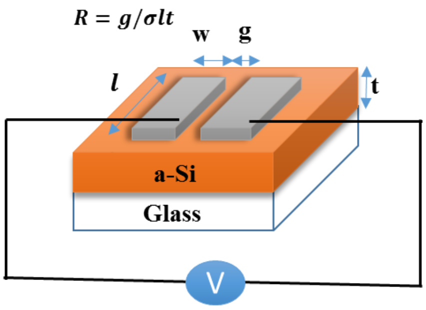

Fig. 4.6 Schematic diagram of a typical a-Si:H of thickness (t) deposited on glass and prepared for spectral photoresponse measurement. Electrodes of length (l), width (w), and gap (g) are deposited by evaporation via shadow mask

The photocurrent $\mathrm{I_{ph}}$ is calculated as the difference between the current measured under light designated as $\mathrm{I_L}$ and that measured in the dark designated as $\mathrm{I_D}$, $\left(\mathrm{I_{ph}} = \mathrm{I_L} - \mathrm{I_D}\right)$ measured at each incident wavelength. The spectral dependence of photocurrent calculated as the difference between the current obtained under illumination at a given wavelength and the current measured in the dark both obtained 10 volt bias and averaged 5 times. The photocurrent normalized to the excitation power, plotted against the excitation wavelength and measured in ampere/watt, somewhat mimics the External Quantum Efficiency (EQE). It measures the induced photocurrent (number of electrons) under bias per unit power of excitation light (number of incident photons).

4.3 Scanning Electron Microscopy

Samples surface topographical images are obtained using a Scanning Electron Microscope, SEM (FEI, Model Quanta400 F) by detecting the secondary (SE) low energetic electrons ($\sim 10 - 50$ eV) generated from the samples upon interacting with the SEM electron beam. SE emission is a function of surface topography SEM is a non-destructive microscopy that provides detailed information about sample topography; surface features, surface morphology; size and shape of surface features, and information about materials composition from small areas. SEM generates a beam of electrons in vacuum. This electron beam is collimated by electromagnetic condenser lenses, focused by an objective lens, and scanned across the surface of the sample by electromagnetic deflection coils. FEI SEM is equipped with a field emission gun working in ultra-high vacuum ($\sim 10^{-11}$ torr) conditions that offers a large probe current (up to few nanoamperes); for better image sharpness and contrast, and small diameter electron probes; for best resolution down to $2 - 5$ nm , over a wide energy range $(1 - 30\ \mathrm{keV})$; to change the depth of interaction volume. Lower electron beam energy is usually applied to collect images and material composition from the very top layer of sample surface. To measure the considered films thicknesses, the samples are mounted at 90° with respect to the SEM focused beam of electrons. Backscattered electrons (BSE) detector is used to collect high energetic

BSE resulted from elastic collisions with energies almost the same as incident electron beam energy. Image generated using BSE has lower resolution than the SE, yet allows to differentiate between the surface elements where elements of greater atomic mass appear brighter. In order to obtain high resolution SEM images, 3 nm gold/palladium (Au/Pd) alloys are usually sputtered on top surface of the samples.

FEI is equipped with an X-ray detector to collect information about the elemental composition of the sample surface. This method is known as Energy-dispersive X-ray spectroscopy (EDX) or sometimes named as Energy Dispersive X-ray Analysis (EDXA). When the electron beam bombards the sample, it excites ground state electron to an inner shell leaving a hole behind. This hole is filled by an outer shell electron by releasing energy in the form of X-ray. Emitted X-ray is the identity of atomic structure of each element.

4.4 Atomic Force Microscopy and 4-Point Probe

Atomic Force Microscopy, AFM (Veeco Nanoscope5) operating in tapping mode, is used to determine the lateral feature size and average surface roughness of dedicated samples. Sheet resistance is measured by a 4-point probe (JANDEL, RM3-AR) instrument.

4.5 Spectroscopic Ellipsometry

Spectroscopic Ellipsometry (SE) is a sensitive, non-destructive and non-contact, non-direct, feasible optical technique to extract the complex refractive index, surface roughness, fractional composition, dielectric constant, optical band gap, and thickness of thick and thin films [101]. This spectroscopic technique is based on the polarization state change of polarized electromagnetic incident light interacting (either reflected or transmitted) through dedicated sample surfaces and/or interfaces. Electromagnetic radiation reflected from the sample surface leads to a polarization state change with respect to incident radiation. This polarization change is a characteristic uniqueness of each reflecting sample surface structure and its material composition and optical identity. Operation principle of SE is illustrated in Figure 4.8. Light generated from a Xenon lamp is collimated and then passed through a polarizer to produce a linearly polarized light. After interacting with the sample surface, the linearly polarized light becomes elliptically polarized.

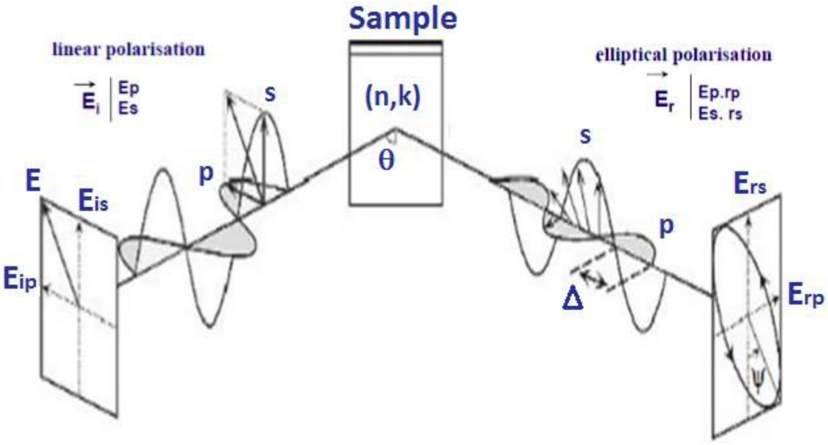

Fig. 4.8 Operation principle of SE

Light reflected from the sample surface has phase and amplitude changes that are different for electric field components polarized parallel (p) and perpendicular (s) to the plane of incidence. SE measures the amplitude ratio (ψ) and phase difference (Δ) of the parallel polarized (p) and perpendicularly polarized components. Thus SE measures the state of polarization (ρ) interpreted in terms of ellipsometric parameters ψ and Δ which are expressed as the ratio of the complex Fresnel reflection coefficients for parallel ($\widetilde{R_p}$) and perpendicularly ($\widetilde{R_s}$) polarized light as given in Equation 4.9 and shown in Figure 4.9. Fresnel reflectance coefficients are correlated to the optical constants of the surface [101].

$$\rho = \tan\psi e^{i\Delta} = \frac{\widetilde{R_p}}{\widetilde{R_s}} \qquad \text{Eqn (4.9)}$$

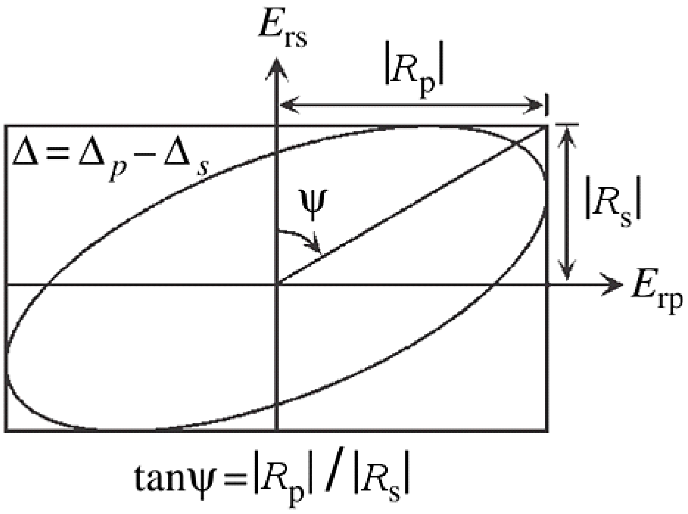

Fig. 4.9 Definition of SE parameters psi and delta for elliptically polarized reflected light

SE does not give a direct measurement of these parameters. It measures $\tan\psi$ and $\cos\Delta$ as a function of incident light wavelength or energy, thus a physical model including optical relations and an expected sample structure are assumed in a regression process as shown in Figure 4.10. Thus a model is needed to interpret the experimental SE parameters and thereby to obtain physical parameters of the dedicated sample layers. Several dispersion relation models have been developed to describe dielectric function of materials based on Lorentz or Drude oscillators [79]. Lorentz oscillators are basically exploited in absorption regions while Drude oscillators describe free electron behavior in metals.

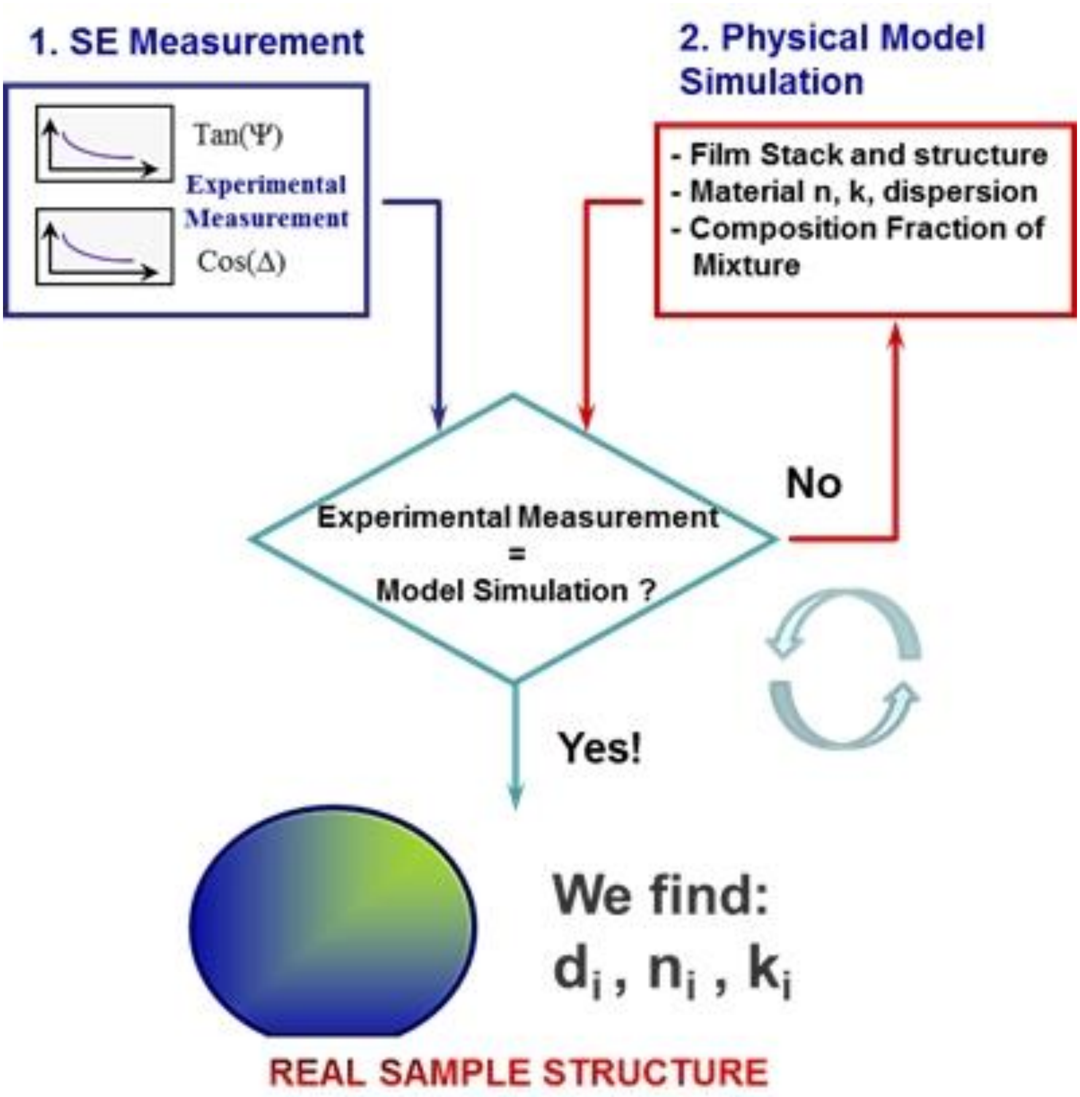

Fig. 4.10 Flow chart of SE data analysis

In this thesis, SE is utilized to determine the thickness, refractive index for SiO_x and SiN_x and band gap of a-Si:H films.

SiO_x and SiN_x thin films are usually modeled by Cauchy law, given by Equation 4.10 and Equation 4.11 for refractive index and extinction coefficient, respectively [102]. Cauchy's law is suitable empirical relation to characterize insulators and semiconductors or transparent materials in the ultraviolet and visible (UV/VIS) portion of spectrum incase the atomic polarization effect is neglected. Cauchy can offer smoothly changing fractional functions for wavelength dependence of refractive index and absorption coefficient.

$$n(\lambda) = A + \frac{B}{\lambda^2} + \frac{C}{\lambda^4} \qquad \text{Eqn (4.10)}$$

$$k(\lambda) = D + \frac{E}{\lambda^2} + \frac{F}{\lambda^4} \qquad \text{Eqn (4.11)}$$

For SiO_x and SiN_x, values such as $A = 1.5$ and $A = 1.8$ can be considered, respectively. B $= 0.001$ and C $= 0.001$ while $k(\lambda)$ can be set to 0 in modeling.

For a-Si:H, Tauc-Lorentz disperison formula is utilized [103]. This model is used for amorphous semiconductors and insulators in the interband region as well as transparent conductive oxides. Detailed derivation of this dispersion relation can be found elsewhere [103].

CHAPTER 5

FABRICATION OF SILVER NANOPARTICLES EMBEDDED IN AL:ZNO CONTACTS

In this chapter, fabrication of plasmonic interfaces consisting of silver nanoparticles (AgNPs) embedded in Al:ZnO will be presented. This interface has the potential to be integrated at the front surface or at the rear reflector of thin film solar cells to increase photon absorption and enhance the light-conversion efficiency. AgNPs are fabricated by the simple dewetting technique by annealing thin Ag film at temperatures lower than Ag melting temperatures in inert environment. Plasmonic interfaces of AgNPs with and without spacer layer show LSP resonance in the visible and near infrared portions of the solar spectrum, which is crucial in enhancing light trapping in thin film solar cells and thereby increasing conversion efficiency. The data and results presented in this chapter are published in Plasmonics [90].

5.1 Samples Preparation

To fabricate AgNPs, 15 nm Ag thin films were sputtered atop Al:ZnO films followed by annealing in nitrogen environment at flow rate of 150 sccm for 55 minutes in temperature ranging between 200 °C and 500 °C. To ensure the appropriate formation of AgNPs, the dielectric properties and melting points of Al:ZnO and Ag are considered. Immediately after the dewetting process the samples were optically characterized and imaged by SEM to minimize any contamination or oxidation arising from the atmosphere. The SEM images were analyzed using image analysis software (Gwyddion) to calculate the AgNPs mean particle radius distribution and their surface coverage.

A total of five sets of three samples each were fabricated all on Corning glass substrates as indicated in table 5.1.

Table 5.1 Design of samples structure

Sample Name	Step 1	Step 2	Step 3	Step 4
A	300 nm Al:ZnO	15 nm Ag	Annealing	
B	300 nm Al:ZnO	15 nm Ag	Annealing	60 nm Al:ZnO
C	300 nm Al:ZnO	15 nm Ag	60 nm Al:ZnO	Annealing
D	300 nm Al:ZnO	15 nm Ag at 150 °C	60 nm Al:ZnO	Annealing
E	90 nm Ag	60 nm Al:ZnO	15 nm Ag	Annealing

Sample sets A, B, C, and D are designed for potential use at the front interface while set E is designed for a rear reflector as it has a 90 nm thick Ag film. In samples of set B, Ag thin film is annealed to fabricate AgNPs before sputtering Al:ZnO on top. Sample set C is different from set B where the top Al:ZnO film was sputtered before AgNPs fabrication to investigate their formation inside Al:ZnO without exposure to air. Sample set E was introduced in this study to demonstrate the plasmonic effect for light reflected from the rear-reflector.

5.2 Formation of AgNPs at the Front Surface

Figure 5.1 shows the SEM images, particle size distribution and the optical response for the AgNPs formed by annealing samples in set A at temperatures 200 °C, 300 °C, and 500 °C. The mean particle radius increases with increasing annealing temperature which particularly noticed for the sample annealed 500 °C. Since the amount of Ag is conserved, the inter-particle spacing also increases with growing nanoparticles as the annealing temperature increases. The average mean particle diameter is taken as the quantity to compare particle sizes for this and subsequent structures. As the distributions indicate, the median particle diameter increases with annealing temperature.

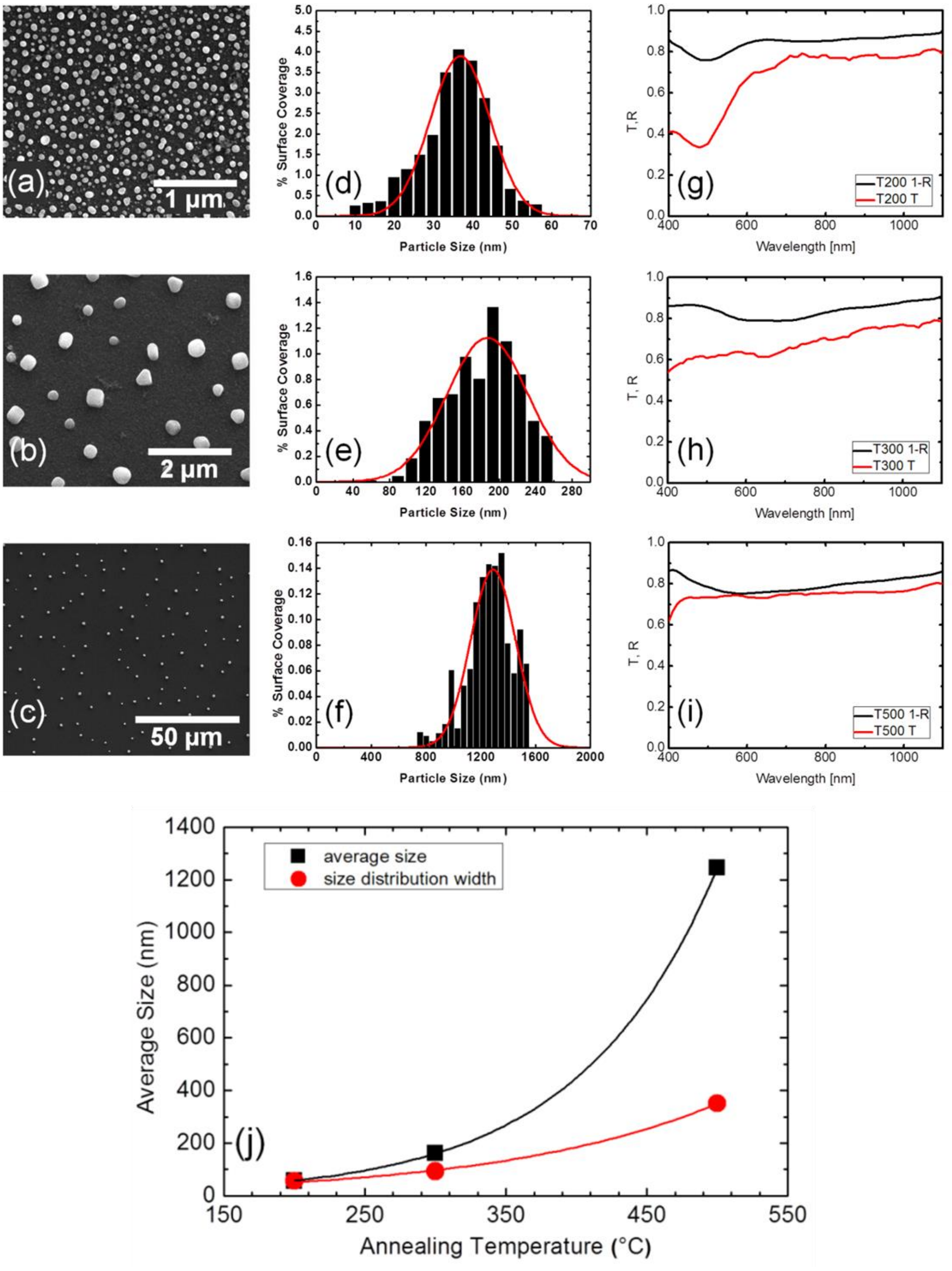

Fig. 5.1 SEM images obtained at different magnifications as indicated, mean radius distributions and optical response of AgNPs formed in sample set A annealed in nitrogen at 200 °C (a, d, g), 300 °C (b, e, h), and 500 °C (c, f, i), and the average particle size and average size distribution as a function of annealing temperature (j)

The LSP resonance peak that occurs at ~500 nm for sample annealed at 200 °C, is red-shifted to 630 nm for the sample annealed at 300 °C and disappears for the sample annealed at 500 °C. This red shift in LSP resonance peak is attributed to the increase in the mean particle diameter from ~35 nm for the film annealed at 200 °C to ~190 nm for the film annealed at 300 °C . No LSP resonance is detected for the film annealed at 500 °C, where the median particle diameter is larger than 1 µm. The absence of LSP resonance peaks is due to (i) the large particle size shifts the LSP into longer wavelength which is not in the considered spectral rannge and (ii) the scattering scross section is significanlly low due to poor surface coverage (< 1%) left by the dispersed large particles thus allowing a vast fraction of incident light to be transmitted through the top Ag interface. The increased absorption below 520 nm is attributed to the absorption in 300 nm thick Al:ZnO layer.

To examine the influence of top Al:ZnO layer on LSP resonance as well as on other optical properties of the formed nanoparticles, a total of 60 nm thick Al:ZnO film was sputtered atop of the formed AgNPs as specified in sample set B in table 5.1. Figure 5.2 shows the optical response of samples in set B annealed at temperatures 200 °C, 300 °C, and 500 °C. The particle formation in set B is identical to that in set A yet the LSP resonance peaks are red-shifted due to the addition of Al:ZnO top layer. As seen in Figure 5.2, the LSP resonance peak shifts from wavelength of ~500 nm for the sample in set A (no top Al:ZnO), to wavelength of ~550 nm for set B (with top Al:ZnO) as can be extracted from the dips of the total transmittance curves in Figure 5.1 and Figure 5.2, respectively. Similar shifts are not observed, however, for the sample annealed at 300 °C. This is probably because the nanoparticles formed at this annealing temperature are larger (~150 nm) and the additional film of 60 nm Al:ZnO sputtered atop the annealed layers is not likely to covering them properly. Indeed, the mean diameter of the AgNPs is larger than 60 nm and, therefore, the second 60 nm thick Al:ZnO film sputtered atop will conform with the bottom 300 nm thick Al:ZnO film forming a total of 360 nm thick Al:ZnO in the nanoparticle-free surface areas, thereby cause an increase in the absorption as can be noticed in comparing Figure 5.1 and Figure 5.2 for 300 °C and 500 °C annealing temperatures.

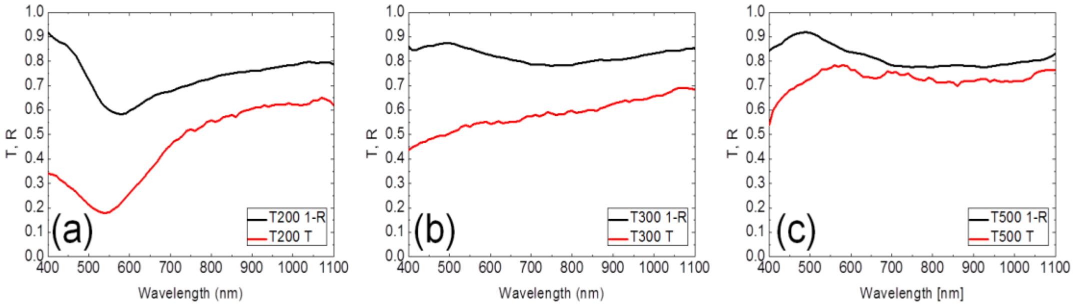

Fig. 5.2 Optical response of AgNPs formed in sample set A fabricated at at 200 °C (a), 300 °C (b), and 500 °C (c) annealing temperatures and covered by a 60 nm Al:ZnO as indicated in sample set B

To investigate the formation and optical response of AgNPs formed inside the Al:ZnO films, we construct the plasmonic design indicated in sample set C where the annealing steps are performed after the top capping Al:ZnO film is sputtered. Figure 5.3 shows the optical response of three samples in set C, where the 15 nm Ag layer is encapsulated by the top Al:ZnO film before annealing at temperatures 200 °C, 300 °C, and 500 °C. None of these three samples exhibit any noticeable LSP peaks as can be seen in Figure 5.3. The absence of plasmonic resonance peaks for the 200 °C and 300 °C annealing temperatures in this set is probably due to the capping layer of 60 nm Al:ZnO that blocks the dewetting process and thus the particle formation. However, as the annealing temperature increases, softened Ag appears to flow through Al:ZnO, by bulk diffusion, up to the top surface of the Al:ZnO layer forming Ag spheroids.

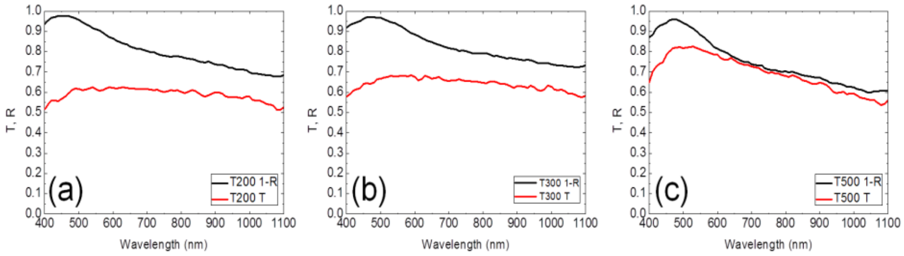

Fig. 5.3 Optical response of AgNPs formed in sample set C fabriacted at 200 °C (a), 300 °C (b), and 500 °C (c) annealing temperatures

Figure 5.4 shows the SEM images of two samples in set C annealed at 400 °C and 500 °C as well as the EDX data collected from a single particle fabricated at 500 °C annealing temperature. The films were tilted by 90 degrees with respect to SEM electron beam in order to demonstrate the Ag bulk diffusion process through Al:ZnO film. At 400 °C, the Ag film appears to preserve a continuous layer where dewetting is blocked by the top Al:ZnO even though some Ag starts to diffuse through Al:ZnO film. As the annealing temperature is increased to 500 °C, the film appears to diffuse forming Ag particles of diameter that exceed 1.02 µm and consist of pure Ag as confirmed by EDX data. These particles are not formed by the dewetting process and thereby their size and shape are not controlled perfectly. They are not embedded in the Al:ZnO layer and thus cannot be compared with the samples in set B. Moreover, they are dispersed randomly and do not interact enough with the incoming light both due to the large inter-particle spacing and their large sizes compared to the visible light wavelength.

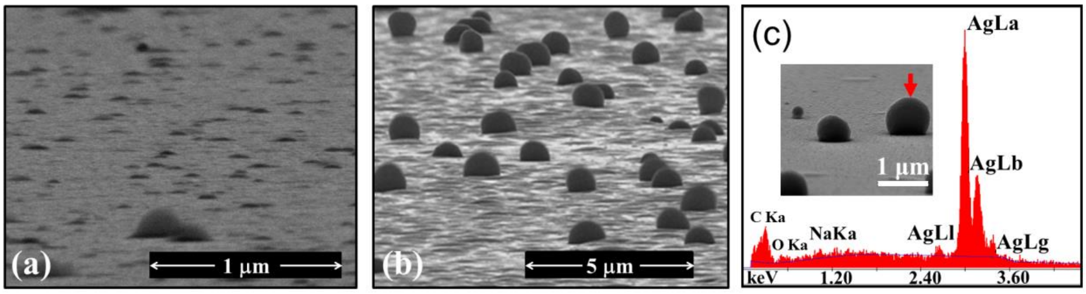

Fig 5.4 Cross-section SEM images for samples in set C annealed at 400 °C (a) and 500 °C (b) along with an EDX analysis (c) of an AgNP with diameter of 1.02 µm formed at the Al:ZnO surface after annealing at 500 °C. The inset in (c) shows a magnified image of the AgNP (pointed by a red arrow) from which the EDX data was acquired

It is crucial to perform the annealing and subsequent characterizations immediately after the Ag deposition since Ag exposure to air leads to the formation of silver oxide/sulfide that significantly alters and the location LSP resonance. Even though the dewetting process which involves the exposure of AgNPs to atmospheric modifications appears to increase absorption, it is still important to develop a technique by which the AgNPs are embedded inside the dielectric medium without any exposure to atmosphere. AgNPs exposure to atmosphere causes atmospheric modifications of the AgNPs and their embedding medium, which may degrade their scattering efficiency. Since dewetting processes failed for the capped Ag film, it was crucial to build a structure in which dewetting and the dielectric encapsulation are both completed without exposure to air. For this goal, sample set D was constructed by sputtering 15 nm Ag film on the Al:ZnO coated glasses substrate temperature of 150 °C compared to room temperature for sample set C to initiate the dewetting process.

Figure 5.5 shows the optical response for three samples in set D annealed at 200 °C, 300 °C, and 500 °C. It is not possible to extract the particle mean radius distribution as the top Al:ZnO film inhibits its measurements, but dips occurring in absorption curves clearly indicate the presence of LSP resonances in these interfaces. The optical response from these samples shows clear LSP resonance peaks occurring at 709 nm for the sample annealed at 200 °C, 700 nm for the sample annealed at 300 °C, and 820 nm for the sample annealed at 500 °C, suggesting that formation of AgNPs from the dewetted film are successfully occurring during the subsequent annealing steps. Increasing the substrate temperature during Ag sputtering to 150 °C appears to enhance the dewetting of encapsulated Ag film even in the presence of the top Al:ZnO layer and prevents the bulk diffusion of Ag film through top Al:ZnO layer as was observed in sample set C.

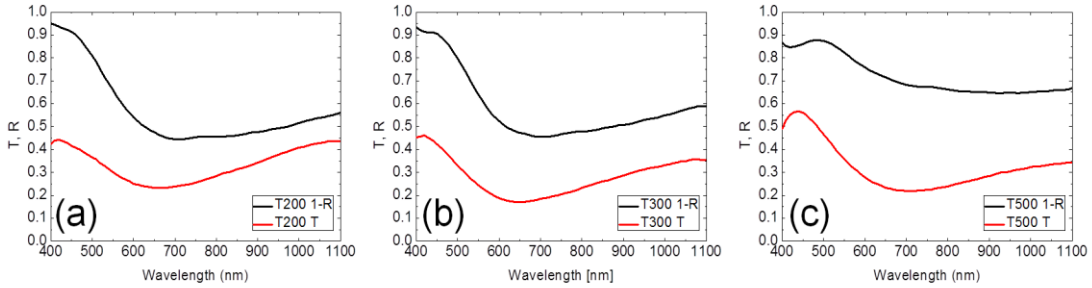

Fig. 5.5 Optical response of AgNPs formed in sample set D fabriacted at 200 °C (a), 300 °C (b), and 500 °C (c) annealing temperatures

Figure 5.6 shows SEM images of thin Ag films (~15 nm) sputtered at room temperature (left) and another at 150 °C (right). It is clear that the Ag film sputtered at 150 °C is rather discontinuous indicating that dewetting of Ag is initiated without complete AgNPs formation. The LSPs peaks observed in Figure 5.5 indicate that this discontinuity in as sputtered Ag film permits the formation of nanoparticles even in the presence of the top encapsulating Al:ZnO film at these standard annealing temperatures.

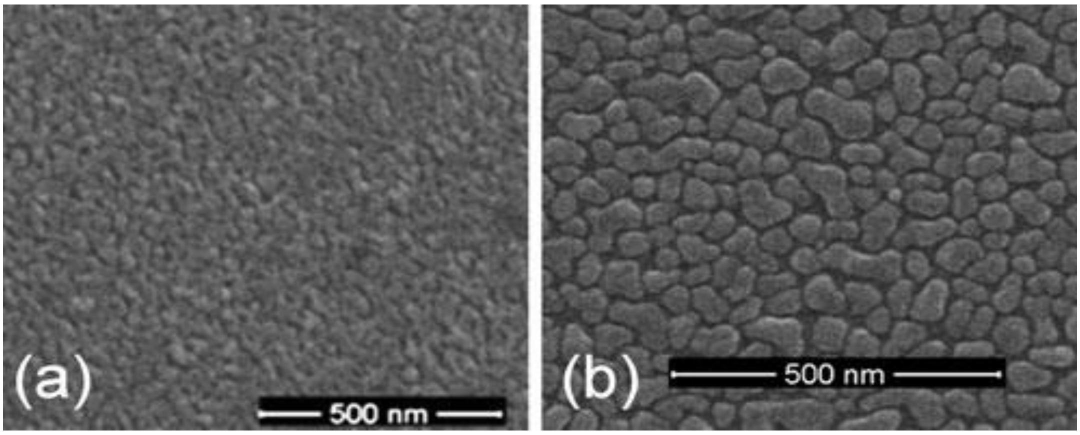

Fig. 5.6 SEM images of thin Ag films sputtered atop Al:ZnO film at room temperature (a) and at 150 °C (b)

5.3 Formation of AgNPs at the Rear Surface

To examine AgNPs formation and their plasmonic influence on the light reflected back from the rear reflector, sample set E was constructed. Sample set E is similar to set A except for the additional 90 nm Ag thick film sputtered on the glass substrate. Figure 5.7 shows the SEM images along with the radius distribution and optical total reflectance for the particles obtained by annealing at 200 °C and 500 °C. The SEM images as well as the particle size distributions are consistent with those obtained for set A as expected, yet the total transmittance measurements shown above for set D, are naturally blocked by the 90 nm Ag back reflector in set E. In samples containing rear reflector, LSP resonances are extracted from the maxima of the total reflectance curves. The LSP resonance peak occurs at ~500 nm for the sample annealed at 200 °C where the average particle size is ~ 50 nm while no LSP resonance peak is detected for the sample annealed at 500 °C, which is again attributed to the larger particle size at this annealing temperature. The presence of 90 nm thick Ag film in sample set E appears to have no influence on the formation, size distribution and optical characteristics of the fabricated AgNPs.

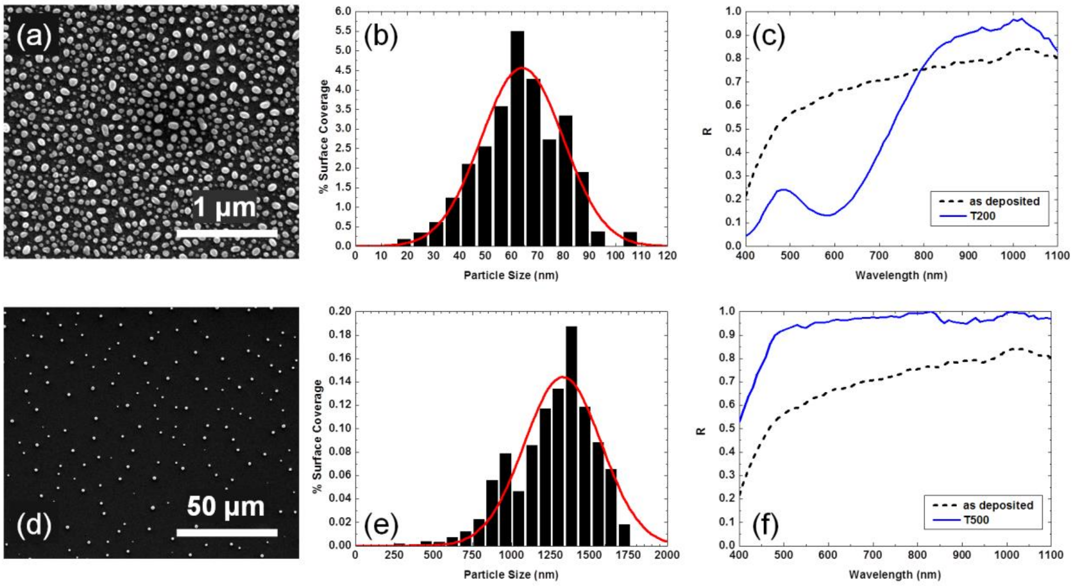

Fig. 5.7 SEM images, particle size distribution, and measured total reflectance for samples in set D obtained by annealing at 200 °C (a,b,c) and 500 °C (d,e,f)

CHAPTER 6

ENHANCED OPTICAL ABSORPTION AND PHOTORESPONSE OF ASI:H THIN FILM BY SINGLE AND DOUBLE PLASMONIC INTERFACES

In this chapter, we present the influence of single and double plasmonic interfaces fabricated using self-assembled AgNPs and integrated at the interfaces of two different media with various dielectric optical constants and placed at the rear of device-quality a-Si:H thin films to measure enhanced light-trapping and any corresponding improvement in a-Si:H photocurrent. Conventional studies employ solar-cell or photo-detector modules to measure enhancement in photocurrent due to the plasmonic interfaces. Our study use the enhancement in the spectral dependence of photocurrent in an isolated thin a-Si:H layer as an indicator for an improved plasmonic effect. It gives direct and conclusive results for the plasmonic effect before introducing more possible losses in conversion efficiency due to the more sophisticated actual device structure. The data and results presented in this chapter are published in Plasmonics [73].

6.1 Samples Preparation

A total of three types of plasmonic designs consisting of AgNPs placed at the interfaces between two dielectric media having different thicknesses and optical refractive indices are integrated to device-quality a-Si:H films deposited by the PECVD technique. Designs of samples structure are listed in table 6.1. AgNPs were fabricated by the standard dewetting technique starting with 15 nm Ag films sputtered on Corning glass substrates at room temperature and followed by annealing at 200 °C – 500 °C in nitrogen environment for 1 hour as was discussed in more details in chapter 5. For the double plasmonic interfaces, the plasmonic lower layer is fabricated at high annealing temperature to obtain larger AgNPs (first interface) followed by a 10 or 20 nm thick spacer layer of sputtered SiN_x or SiO_2. Then the upper plasmonic layer (secondary interface) is fabricated by dewetting of a second sputtered 15 nm Ag at 200 °C annealing temperature. Secondary annealing temperature is lower than that of first interface.

Table 6.1 Design of samples structure

Sample Name	Substrate	Step 1	Step 2 Annealing	Step 3	Step 4	Step 5 Annealing	Step 6	Step 7
PLS-Si	Corning glass	Reference set consisting of 250 nm a-Si:H deposited on Coring glass substrate						
PLS-01		15 nm Ag	200 °C	250 nm a-Si:H				
PLS-03		15 nm Ag	200 °C	20 nm SiO_2	250 nm a-Si:H			
PLS-05		15 nm Ag	400 °C	20 nm SiO_2	250 nm a-Si:H			
PLS-06		15 nm Ag	400 °C	20 nm SiO_2	15 nm Ag	200 °C	10 nm SiO_2	250 nm a-Si:H
PLS-07		15 nm Ag	400 °C	10 nm SiO_2	15 nm Ag	200 °C	10 nm SiO_2	250 nm a-Si:H
PLS-08		15 nm Ag	400 °C	20 nm SiN_x	15 nm Ag	200 °C	10 nm SiN_x	250 nm a-Si:H

As shown in table 6.1, a total of seven sample sets were constructed. Set PLS-Si is the reference set consisting of samples with 250 nm a-Si:H deposited on clean Corning glass substrate by PECVD technique. PLS-01 consists of an identical a-Si:H deposited directly on AgNPs fabricated by dewetting at 200 °C. PLS-03 is the same as PLS-01 except for a 20 nm SiO_2 spacer layer sputtered on top of the formed AgNPs. PLS-05 consists of a 250 nm a-Si:H film deposited on AgNPs fabricated by dewetting at 400 °C. PLS-06 is a double plasmonic interface consisting of two AgNPs interface such that the lower layer is fabricated by annealing Ag thin film at 400 °C on Corning glass while the upper layer is formed by dewetting at 200 °C. The two plasmonic interfaces are separated by a 20 nm SiO_2 layer and covered by another 10 nm SiO_2 spacer layer under the 250 nm a-Si:H thin film. PLS-07 is identical to PLS-06 except that the SiO_2 dielectric layer separating the two plasmonic interfaces is reduced to 10 nm. Finally PLS-08 is identical to PLS-06 except that the SiO_2 is replaced by SiN_x spacer layer of 10 nm thickness.

Samples are prepared for spectral photoconductivity measurements by evaporating Al electrodes on a-Si:H side as discussed in section 4.2. The final structure of a typical set ready for photocurrent measurements is depicted in Figure 6.1. Measurements were conducted by illuminating a-Si:H side as shown in Figure 6.1.

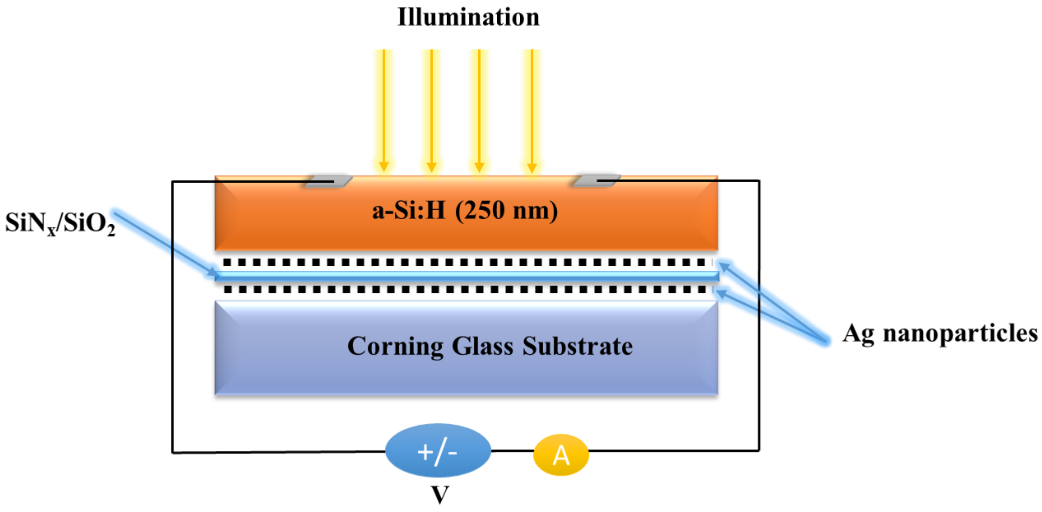

Fig. 6.1 Schematic diagram of a double plasmonic interface integrated to the rear of a-Si:H thin film for spectral photocurrent measurements by illuminating the Si side

6.2 Fabrication of Single Plasmonic Layers on Corning Glass

AgNPs are successfully formed on Corning glass by dewetting the 15 nm Ag thin film. Fabricated AgNPs are well separated even though their size, as described by the mean particle diameter, does not follow a perfectly well random distribution and their shape is not completely spherical. As can be seen in Figure 6.2, increasing the annealing temperature from 200 °C to 400 °C increases the particles size and their shapes appear to become qualitatively more spherical. However, increasing the annealing temperature to 600 °C appears to deform the Corning glass substrate leaving Ag and/or Ag/SiO_2 residue in the empty spaces between the AgNPs.

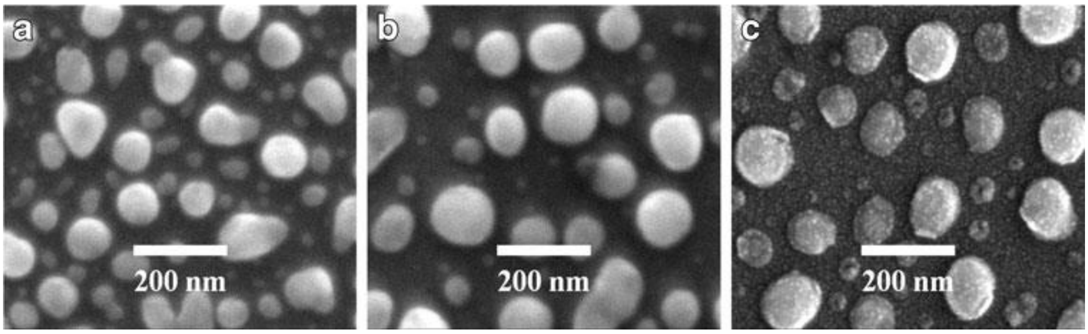

Fig. 6.2 SEM images of Ag thin film deposited on Corning glass annealed at (a) 200 °C, (b) 400 °C, and (c) 600 °C

In Figure 6.3, we present the particle size distribution for samples from sets PLS-01 annealed at 200 °C and PLS-05 annealed at 400 °C. These particle size analyses were performed just after the annealing process and before subsequent layers depositions. Data displayed in Figure 6.3 clearly demonstrate that the particle radius distributions are far from random and appear to exhibit a broader peak for the sample annealed at 200 °C. Annealing at 200 °C produces particles with radius distribution ranging from 10 nm to over 52 nm converting into particle diameter of 20 nm to 100 nm. Particle size distribution for the sample annealed at 400 °C, on the other hand, exhibits a narrower distribution (Figure 6.3 right) with a mean particle diameter ranging from 20 nm to over 90 nm in diameter. Since an average is meaningless for such broad distributions, we can just deduce that annealing at 200 °C produces more particles that are less than 50 nm diameter than does the annealing at 400 °C.

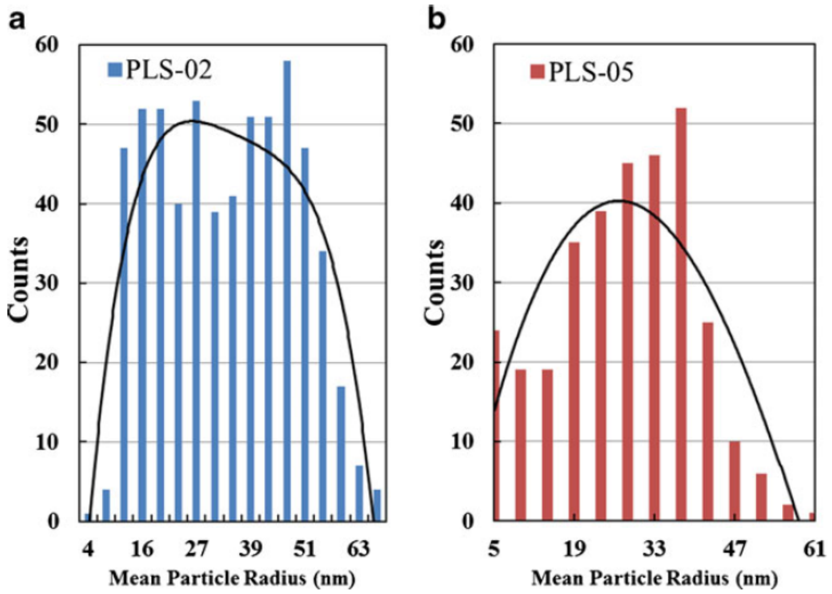

Fig. 6.3 Particle size distribution of AgNPs fabricated on Corning glass by annealing at (a) 200 °C, (b) 400 °C

Figure 6.4 shows the SEM images for a single plasmonic layer structure before and after covering by the 20 nm SiO_2 dielectric spacer layer which serves to electrically disconnect the plasmonic layer from the subsequent a-Si:H thin film. The presence of spacer layer visually increases the actual particle size by ~40 nm in diameter and thereby exaggerates the size of smaller nanoparticles yet that increase does not alter the MNPs effective size.

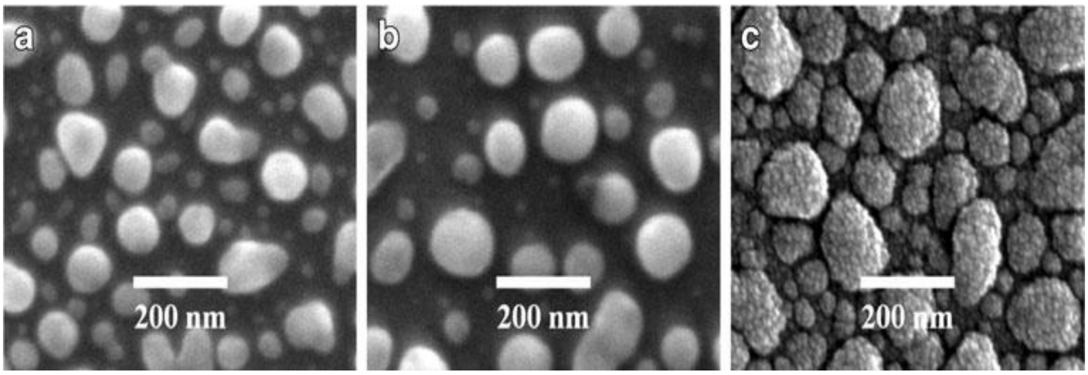

Fig 6.4 SEM images of (a) PLS-01: 15 nm Ag/200 °C (before the subsequent a-Si:H thin film), (b) PLS-05: 15 nm Ag/400 °C (before covering with oxide layer), and (c) PLS-03: 15 nm Ag/200 °C/20 nm SiO_2

Figure 6.5 shows the total transmittance spectra T for structures identical to those shown in Figure 6.4 to demonstrate the impacts of annealing temperature and dielectric spacer layer on the LSP resonance as inferred from the minima in the total transmittance spectra. Both parameters appear to redshift the LSP resonance. As can be seen in Figure 6.5, increasing annealing temperature from 200 °C to 400 °C redshifts the LSP resonance by 30 nm from 450 nm to 480 nm, while the presence of SiO_2 dielectric spacer layer redshifts LSP resonance by 60 nm to 510 nm. Moreover, the SiO_2 dielectric spacer layer appears to broaden the minimum in total transmittance spectra into the red while the increase in the annealing temperature just redshifts the LSP resonance without broadening the total transmittance spectra. As we shall demonstrate below, this broadening in transmittance has significant impacts on the spectral dependence of photocurrent in that region.

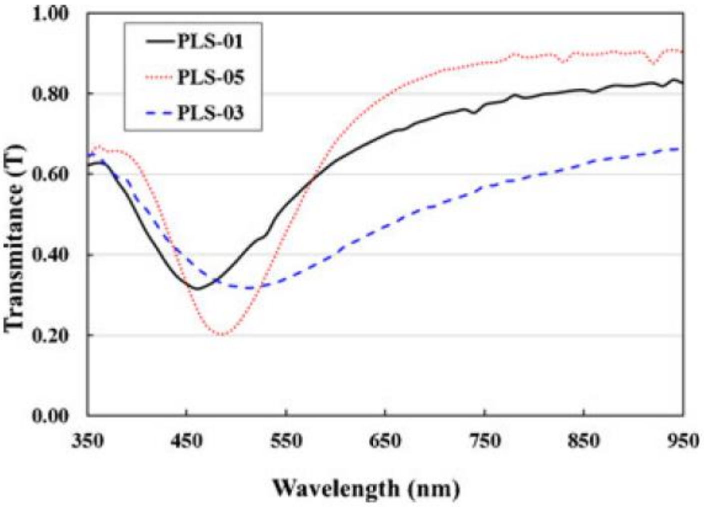

Fig. 6.5 Total transmittance spectra for various plasmonic layers showing the effects of dewetting temperature and dielectric spacer layer on the LSP resonance indicated by the minima in the transmittance curves: Solid black line (PLS-01 consisting of AgNPs fabricated at 200 °C anneal on Corning glass), dotted red line (PLS-05 consisting of AgNPs fabricated at 400 °C on Corning glass), and dashed blue line (PLS-03 similar to PLS-01 covered by SiO_2 nm)

In Figure 6.6, we show the LSP resonance wavelength versus annealing temperature for three different dewetting temperatures: 200 °C, 400 °C, and 600 °C. The LSP resonance of AgNPs shifts linearly to red with increasing dewetting temperature and therefore with particle size. Since we are interested in scattering and absorption due to plasmonic interfaces and their impact on spectral photocurrent, we plot the Extinction spectra in Figure 6.7. Extinction is an appropriate physical quantity used to assess the effect of AgNPs interface. Figure 6.7 shows the extinction spectra for the plasmonic interfaces identical to those presented in Figure 6.5. Again increasing the annealing temperature shifts the extinction maximum to red. However, the influence of spacer layer is not as obvious as in the case of the total transmittance minima. Instead, the dielectric spacer layer seems to broaden the maximum of extinction spectra into the red rather than shifts the maximum toward the red.

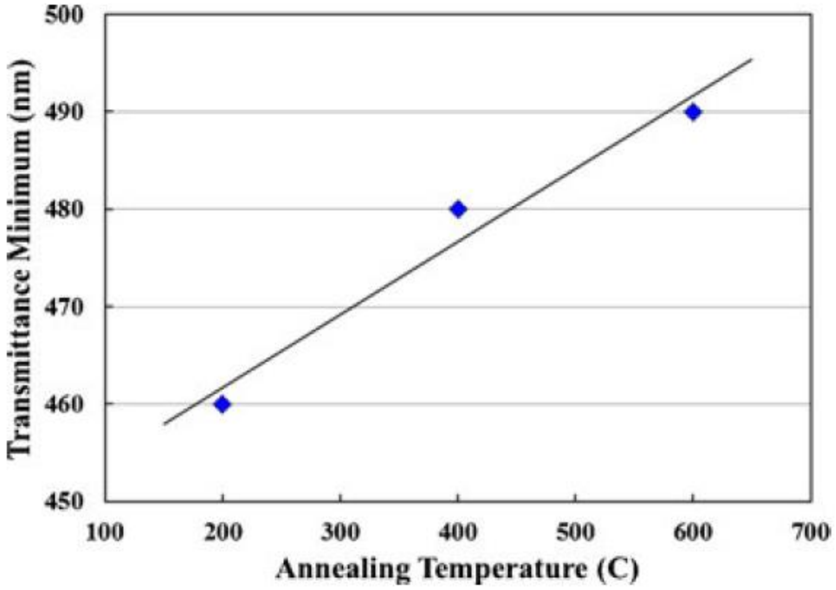

Fig. 6.6 The effect of annealing temperature on the LSP resonance wavelength. At 600 °C, however, the Corning glass surface deformed where Ag residue appears in the spaces between nanoparticles

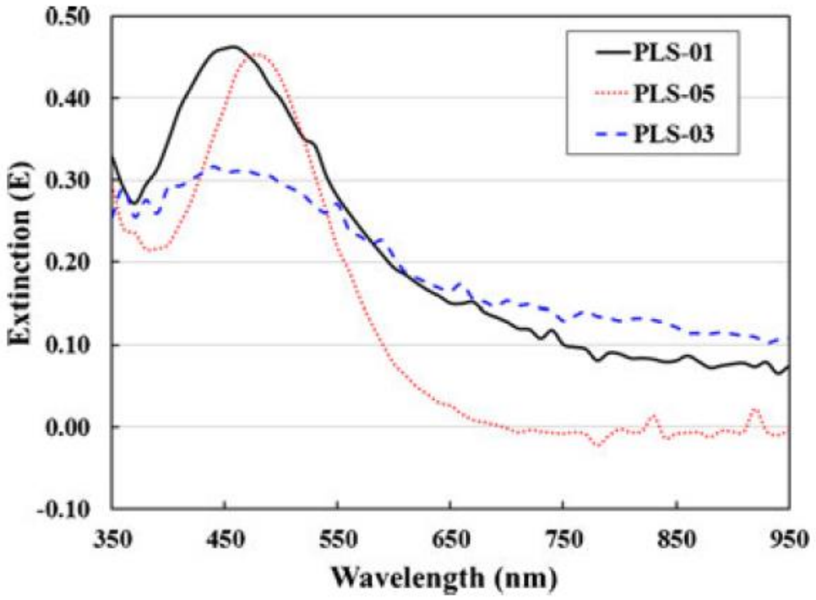

Fig. 6.7 Extinction spectra for various plasmonic layers showing the effects of dewetting temperature and dielectric spacer layer on the LSP resonance: Solid black line (PLS-01 consisting of AgNPs fabricated at 200 °C anneal on Corning glass), dotted red line (PLS-05 consisting of AgNPs fabricated at 400 °C on Corning glass), and dashed blue line (PLS-03 similar to PLS-01 covered by SiO_2 nm)

6.3 Fabrication of Double Plasmonic Layers on Corning Glass

Figure 6.8 shows the SEM images and the corresponding optical spectra for two double plasmonic interfaces separated by 20 nm SiO_2 dielectric spacer layer (PLS-06 in table 6.1) and by a 20 nm SiN_x dielectric spacer layer (PLS-08 in table 6.1). The images may appear misleading based on single plasmonic layer dewetting results as well as conservation of mass arguments. One anticipates the top plasmonic layer to include higher particle density than these images seem to indicate. It appears that only those nanoparticles that fall on top of another nanoparticle at the lower interface (those appearing suspended in air) have higher contrast spots while nanoparticles falling between those of the lower interface have lower contrast. This creates an issue in extracting the particle count and size distributions for the upper plasmonic layer. The optical responses for these two plasmonic interfaces are also presented in Figure 6.8. The extinction spectra are not only broadened but appear to consist of two distinct components corresponding to the two AgNPs interfaces and the dielectric spacer layers in each interface. AgNPs formation on top of sputtered SiN_x and SiO_2 appear to be more spherical than those formed on Corning glass. AgNPs formed on sputtered SiN_x and SiO_2 spacer layers are consistent with those formed on sputtered Al:ZnO as discussed in chapter 5.

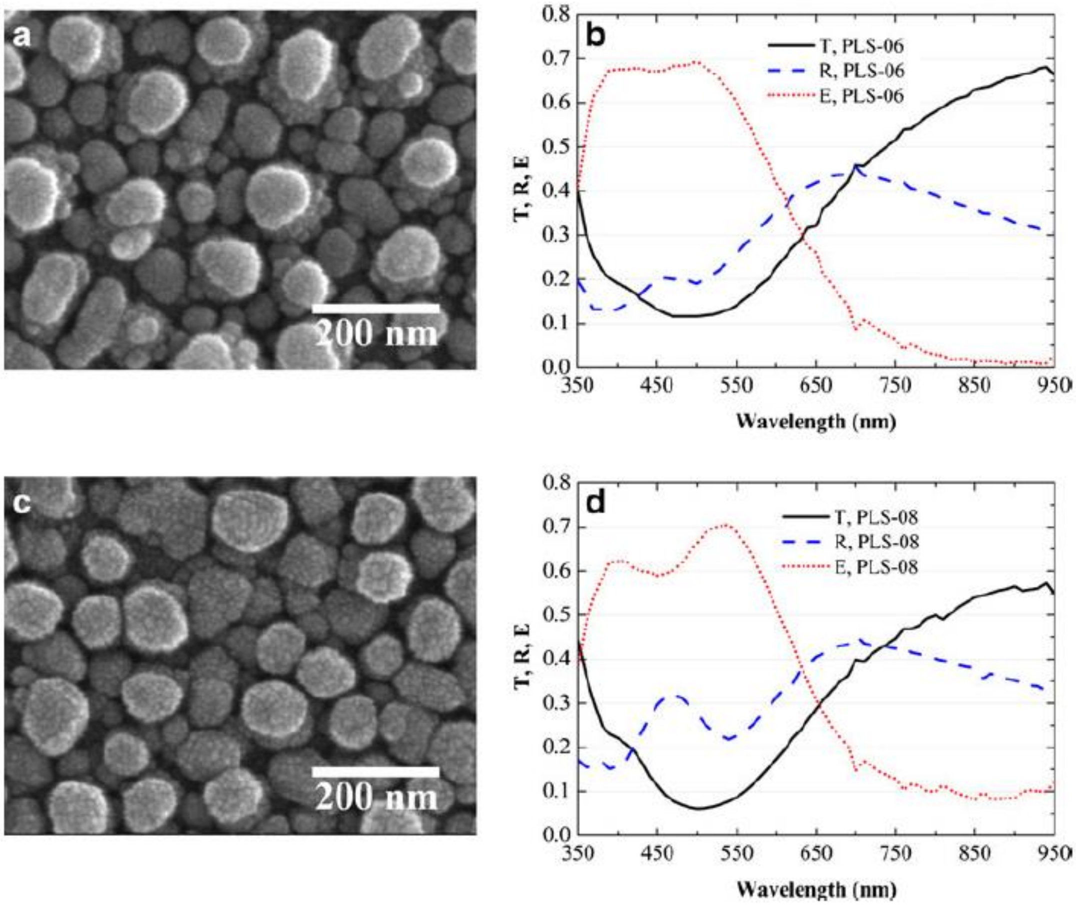

Fig. 6.8 SEM images and optical responses for two double layer plasmonic designs demonstrating the effects of dielectric constant of the spacer layer on the LSP resonance expressed by the minima in the total transmittance curves: (a) SEM and (b) optical response for PLS-06, (c) SEM and (d) optical response PLS-08. In the optical spectra: solid black line (total transmittance), dashed blue line (total reflectance), and dotted red line (extinction)

To investigate the influence of increased interaction between the two plasmonic layers in the interface, sample PLS-07 was constructed with a thinner SiO_2 dielectric spacer layer of 10 nm thickness separating the lower and upper AgNPs layers. The extinction spectrum exhibits a single narrow peak centered at 370 nm as shown in

Figure 6.9. The existence of narrow peak in extinction spectrum implies that the dielectric spacer layer thickness of 10 nm is not perfectly continuous causing the two AgNPs layers to make contact and form a single plasmonic interface of apparently connected AgNPs.

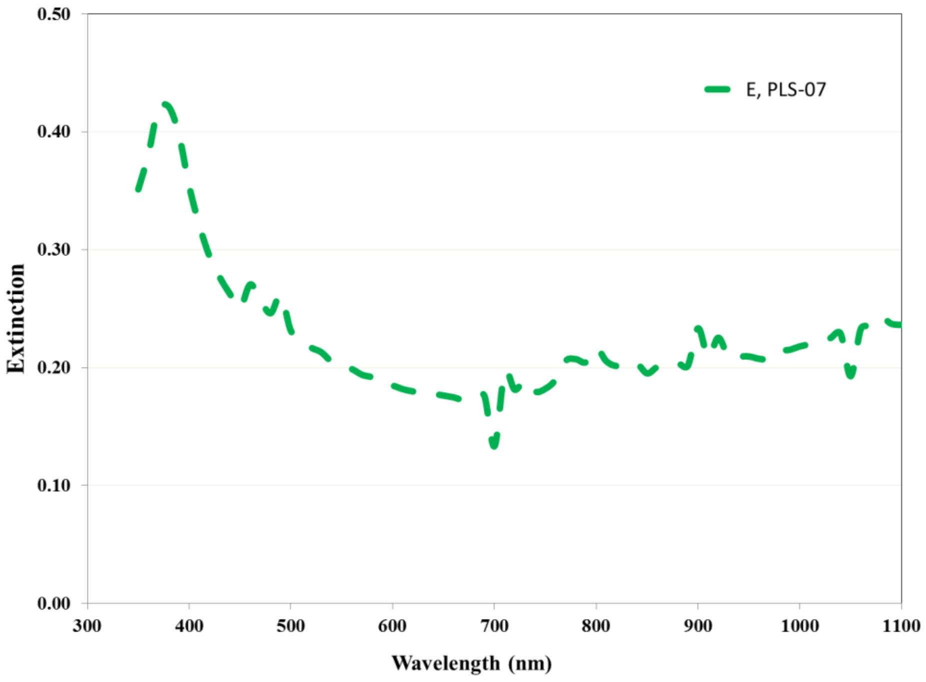

Fig. 6.9 Extinction spectrum of PLS-07

6.4 Enhanced Optical Extinction and Spectral Photocurrent of a-Si:H

Figure 6.10 shows the extinction spectra of two single (PLS-01 and PLS-03 before subsequent a-Si:H deposition) and two double layer (PLS-06 and PLS-08 before subsequent a-Si:H deposition) plasmonic interfaces along with that of the reference set consisting of 250 nm a-Si thin film deposited on Corning glass (PLS-Si). Extinction spectrum of a-Si:H exhibits oscillations arising from the interference between the incident light and the light reflected off the rear a-Si:H/ Corning glass interface.

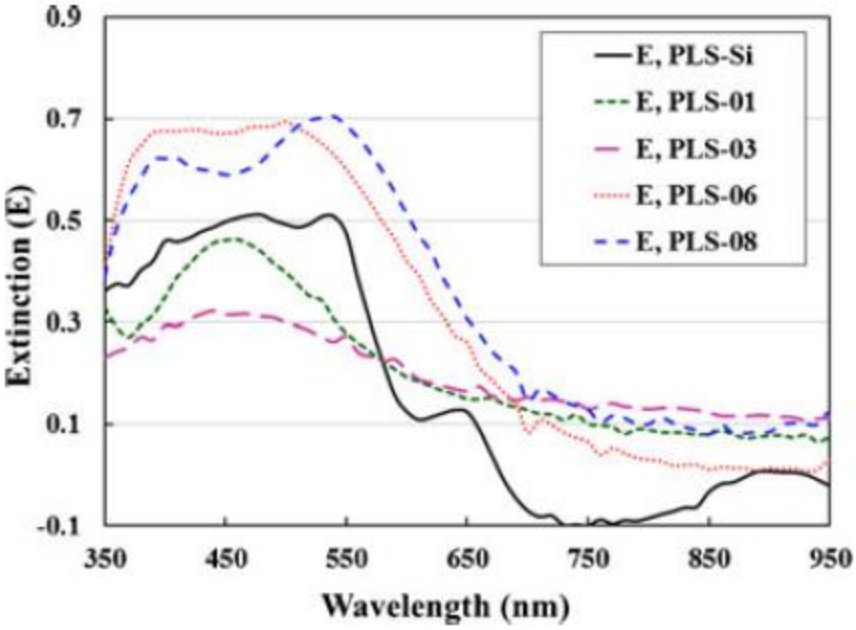

Fig. 6.10 Extinction spectra of two single and two double layer plasmonic interfaces compared to that of reference sample (250 nm a-Si:H on Corning glass)

The extinction spectra of the 250 nm a-Si:H film deposited on top of a single plasmonic interface dewetted at 400 °C (PLS-05) and a double plasmonic interface that consists of lower plasmonic layer dewetted at 400 °C and upper plasmonic layer dewetted at 200 °C (PLS-08) with 20 nm SiN_x spacer layer separating them, and that of the reference set (PLS-Si) are depicted in Figure 6.11. Both the single and the double plasmonic interfaces extend the extinction spectrum and thus the light absorption in a-Si:H film toward the red. The influence of the second plasmonic layer in the double interface is smaller than that of a single layer dewetted at the same temperature as the lower plasmonic layer (400 °C).

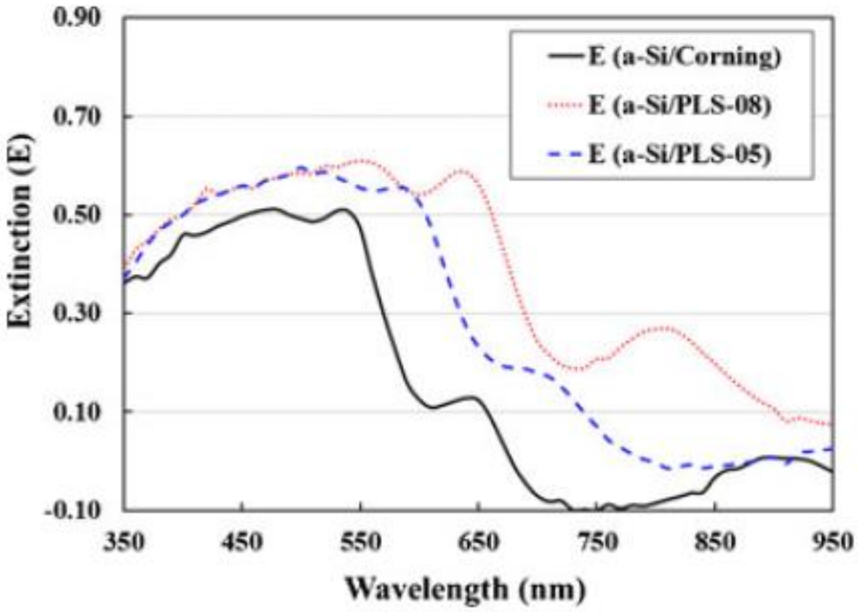

Fig. 6.11 Extinction spectra of the 25-nm a-Si:H film deposited on a single plasmonic interface (PLS-05 dashed blue line) and a double plasmonic interface (PLS-08: dotted red line) compared to that of the reference (PLS-Si: solid black line)

The influence of the these plasmonic interfaces on the photoconductivity of an a-Si:H film deposited on the interfaces are examined and compared to the reference sample with no plasmonic interfaces (PLS-Si). During current measurements, light is shone from the Al contact/a-Si:H side (opposite from the plasmonic interface) while applying a voltage bias from -10 to + 10 V. The total photocurrent obtained under white light decreased for all plasmonic interfaces and the reduction is more pronounced for the double plasmonic interfaces. This photocurrent reduction has been reported by several research groups and may be attributed to possible parasitic losses which reduce reflection and increase absorption at the rear interface [104].

Figure 6.12 shows the photocurrent measured at 10 V bias versus wavelength as well as the extinction spectrum for a-Si:H thin film deposited on the single plasmonic interface as indicated in PLS-05 at each wavelength in the range of 350 – 950 nm with 25 nm interval. The spectral photocurrent and extinction spectrum versus wavelength of the reference sample (PLS-Si) are also plotted. A relative yet appreciable photocurrent enhancement at the lower band gap edge (600 ~ 700 nm) can be clearly seen in Figure 6.12. This photocurrent enhancement correlates well with the broadening that appears in the extinction spectra. As shown in the figure, the extinction spectrum of a-Si:H deposited on PLS-05 plasmonic interface is clearly broadened into the red compared to that of flat a-Si:H thin film deposited on Corning glass (PLS-Si). This result suggests that there is enhanced scattering by the fabricated single plasmonic interface into the a-Si:H absorber layer promoting more light absorption and thus more photo conversion.

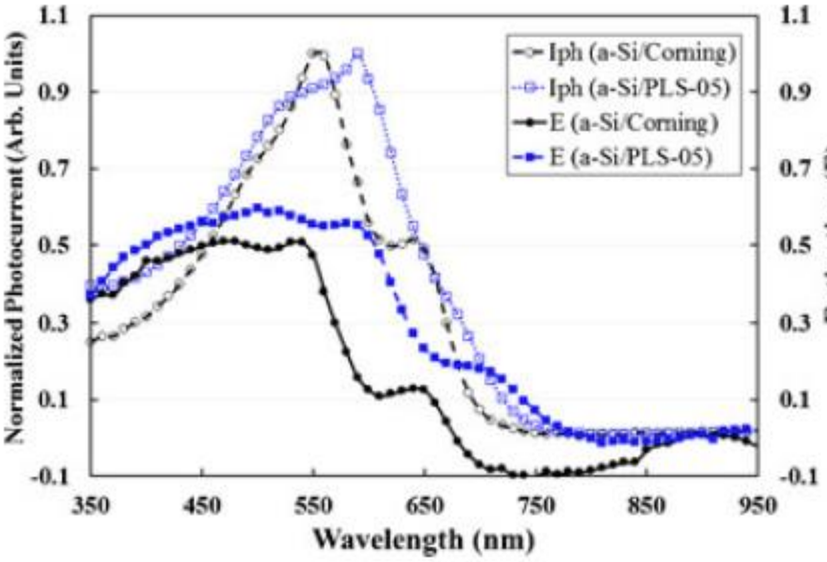

Fig. 6.12 Normalized spectral photocurrent (open blue squares) and the extinction spectrum (solid blue squares) for a-Si:H thin film deposited on PLS-05 compared with the normalized photocurrent (open black circles) and extinction spectrum (solid black circles) for the reference sample consisting of a-Si:H thin film co-deposited on Corning glass substrate. Both photocurrent curves are normalized to the same maximum current

The influence of the double plasmonic interface on the spectral photocurrent is manifold. Figure 6.13 shows the spectral dependence of the photocurrent measured by applying a similar 10 V bias at 25 nm wavelength increments along with the extinction spectrum for a-Si:H thin film deposited on the double plasmonic interface as indicated in PLS-08. Again the spectral photocurrent and extinction spectrum versus wavelength of the reference sample (PLS-Si) are also plotted. The extinction spectrum of a-Si:H deposited on a double plasmonic interface is also found to extend into the red but the photocurrent enhancement is clearly lower. This result suggests that absorption rather than scattering dominates the plasmonic interface response even in this spectral range.

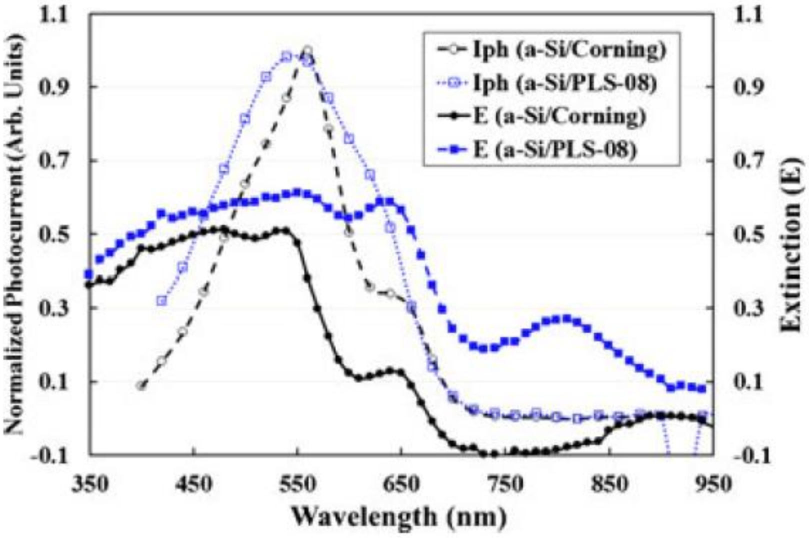

Fig. 6.13 Normalized spectral photocurrent (open blue squares) and the extinction spectrum (solid blue squares) for a-Si:H thin film deposited on PLS-08 compared with the normalized photocurrent (open black circles) and extinction spectrum (solid black circles) for the reference sample consisting of a-Si:H thin film co-deposited on Corning glass substrate. Both photocurrent curves are normalized to the same maximum current

CHAPTER 7

COMBINED PLASMONIC SILVER NANOPARTICLES AND TEXTURED AL:ZNO AS A SINGLE LIGHT TRAPPING INTEFRACE FOR ENHANCED OPTICAL ABSOPTION AND SPECTRAL PHOTCURRENT IN A-SI:H THIN FILMS

In this chapter we fabricate HCl textured Al:ZnO thin films with high total and diffuse transmittance and low electrical resistivity. The influence of these surface textures on the Ag dewetting and scattering mechanism of the AgNPs will be discussed in terms of optical and electrical properties. We further investigate the effect of AgNPs on the optical response of flat (as deposited) and HCl textured Al:ZnO. Intilially, reseach focused on nanoscale scatterers such as MNPs embedded in a dielectric medium or on microscale scatterers such as the bare naturally rough Al:ZnO. Enhanced light trapping by these schemes was not sufficient for solar cell devices. We moved one step further and combined both effects by fabricating plasmonic nanoparticles on textured Al:ZnO in a single light trapping interface separated by 20-nm SiO_2 spacer layers from the a-Si:H absorber (see Figure 7.1 (d)). Combined Al:ZnO and AgNPs act as single light trapping interfaces that can be integrated to the front surface of a-Si:H thin film solar cells in a superstrate configuration. At the end of this chapter, we will present the great potential of AgNPs fabricated on textured Al:ZnO as an advanced light-trapping interface to enhance the photoresponse of a-Si:H as a representation of enhanced light trapping. The data and results presented in this chapter are published in Optical Materials Express [91] and in Physica Status Solidi [105].

7.1 Samples Preparation

A total of four types of plasmonic designs consisting of AgNPs dewetted on top of as-deposited and textured Al:ZnO films. Designs of samples structure are listed in table 7.1. A total of 1250 nm thick Al:ZnO films were sputtered on the given

25 cm x 25 cm Schott glass at 250 °C substrate temperature to ensure high crystallinity and high transparency of sputtered Al:ZnO films. Textured Al:ZnO coated superstrates were obtained using a single step wet chemical etching in 5% diluted HCl for 30 seconds. AgNPs were fabricated by the standard dewetting technique starting with 15 nm Ag film sputtered at room temperature on as deposited and textured Al:ZnO and followed by annealing at 200 °C – 300 °C in nitrogen environment for 1 hour as was discussed in chapters 5 and 6.

Table 7.1 Design of samples structure

Sample Name	Substrate	Step 1	Step 2	Annealing	Step 4	Step 5
Sample A	Schott Glass	1250 nm flat Al:ZnO	Reference flat Al:ZnO		20 nm SiO_2	250 nm a-Si:H
Sample B			15 nm Ag	200 °C		
Sample C			15 nm Ag	300 °C		
Sample D		HCl textured Al:ZnO	Reference textured Al:ZnO			
Sample E			15 nm Ag	200 °C		
Sample F			15 nm Ag	300 °C		

As shown in table 7.1, a total of six samples were prepared. Set A consists of identical samples of 250 nm a-Si:H deposited on flat (non-textured) Al:ZnO as reference. Set B consists of identical a-Si:H samples deposited on the AgNPs fabricated by the dewetting technique at 200 °C on flat Al:ZnO. Set C is the same as set B except that the AgNPs dewetting temperature is 300 °C. Set D consists of identical 250 nm a-Si:H deposited on textured Al:ZnO as a reference. Set E consists of identical a-Si:H films deposited on AgNPs dewetted at 200 °C on textured Al:ZnO. Set F is the same as set E except that the AgNPs were dewetted at 300 °C. All the plasmonic nanoparticles are separated by a 20-nm SiO_2 spacer layer from the a-Si:H absorber. Samples prepared by deposition of the same a-Si:H and SiO_2 film on bare Schott glass substrates were used as references for thickness and bandgap measurement using Spectroscopic Ellipsometry (SE). Using this technique, the thickness of a-S:H is measured to be ~250 nm thick and has a bandgap of 1.65 eV while the SiO_2 spacer is ~20 nm in thickness.

Samples are prepared for spectral photoconductivity measurements by evaporating Al electrodes on the a-Si:H side as discussed in section 4.2. Before the spectral dependence of photocurrent was measured, we verified that at the extreme biases of – 1 and +1 V, at which the photocurrent is measured, the electrical contacts deposited by thermal evaporation remain ohmic. The final structure of typical samples ready for photocurrent measurements is depicted in Figure 7.1. In all optical and electrical measurements, the light was shone on the glass side to mimic the superstrate configuration of a typical a-Si:H thin film solar cell.

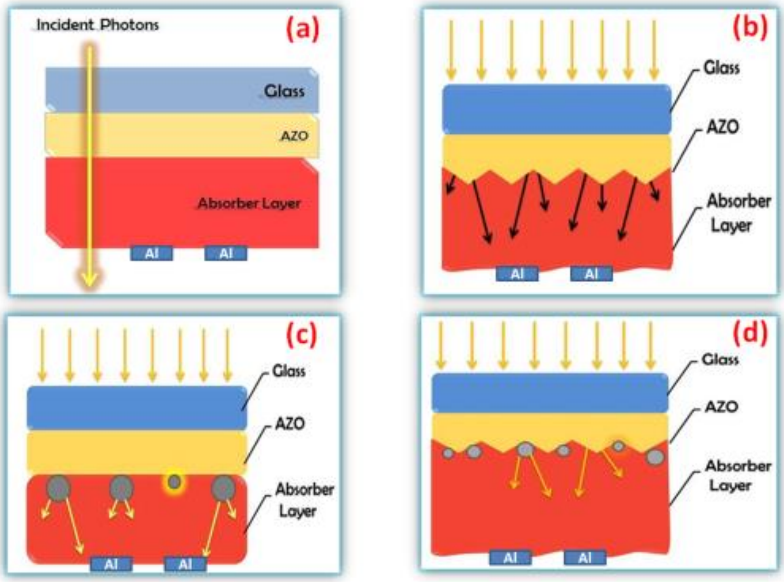

Fig. 7.1 Schematic diagram of a typical superstrate configuration for photocurrent measurements of a-Si:H thin film on (a) flat Al:ZnO, (b) textured Al:ZnO, (c) AgNPs on flat Al:ZnO, and (d)AgNPs on textured Al:ZnO. SiO_2 spacer layer between a-Si:H thin film and AgNPs/Al:ZnO layer is not shwon to reduce confusion

7.2 Characterizations of Flat and Textured Al:ZnO

Figure 7.2 shows the SEM cross-sectional views of as deposited (Sample A) and textured Al:ZnO (Sample C) prepared on Schott glass substrates. The 1250 nm initial thickness of as deposited Al:ZnO is reduced to 816 after texturing with 5%

HCl for 30 seconds. Difference in surface morphologies are clearly seen in the figure where the as deposited Al:ZnO appears to have flat surface while textured Al:ZnO appears to exhibit vertical grooves.

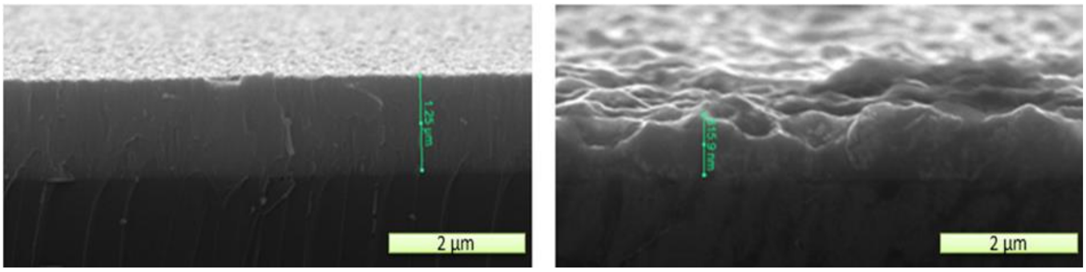

Fig. 7.2 SEM images of as deposited Al:ZnO (left) and textured Al:ZnO (right).

Figure 7.3 displays top view SEM images of surface morphology along with AFM layouts of as deposited (flat) and HCl-textured Al:ZnO. These images reveal dramatic changes to the surface morphology after HCl texturing. SEM images display smaller surface features present on the surface of as deposited Al:ZnO. Texturing Al:ZnO with HCl produces crater-like valleys which appear clearly on the surface. The average surface roughness of as deposited (flat) Al:ZnO is 16 nm whereas it is 157 nm for HCl textured films.

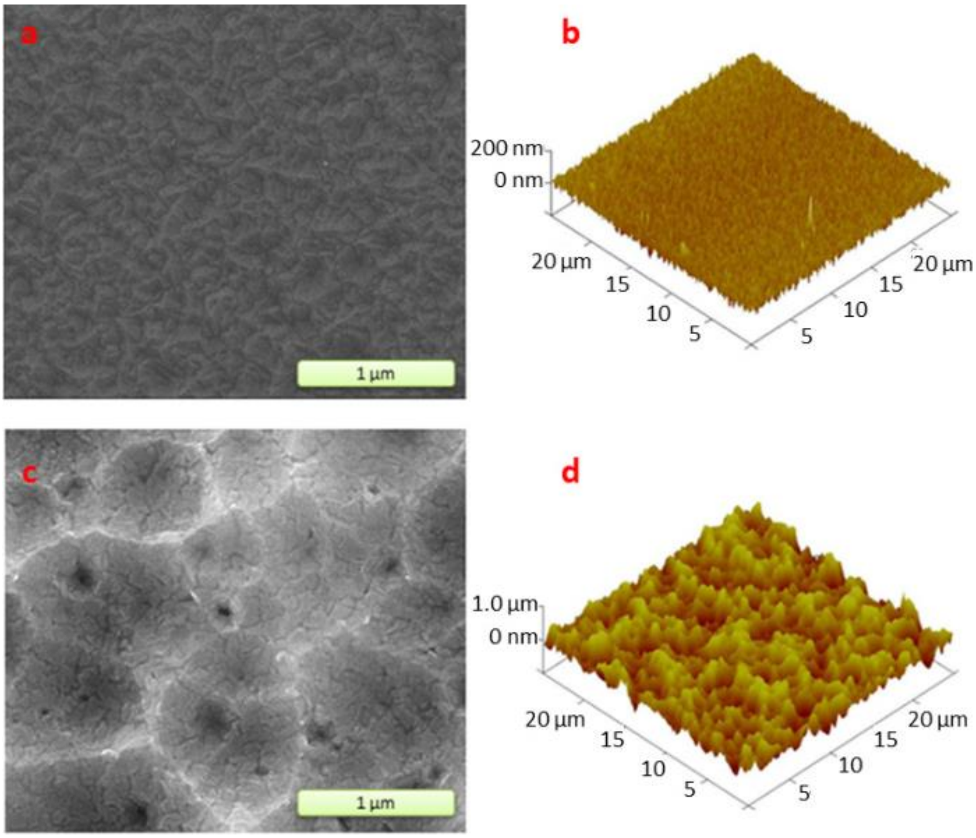

Fig. 7.3 (a) SEM image and (b) AFM topography of flat Al:ZnO, (b) SEM image and (d) AFM topography textured Al:ZnO. The AFM analyses were taken by considering 625 µm^2 large square areas

Texturing of flat Al:ZnO in 5% diluted HCl for 30 seconds is successful in increasing both the total and diffuse transmittance while maintaining superior electrical properties. Using the 4-point probe the sheet resistance of flat Al:ZnO film is found to be 1.3 Ω/□ and that of textured Al:ZnO film is found to be 8 Ω/□. This increase in sheet resistance upon texturing is expected since the textured Al:ZnO film is thinner and a lot more disruptive for the electron conduction due to its rougher surface morphology and the presence of higher trap charges concentration than flat film. Figure 7.4 shows, in column from left to right the measured total and diffuse transmittance, and the calculated haze is transmittance versus wavelength, respectively. These data were measured by illuminating the Schott glass side as illustrated in the experimental details (Figure 4.1). The presence of oscillating crests and trough in the total transmittance curve of the as deposited (flat) Al:ZnO film is attributed to the interface, induced by thick Al:ZnO film, between the incident beam and the reflected one. It is clear that the as deposited Al:ZnO film has very low diffuse transmittance, lower than 1%, and thus results in a low calculated haze over the entire spectral range. This low value is due to miniature average surface roughness of 16 nm for flat Al:ZnO film. In line with the increase surface roughness, the diffuse transmittance of textured Al:ZnO film shows a pronounced increase over the whole wavelength range. In particular a diffuse transmittance maximum of about 70%, corresponding to an impressive 3 orders of magnitude increase, is attained at 550 nm wavelength. The calculated haze in transmittance of textured Al:ZnO film screens a broad spectral range which is highly correlated to the vast increase in roughness.

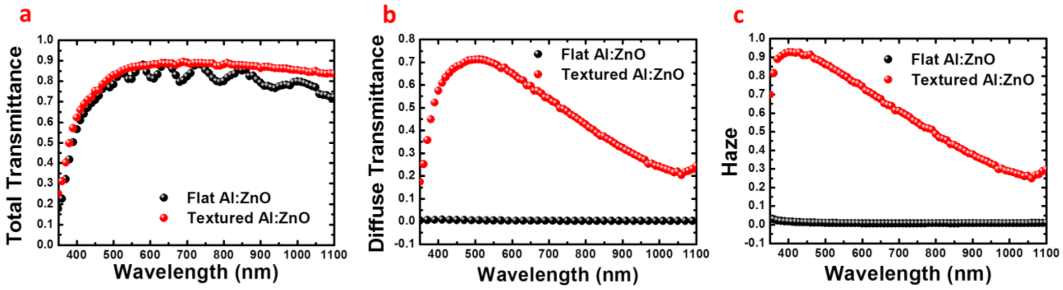

Fig. 7.4 (a) Total transmittance, (b) diffuse transmittance, and (c) haze of bare flat (black) and textured Al:ZnO (red)

7.3 Fabrication of AgNPs on Flat and Textured Al:ZnO

In order to investigate the influence of AgNPs on the flat and textured Al:ZnO films, we prepared samples B, C, D, and E. Figure 7.5 shows the SEM images and the corresponding optical responses for samples B and C bearing both flat Al:ZnO and AgNPs, before subsequent SiO_2 and a-Si:H depositions, one prepared by annealing at 200 °C (a) and the other at 300 °C (b). The optical response of bare sample (Sample A) is also included in the plots in order to serve as a reference to demonstrate the effect of AgNPs on the optical response. Annealing Ag thin film on flat Al:ZnO layer at 200 °C results in AgNPs, yet the dewetting of the Ag on the flat Al:ZnO appears to be rather incomplete. The sample annealed at 300

°C, on the contrary, appears to have well-formed AgNPs with an increased average particle size with respect to 200 °C anneal.

Since the optical response measurements were taken by illuminating the glass superstrate side, it is not possible to extract the LSP resonance from the total reflectance measurements. This is because at LSP, the incident light scattered by AgNPs, couples into Al:ZnO where the density of optical modes (or n) is higher than that of air. Thus in our optical measurements, the LSP resonance depicts itself in the form of a dip in the total transmittance curve. The sinusoidal fringes observed at the total reflection curves reveal the constructive and destructive interference between the light reflected at the Al:ZnO/AgNPs interface and the glass/Al:ZnO interface. The LSP resonance dip in the total transmission curve occurs at about 540 nm for sample B annealed at 200 °C, which is observed to redshift to about 580 nm for sample C annealed at 300 °C. This red shift is expected since the average size of AgNPs increases by increasing the dewetting temperature from 200 °C to 300 °C [71].

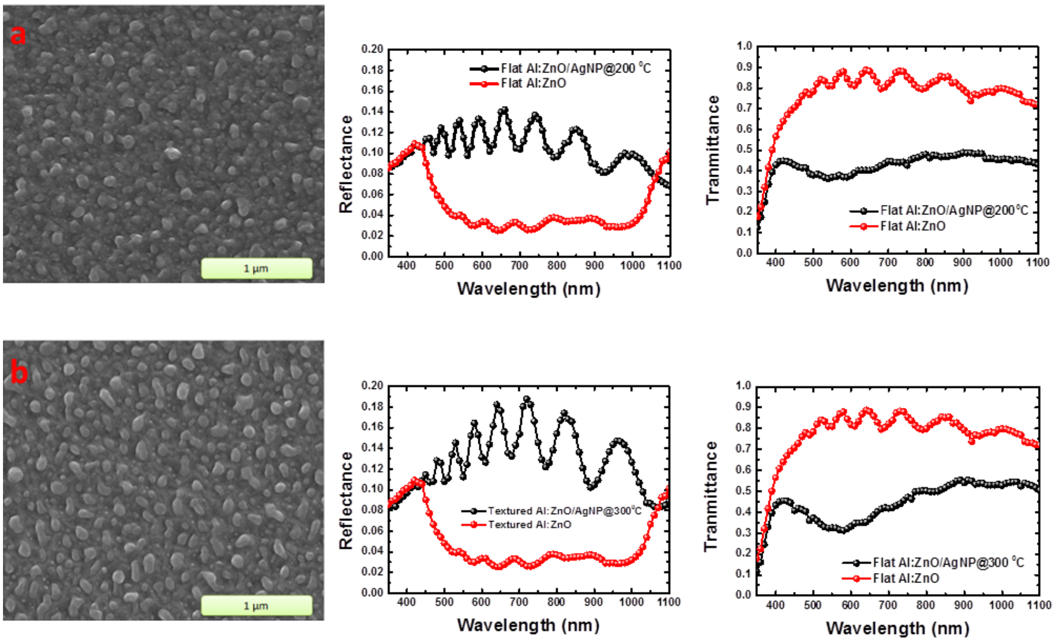

Fig. 7.5 SEM, total reflection and total transmittance response of AgNPs formed on flat Al:ZnO at annealing temperature of (a) 200 °C (Sample B) and (b) 300 °C (Sample C). Total reflection and total transmittance (in red) of reference sample consisting of bare flat Al:ZnO (Sample A) are also plotted

Figures 7.6 and 7.7 show the SEM images and the optical response of textured Al:ZnO samples without and with AgNPs fabricated by annealing at 200 °C (Sample E) and 300 °C (Sample F), respectively. Dewetting of Ag film on textured Al:ZnO at 200 °C results in rather irregularly elongated (bean-like) AgNPs together with smaller spherical AgNPs dispersed between larger AgNPs as can be clearly seen in Figure 7.6(a) and further magnified in Figure 7.6(c). This result is consistent with the literature. Tayneli et al. have shown that the FWHM of AgNPs size distribution increases with increasing surface roughness of the underlying substrate for Ag films dewetted at 200 °C [71]. Those elongated AgNPs present in the sample E annealed at 200 °C are larger in size than that of the AgNPs formed in sample F annealed at 300 °C as shown in Figure 7.7(a) and 7.7(c). The surface roughness apparently hinders the complete coalescence of AgNPs at 200 °C causing the formation of larger elongated AgNPs between smaller and more spherical AgNPs. Increasing the dewetting temperature to 300 °C allows rapid dewetting of Ag thin film through larger surface features producing well-separated spherical AgNPs. Sample F annealed at 300 °C has higher measured total transmittance. This is in accordance with the reduced number of mostly absorbing smaller AgNPs as can be seen from SEM images with respect to sample E annealed at 200 °C, for all wavelengths above 640 nm. Plasmonic resonance dip occurs at 530 nm for sample E dewetted at 200 °C and blue shifts to 520 nm for sample F dewetted at 300 °C. The observed blue shift in LSP resonance dips with increasing dewetting temperature can be explained by three possible mechanisms: (i) It is a result of reduced interaction of AgNPs with increased inter-particle spacing (ii) It reflects the size difference between larger AgNPs formed by annealing at 200 °C and smaller AgNPs formed by annealing 300 °C; (iii) It is a result of increased symmetry in the shape of AgNPs. Indeed, the resonance peake position is a product of the final configuration of the plasmonic interface; the size, the shape, and the inter-particle spacing. For example, in the 300 °C treated samples, the particle size is found smaller, more symmetric, and with a larger inter-particle distance than that of the samples treated at 200 °C shifting the LSP peak into blue. Again, no LSP resonance can be detected from the total reflectance measurement where the maximum scattering at LSP wavelength scatters preferentially towards Al:ZnO rather than air due to much higher index of refraction of Al:ZnO (n~1.8) with respect to air (n = 1) [106].

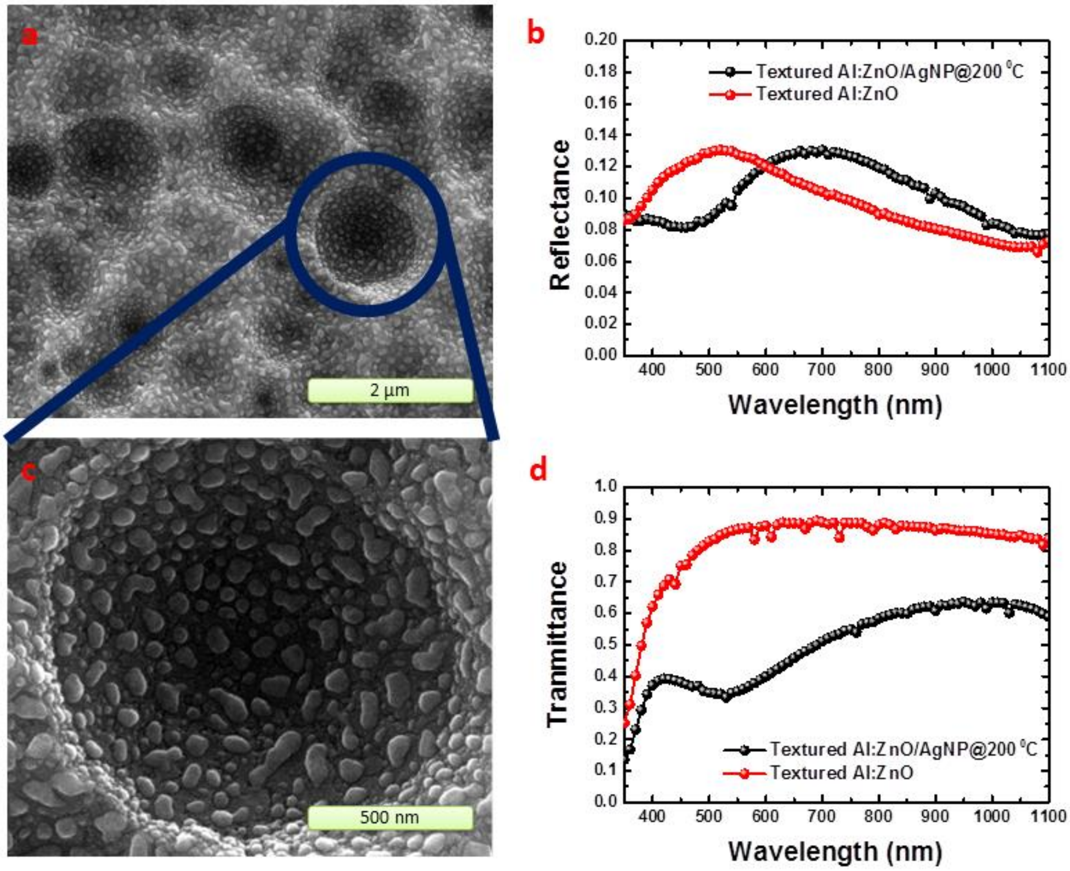

Fig. 7.6 (a), (c) SEM; (b) total reflection; and (d) total transmittance of sample E which includes AgNPs fabricated at 200 °C annealing temperature on textured Al:ZnO. Total reflection and total transmittance (in red) of bare textured Al:ZnO (Sample D) are also plotted

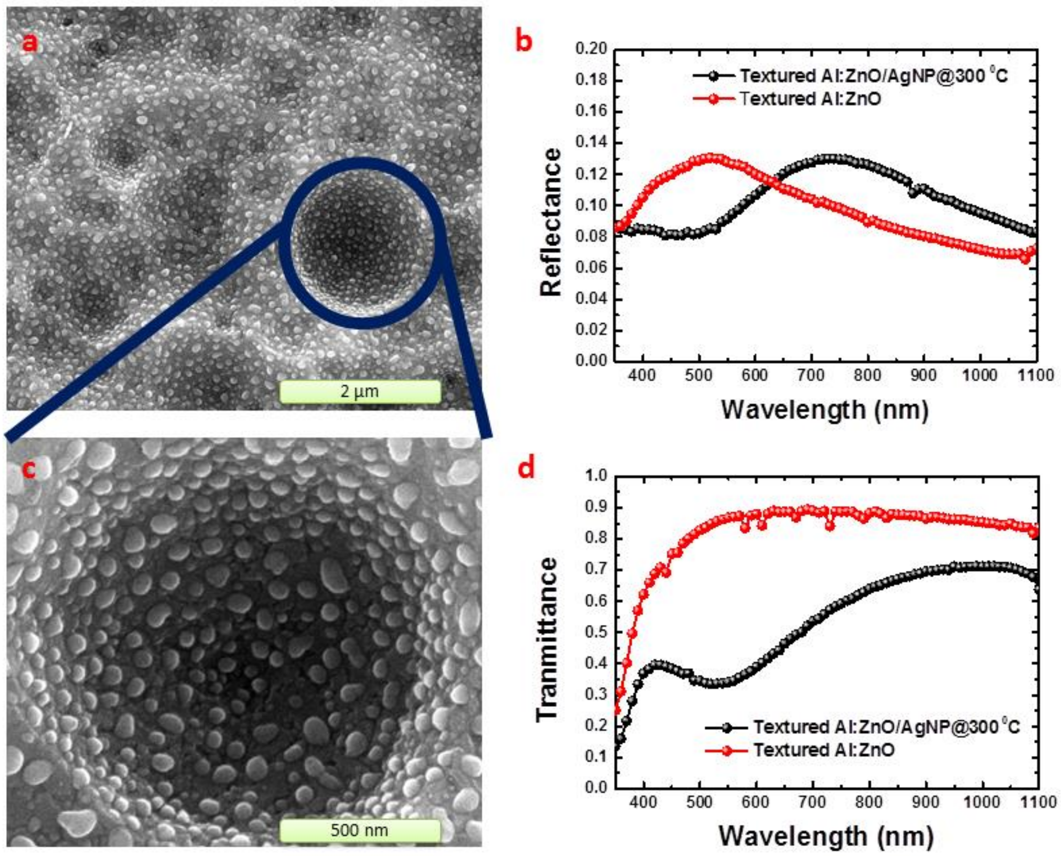

Fig. 7.7 (a), (c) SEM; (b) total reflection; and (d) total transmittance of sample F which includes AgNPs fabricated at 300 °C annealing temperature on textured Al:ZnO. Total reflection and total transmittance (in red) of bare textured Al:ZnO (Sample D) are also plotted

Figure 7.8 presents the influence of AgNPs on the diffuse transmittance of flat (a) and of textured (b) Al:ZnO. Scattering of AgNPs in all direction upon light excitation [106] and natural surface roughness induced by AgNPs on flat Al:ZnO slightly increases diffuse transmittance as compared to bare samples which further increases for sample C annealed at 300 °C, for the entire wavelength range (Figure 7.8(a)), where formed AgNPs are farther separated. This enhancement in diffuse transmittance is also detected by the calculated haze in transmittance as shown in Figure 7.8(c). Haze in transmittance shows an increase up to 14% at 640 nm wavelength for sample C annealed at 300 °C compared to bare flat Al:ZnO.

Decorating textured Al:ZnO with AgNPs reduces the diffuse transmittance as seen in Figure 7.8(b). Diffuse transmittance of samples E and F annealed at 200 °C and 300 °C, respectively, exhibits broad dip around LSP resonance wavelength. The haze of samples E and F is similar to that of the reference textured sample D as can be clearly seen by comparing the red, green and blue symbols in Figure 7.8(c). Thus we conclude that the formation of AgNPs on textured Al:ZnO reduces both diffuse (Figure 7.8(b)) and total (Figures 7.6(d) and 7.7(d)) transmittance of Al:ZnO but their ratio (the haze) is conserved throughout the entire spectrum.

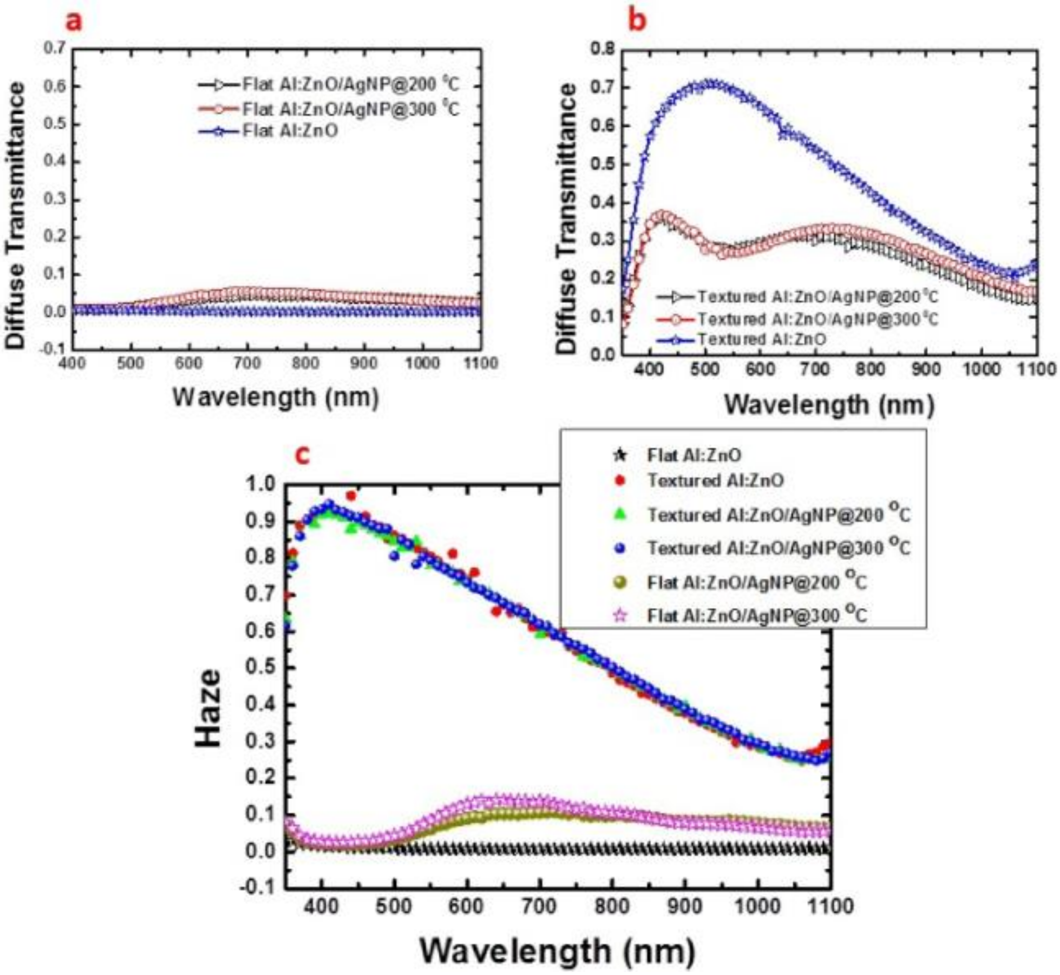

Fig. 7.8 (a) Diffuse transmittance of sample A: bare flat Al:ZnO and samples B and C: AgNPs fabricated on flat Al:ZnO by annealing at 200 °C and 300 °C, respectively; (b) Diffuse transmittance of sample D: bare textured Al:ZnO and samples E and F: AgNPs fabricated on textured Al:ZnO by annealing at 200 °C and 300 °C, respectively; (c) haze in transmittance of bare flat and bare textured Al:ZnO and of AgNPs fabricated on flat and textured Al:ZnO by annealing at 200 °C and 300 °C

The reduction in total transmittance has three origins. First contribution arises from the fact that light is scattered by AgNPs in all directions, yet mostly preferentially into Al:ZnO due to the asymmetry in the index of refraction of Al:ZnO and air [106]. The second contribution arrives from the intrinsic parasitic absorption of light in AgNPs; and the final contribution comes from light absorption by Al:ZnO and Schott glass substrate itself.

7.4 Dewetting of Thin Ag Film Sputtered on Textured Al:ZnO at Elevation Temperatures

To investigate the potential of elevated annealing temperatures to form plasmonically active AgNPs on textured Al:ZnO, we constructed two plasmonic interfaces as indicated in table 7.2

Table 7.2 Design of samples structure

Sample Name	Substrate	Step 1	Step 2	Annealing
Sample G	Schott Glass	Textured Al:ZnO	15 nm Ag	400 °C
Sample H			15 nm Ag	500 °C

In samples G and H, 15 nm thick Ag film sputtered on textured Al:ZnO is dewetted at 400 °C and 500 °C, respectively.

In Figure 7.9, we show the SEM images of samples G and H. Increasing the annealing temperature above 400 °C produces large and farther separated AgNPs on textured Al:ZnO. Similar results were obtained for the case of flat Al:ZnO as discussed in Chapter 5. These samples display no LSP resonance where the median diameter of the dispersed AgNPs is larger than 500 nm. Additionally it should be kept in mind that annealing temperatures exceeding 300 °C can be potentially damaging to the Al:ZnO as well as to Si based solar cells as the p-n junction gets adversely affected from thermal diffusion of dopants at temperatures above this value [92].

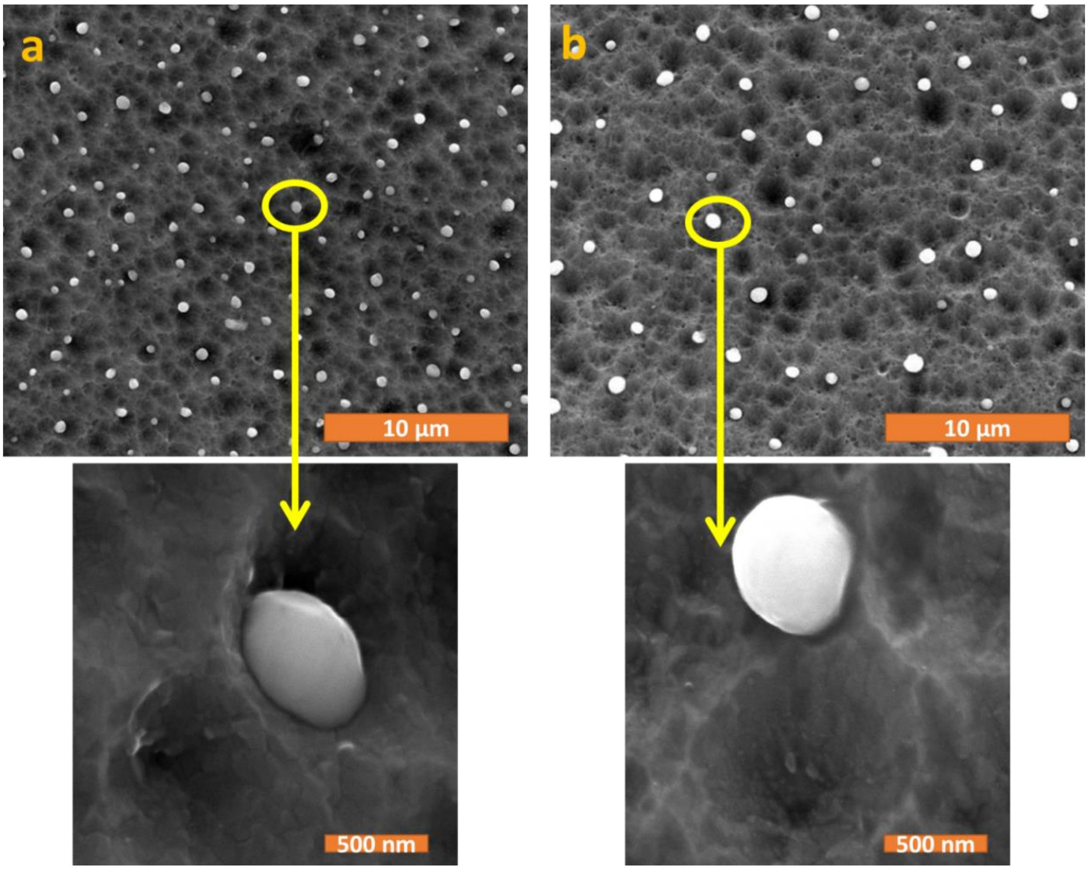

Fig. 7.9 SEM images of AgNPs formed on textured Al:ZnO by annealing at (a) 400 °C and (b) 500 °C. From magnified SEM images, it is clear that formed AgNPs exhibit diameter larger than 500 nm

7.5 Enhanced Optical Extinction and Spectral Photocurrent of a-Si:H

In order to examine the light-trapping efficiency of the interfaces indicated in table 7.1, we deposited 250 nm a-Si:H thin film on top using a 20 nm thick SiO_2 spacer layer. The purpose of the 20 nm thick SiO_2 spacer is to passivate the a-Si:H absorber and reduce possible carrier recombination induced by the AgNPs and to optimize the fraction of light preferentially scattered into a-Si:H, which is contolled primarily by the scattering cross section of the Ag nanoparticles themselves and their distance from the absorber layer [73,84,86]. Figure 7.10 displays the optical Extinction spectra of samples A through F.

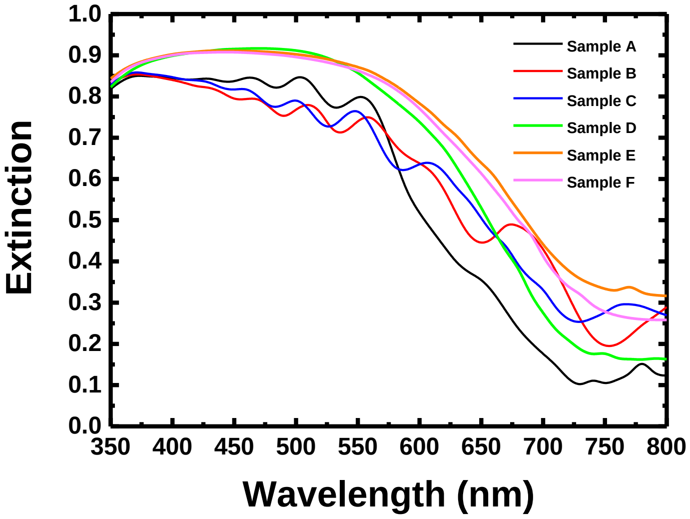

Fig. 7.10 Extinction spectra of a-Si:H deposited on 6 different light trapping interfaces as presented in samples A through F. The red bar at 750 nm corresponds to the band edge of a-Si:H thin film

The oscillations present in samples A, B, and C are due to interference between the incident light and light reflected by glass/Al:ZnO and/or the Al:ZnO/AgNPs/SiO_2 interfaces. Reference sample A consisting of a-Si:H thin film on flat Al:ZnO/SiO_2, has higher extinction than samples B and C with the plasmonic interface integrated to the flat Al:ZnO over the spectral range of < 570 nm and 580 nm for AgNPs fabricated at 200 °C and 300 °C, respectively. Above 570 nm and 580 nm for samples B and C, respectivley, extinction is higher than that of sample A. Reference sample D consisting of a-Si:H deposited on textured Al:ZnO/SiO_2 (green curve in Figure 7.10) has higher extinction compared with the reference sample (A) for all wavelength and higher extinction than samples B and C for all wavelength below 660 nm. In the wavelength range close to the band edge of a-S:H between 660-750 nm, a-Si:H thin films fabricated on flat Al:ZnO/AgNPs/SiO_2 (samples B and C) have higher optical extinction than a-Si:H fabricated on textured Al:ZnO (sample D). Integrating AgNPs at 200 °C (sample E) and 300 °C (sample F) on textured Al:ZnO increases the extinction for wavelengths above 540 nm compared to sample D. Sample E composed of AgNPs fabricated at 200 °C on textured Al:ZnO shows higher extinction for wavelegths above 540 nm (orange plot in Figure 7.10). Below 540 nm, we observed that samples D, E, and F have almost the same optical extinction.

Measured extinction above 750 nm (band edge of a-Si:H) is due to parasitic absorption of AgNPs and Al:ZnO. Extinction measures the light which is neither reflected nor transmitted by the absorber layer. To check whether the measured extinction is due to absorption by the absorber layer or lost in the Al:ZnO/AgNPs interfaces, we measured the photoresponse a-Si:H.

Figure 7.11 shows the photocurrent measured from samples A through F in the superstrate configuration, as shwon in Figure 7.1, versus wavelength.

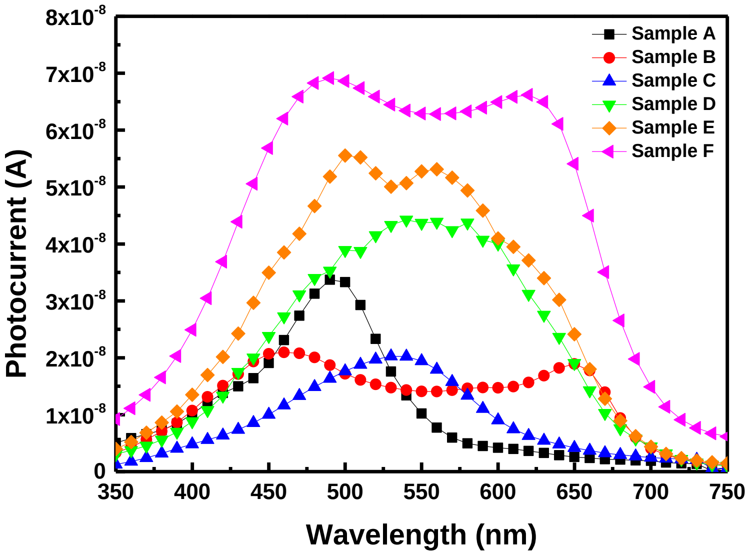

Fig. 7.11 Photocurrent versus wavelength of a-Si:H thin film deposited on 6 different light trapping interfaces in samples A through F as indicated in table 7.1

Textured Al:ZnO with high diffuse transmitance results in an increase of photocurrent in the a-Si:H absorber (green curve) for all wavelength compared to reference sample A (black curve). Incident photons scattered at the interface of textured Al:ZnO/a-Si:H interface results in a longer absorption path in a-Si:H resulting in higher absorption and photocurrent enhancement. AgNPs fabricated at 200 °C on flat Al:ZnO; sample B, results in reduced photocurrent for all wavelengths below 540 nm while enhancement is observed for wavelength close to band gap of a-Si:H as seen by the red curve of Figure 7.11. The lower photocurrent in this region for sample B agrees with the reduced measured extinction presented in Figure 7.10. Similar behavior is observed for sample C, where the enhancement of photocurrent is observed for wavelengths above 525 nm. For shorter wavelengths the reduction of photocurrent is attributed to the nonzero phase of AgNPs polarizability at these wavelengths. The photocurrent enhancement in the off-resonance region is due to the scattered field outflow resulting in enhanced radiative efficiency from AgNPs [107]. Finally, AgNPs fabricated on textured Al:ZnO and separated by SiO_2 (samples E and F), show higher photocurrent enhancement compared to the reference samples A (bare flat) and D (bare textured Al:ZnO) with the highest enhancement arising from AgNPs fabricated at 300 °C (sample F).

CHAPTER 8

POSITION AND THICKNESS OF DIELECTRIC SPACER LAYER SELECTION FOR IMPRESSIVE ENHANCED A-SI:H PHOTOCURRENT

In this chapter, we consider the enhancement of the spectral dependence of photocurrent in a-Si:H as a function of nanoparticle size and dielectric spacer layer thickness placed at the rear of the a-Si:H absorber as an indicator of enhanced light trapping. We use randomly assembled dewetting of AgNPs formed on the glass substrate and separated from the a-Si:H absorber by SiN_x spacer layers of different thicknesses to passivate the a-Si:H absorber and vary the interaction distance of the formed AgNPs from it. Then, we compare the enhancement in the spectral dependence of photocurrent due to plasmonic interfaces integrated to the front, rear and both front and rear surfaces of a-Si:H absorbers using a 30-nm SiN_x spacer layers. Plasmonic interfaces integrated to the front, back and both surfaces of photovoltaic thin films show different degrees of enhancement of light trapping depending on the position and thickness of the spacer layer.

8.1 Samples Preparation of AgNPs Placed at the Rear of a-Si:H Thin Film

Plasmonic interfaces consisting of AgNPs of two different average sizes are integrated to device-quality 150 nm thick a-Si:H thin films. Thin layers of SiN_x of different thicknesses are placed between the AgNPs the and a-Si:H absorber as shown in Figure 8.1. Again, AgNPs were fabricated on Schott glass substrates by dewetting of sputtered Ag thin film of 15 nm thickness at 220 °C or 420 °C for 1 hour in N_2 environment to generate plasmonic interfaces with two different average nanoparticle sizes (set-A and set-B, respectively). Silicon nitride films of 0, 30 and 60 nm in thickness were deposited simultaneously on both sets using the PECVD technique. Device-quality a-Si:H thin films were deposited on successfully fabricated plasmonic interfaces from each set in addition to several clean glass substrates to serve as references.

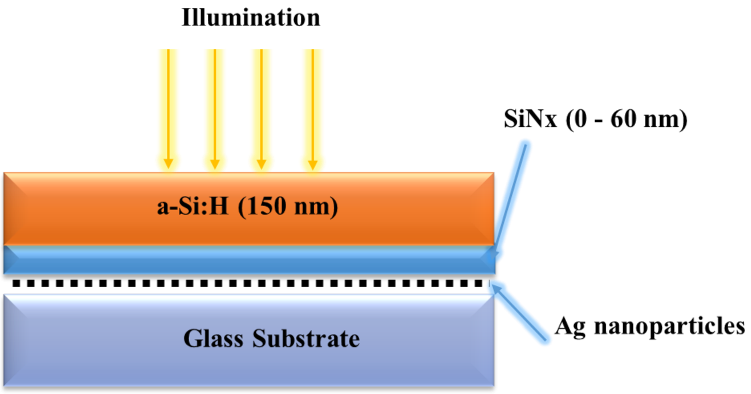

Fig. 8.1 Schematic diagram of plasmonic interfaces integrated to a-Si:H using a SiN_x with different thickness indicating illumination direction

A total of eight samples were prepared as indicated in table 8.1. Sample 1 consists of 150 nm a-Si:H on bare Schott glass substrate to serve as a reference. Samples 2 – 4 (set-A), consists of 150 nm a-Si:H deposited on top of formed AgNPs annealed at 220 °C with 0, 30 nm and 60 nm thick SiN_x dielectric spacer layers. Samples 5 - 7 (Set-B) consists of identical 150 nm a-Si:H thin film deposited on AgNPs annealed at 420 °C again with 0, 30, and 60 nm thick SiN_x dielectric spacer layers. To investigate the in-situ dewetting of as sputtered Ag thin film during the deposition of subsequent SiN_x and a-Si:H thin film, we constructed sample 8 consisting of 150 nm a-Si:H/60 nm SiN_x/15 nm as sputtered continuous Ag thin film. All samples were constructed on clean Schott glass substrates as follows:

Table 8.1 Plasmonic interfaces consisting of AgNPs integrated at the rear of a-Si:H

Set	Sample Name	Substrate	Plasmonic Interface	SiN_x (nm)	a-Si:H
Reference	1	Schott Glass	No	No	150 nm
Set-A	2		AgNPs Dewettet at 220 °C	0	
	3			30	
	4			60	
Set-B	5		AgNPs Dewettet at 420 °C	0	
	6			30	
	7			60	
	8		As sputtered 15 nm Ag	60	

8.2 Structural and Optical Properties of AgNP

Sputtered 15 nm silver films deposited on Schott glass were successfully dewetted by annealing in N_2 environment at 220 °C (samples 2 – 4) and 420 °C (samples 5 – 7) to form AgNPs of two different sizes. Figure 8.2 shows SEM images and particle size distributions of bare AgNPs for sample 3 formed by annealing at 220 °C (Figure 2 (a)) and for sample 6 formed by annealing at 420 °C (Figure 2(b)) before subsequent depositions. As we presented in chapter 3, the AgNPs dewetted at 400 °C appear more spherical and have narrower distribution of particle size centered at a mean particle diameter of ~100 nm. AgNPs dewetted at 220 °C, on the other hand, have what amounts of two distributions one centered at about 20 nm and another at about 100 nm in diameter. Similarly, in this study we observed that the two samples exhibit different particle size distributions. Sample 3 dewetted at 220 °C exhibits two distribution peaks centered at 20 nm and 110 nm suggesting the incomplete dewetting while sample 6 dewetted at 420 °C exhibits a more prominent peak at about 100 nm. The more spherical nature is related to more softening of Ag at higher annealing temperature. In consistent with the data presented in chapter 6, the difference in particle size distribution is associated with in a pronounce red shift in the LSP resonance each sample acquires. The SEM images of the same samples surface presented in Figure 8.2 but after a subsequent deposition of thin film of 30 nm SiN_x on top are shown in Figure 8.3. Again AgNPs dewetted at 420 °C (Figure 3 (b)) are clearly larger in size and more spherical in shape as compared to the AgNPs dewetted at 220 °C. In Figure 3 (c) we show the SEM image of sample 8 with 60 nm SiN_x layer deposited on top of as sputtered 15 nm continuous Ag film. In situ dewetting is attained during subsequent deposition of 60 nm SiN_x at 200 °C. Sample 8 appears to be partially dewetted, as can be seen in Figure 3 (c), yet exhibits some plasmonic effects associated with enhanced extinction and spectral photocurrent.

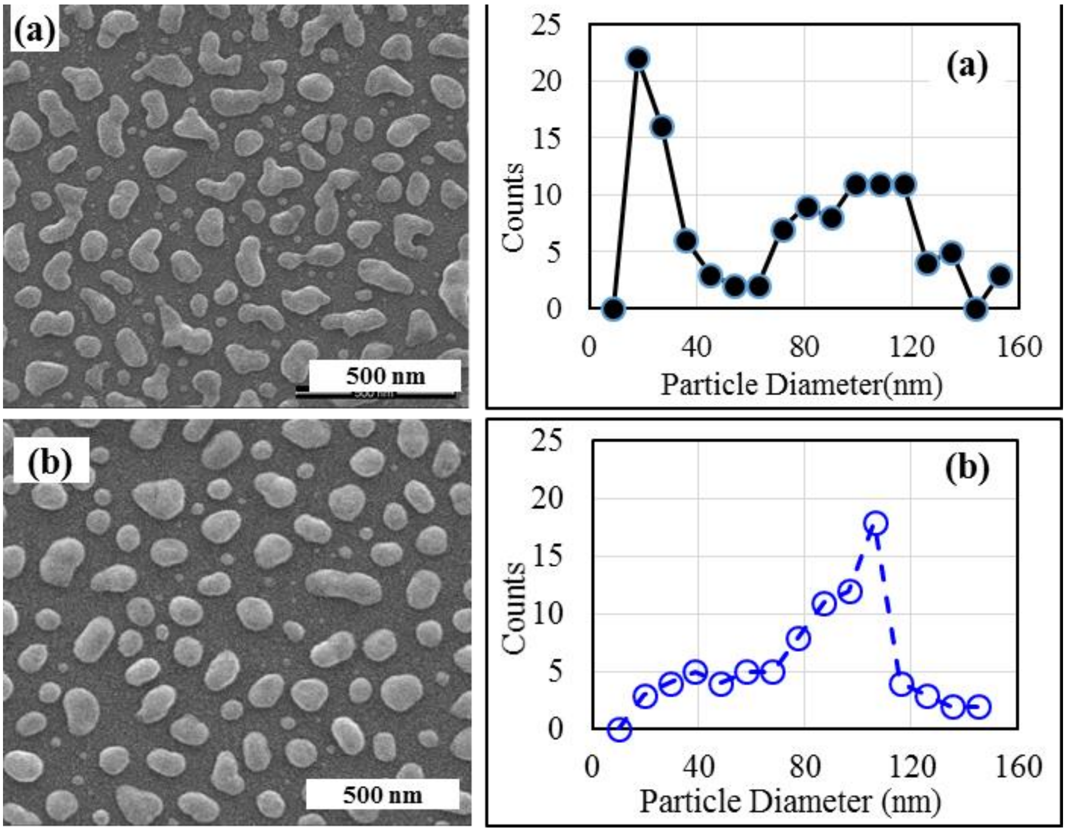

Fig. 8.2 SEM images and AgNPs size distributions of two samples of the two sets prepared by annealing at: (a) 220 °C (as indicated in sample 3) and (b) 420 °C (as indicated by sample 6); before subsequent depositions

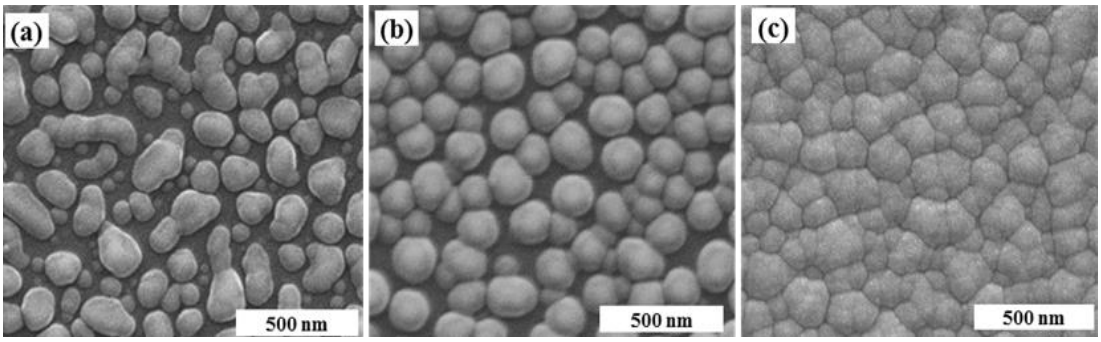

Fig. 8.3 SEM images of representative samples from the two sets dewetted at: (a) 220 °C (as indicated in sample 3) and (b) 420 °C (as indicated in sample 6) then covered by a 30-nm SiN_x dielectric spacer layer. Part (c) shows the SEM for sample 8 of as sputtered 15 nm Ag film partially dewetted during the SiN_x deposition at 200 °C and covered by 60 nm SiN_x spacer layer

Figure 8.4 shows the total transmittance spectra for the bare AgNPs in both sample sets versus wavelength. Distinctly clear minima are easily observed for the two sets. The samples prepared by annealing at 220 °C (Samples 2 – 4) show a minima at approximately 460 nm while those prepared by annealing at 420 °C (sample 5– 7) exhibit a minima at 510 nm. That fairly large red shift in the LSP resonance of ~50 nm is due to the difference in the size and shape of the resulting nanoparticles. It is worth mentioning that the scatter in the positions within each set is pretty small compared to the detected red shift for the two sets.

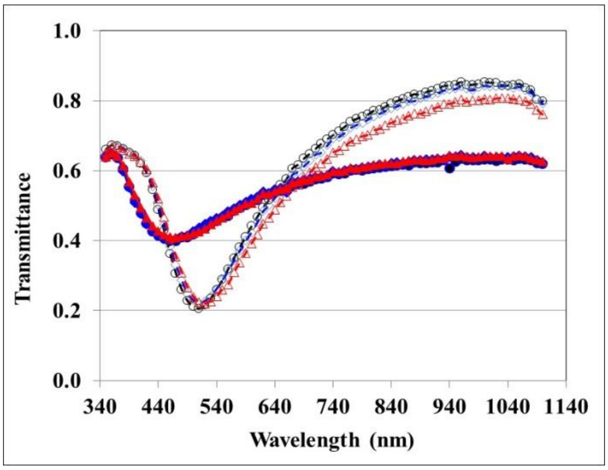

Fig. 8.4 Transmittance versus excitation wavelength for three identical samples form the two sets dewetted at 220 °C (solid symbols) and at 420 °C (open symbols)

Figure 8.5 shows the transmittance for the same two sets after SiN_x spacer layers of different thicknesses are deposited as indicated. As expected, all transmittance minima are broadened and red shifted by the SiN_x spacer because it has a larger dielectric function than air and the shift is proportional to the SiN_x thickness.

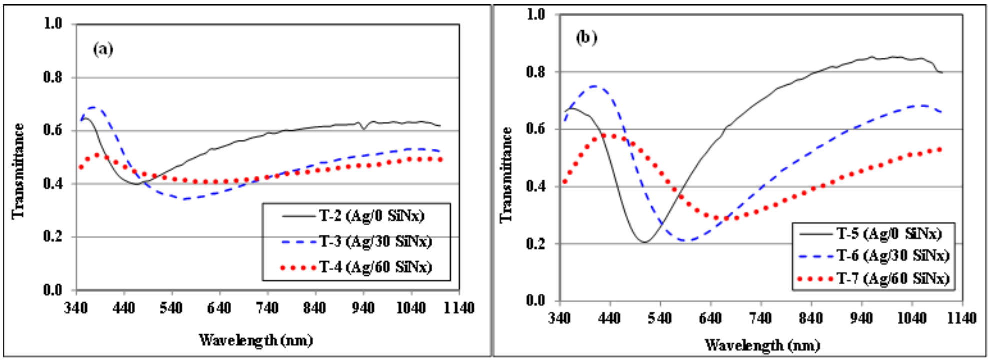

Fig. 8.5 Transmittance versus excitation wavelength for: (a) set-A dewetted at 220 °C and (b) set-B dewetted at 420 °C with SiNx spacer layers of different thicknesses as indicated. No spacer (solid black), 30 nm SiN_x (dashed blue) and 60 nm SiN_x (dotted red)

Figure 8.6 shows the extinction spectra for set A dewetted at 220 °C and set B dewetted at 420 °C with SiN_x spacer layers of 0, 30, and 60 nm in thicknesses deposited on top but before the subsequent deposition of a-Si:H absorber thin film as indicated in table 8.1. As expected, the extinction maxima for sets A and B, are both broadened into the red with increasing the thickness of SiN_x spacer layer. Due to its partial dewetting, the red-shift and broadening of sample 8 extinction spectrum is higher than the reference but less than that of sample 4 with similar 60 nm SiN_x. These broadenings in extinction spectra recommend that more light is either scattered or absorbed by the interfaces in the 600 – 800 nm near infrared excitation spectral range.

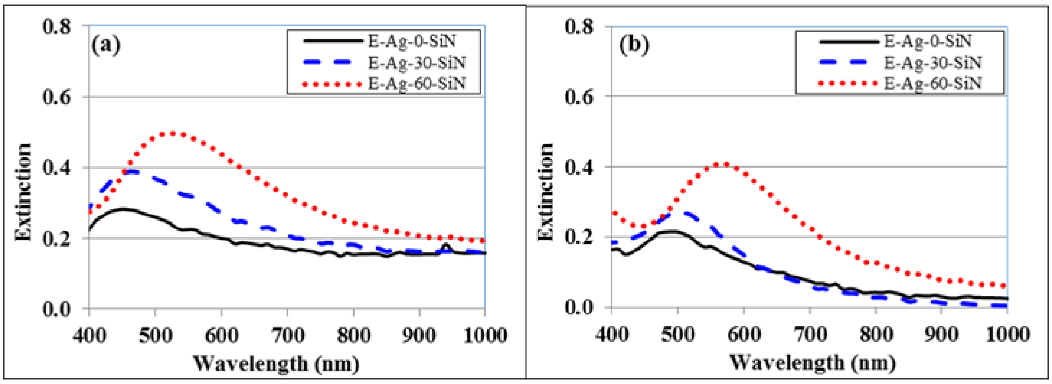

Fig. 8.6 Extinction spectra for the two sets dewetted at (a) 220 °C and (b) 420 °C, with 0 (solid black), 30 nm (dashed blue) and 60 nm (dotted red) SiNx spacer layer thicknesses before subsequent a-Si:H deposition

8.3 Enhanced Optical Extinction and Spectral Photocurrent in a-Si:H

Figure 8.7 shows the extinction spectra of the samples as indicated in both sets A and B and the partially-dewetted sample 8, measured after the final deposition of 150 nm device-quality a-Si:H thin film on top and compared with the extinction spectrum for the reference sample 1 consisting of the same a-Si:H deposited on bare Schott glass. The dependence of extinction spectra on SiN_x spacer layer thickness clearly observed in Figure 8.7 appears to be obscured by the optical contributions of a-Si:H thin film. Indeed, the extinction spectra are not as clean when the a-Si:H layer is deposited because various reflections from the layers and interfaces and the absorption in a-Si:H all contribute to the obtained extinction spectra. Still, it is clear the extinction spectra for the samples in sets A and B are broadened into the red with varying degrees compared with the reference sample. The broadening in the extinction spectrum for sample 8, is less than that of sample 4 with similar 60 nm SiN_x spacer layer thickness yet higher than that of the reference sample.

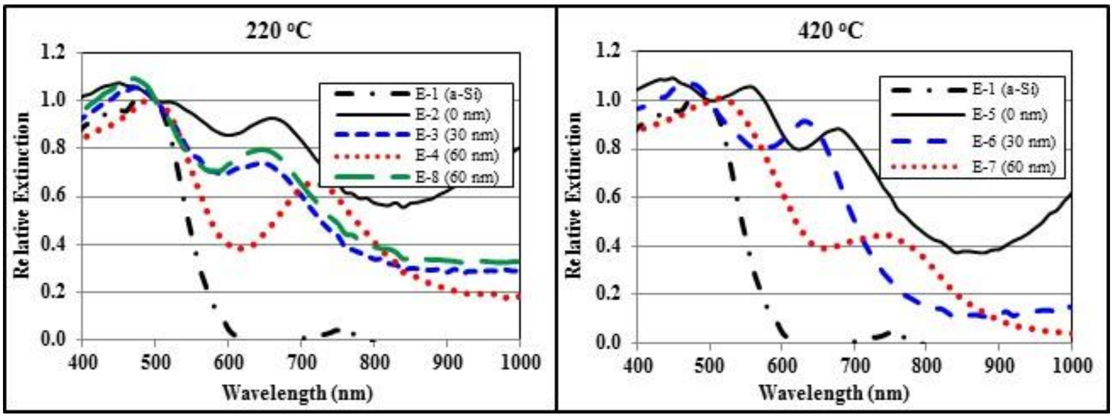

Fig. 8.7 Extinction spectra for samples in the two sets dewetted at (a) 220 °C and (b) 420 °C, measured after subsequent 150 nm a-Si:H deposition on SiN_x with 0 (solid black), 30 nm (dashed blue) and 60 SiN_x (dotted red) SiN_x spacer layer thicknesses. The extinction spectrum of the reference a-Si:H sample deposited on bare Schott glass (dashed-dotted black) is also plotted. The extinction spectrum for sample 8 (long dashed green) is also plotted in Figure 8.7 (a)

To investigate what fraction of the extinct light shown in Figure 8.1 is scattered and coupled into the a-Si:H absorber film, we measure the enhancement of the photocurrent in the a-Si:H absorber versus the wavelength of incident light. Again, before the spectral dependence of photocurrent was measured, we verified that at the extreme biases of – 10 and +10 V, at which the photocurrent is measured, the electrical contacts deposited by thermal evaporation remain ohmic. The measurements were performed by illuminating the a-Si:H side as indicated in Figure 8.1. Spectral photocurrent measurements were performed at 10 V bias versus wavelength for the samples as indicated in table 8.1 at each wavelength in the 400 – 800 nm spectral range with 25 nm intervals.

Figure 8.8 shows the photocurrent calibrated to the power of incident light and normalized to a wavelength of 500 nm as a function of excitation wavelength for the samples in sets dewetted at 220 °C (a) and 420 °C (b) with different SiN_x spacer layer thicknesses along with the reference a-Si:H deposited on bare Schott glass substrate. The chosen wavelength of 500 nm to normalize the photocurrent spectra is because for all wavelengths below 500 nm, most incident light (< 95 %) is absorbed by the 150 nm thick a-Si:H and any plasmonic-induced enhancement is limited to the remaining 5 %. The fluctuations below the 500 nm arise from power calibrations where the source power does decline sharply with decreasing wavelength. It is worth mentioning that the photocurrent is calculated by subtracting the current in the dark form the current under light to eliminate possible contributions to the dark current from the conductive substrates if any. The spectral dependence of photocurrent partially-dewetted sample 8 is also plotted in Figure 8.8 (a). In the wavelength region of 500 – 750 nm, the photocurrent is appreciably higher than the reference for all samples in both sets. For the samples dewetted at 220 °C (Figure 8.8 (a)), the photocurrent for sample 2 with no SiN_x spacer layer is significantly higher than that of the reference, appreciably higher for sample 3 consisting of AgNPs prepared at 220 °C and covered with a 30 nm thick SiN_x spacer layer, and approximately the same as the reference sample for sample 4 consisting of AgNPs prepared at 220 °C and covered with a 60 nm thick SiN_x spacer layer. The photocurrent for the partially-dewetted sample 8, is appreciably higher than the reference and again similar to the spectral photocurrent measured in sample 3. This result fits well with the correlation between the photocurrent and extinction spectra.

For samples in set B (Figure 8.8 (b)), on the other hand, the photocurrent is much lower for sample 5 with no SiN_x spacer layer. The low measured spectral photocurrent of sample 5 is invisible in Figure 8.8. The spectral photocurrent is significantly (~9-fold) higher than the reference sample for sample 6 consisting of AgNPs prepared at 420 °C and covered with 30 nm thick SiN_x spacer layer, and slightly higher than the reference for sample 4 consisting of AgNPs prepared at 420 °C and covered with 60 nm SiN_x spacer layer.

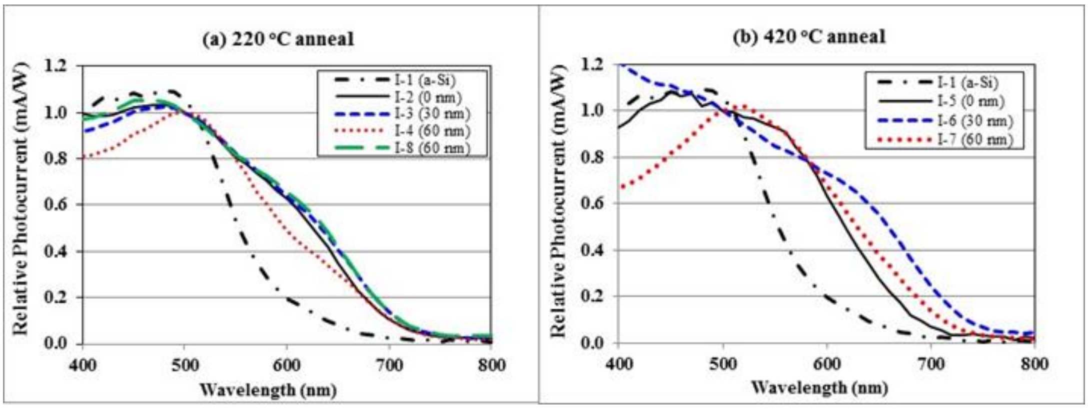

Fig. 8.8 Photocurrent normalized to the excitation power versus wavelength for samples in the two sets dewetted at (a) 220 °C (a) and (b) 420 °C, with 0 (solid black), 30 nm (dashed blue) and 60 nm (dotted red) SiN_x spacer layer thicknesses. The photocurrent for the reference flat a-Si:H deposited on bared Schott is also plotted. The photocurrent for sample 8 (long dashed green) is also plotted in Figure 8.8 (a)

To explore these results further, we conducted a series of numerical simulations on similar structures using RETICOLO software, which utilizes the Rigorously Coupled Wave Analysis (RCWA) written for MatLab by Hugonin and Lalanne [108]. To simplify the simulations, we used one-dimensional square structures of 100 nm in size instead of the 3-dimensional spherical particles. These differences will introduce extra features related to the corners and produce resonances at different frequencies but the trends they predict are in remarkable agreement with experiment. The optical parameters for a-Si:H and SiNx were obtained in-house using Spectroscopy Ellipsometry (ES) measurements, while those for Ag were quoted from MatLab by Johnson and Christy [109]. For glass substrates, we used 1.5 and 0 for the real and imaginary parts of refractive index, respectively.

In Figure 8.9, we show the simulation results for structures with (right) and without (left) plasmonic interfaces integrated to the rear of a-Si:H using SiNx spacer layers. The top rows show cross-sectional views of the structures with a refractive index of 1.0 for air, 4.0 for a-Si:H, 2.0 for SiNx and 1.5 for glass. The middle rows show the localized electric fields where the color scale indicates that the electric field is concentrated near the Ag nanoparticles but clearly skewed into the a-Si:H layer due to its higher refractive index. The bottom rows show the cross-sectional view of absorption by the a-Si:H layer at a wavelength of 865 nm. It is also evident that most of the absorption occurs in the a-Si:H.

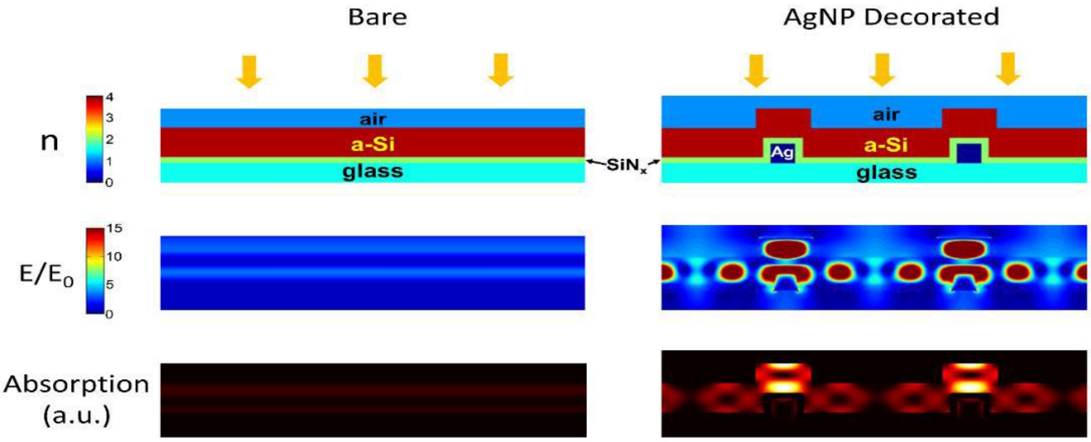

Fig. 8.9 Simulations of the electric field (E) and absorption by a-Si:H for structures without plasmonic interface (left) and with the plasmonic interface (right), both illuminated from the a-Si:H side, showing the schematics (upper rows), enhancement of the localized electric field (middle rows) and absorption (lower rows).

Figure 8.10 shows the simulation results for the extinction spectra (left) and extinction enhancements (right) for the same structures presented in Figure 8.9, with 0, 30 nm, and 60 nm SiNx spacer layer thicknesses compared to flat a-Si:H. The samples with plasmonic interfaces show clear extinction enhancements compared with the reference. The enhancement occurs deeper into the infrared probably due to the differences in the structures of the plasmonic elements but the agreement with the photocurrent enhancement is striking In the sense that the 30 nm spacer yields higher extinction as it does higher photocurrent. Again, the dependence on spacer layer thickness for plasmonic interfaces is obscured by the a-Si:H absorption and interface reflections.

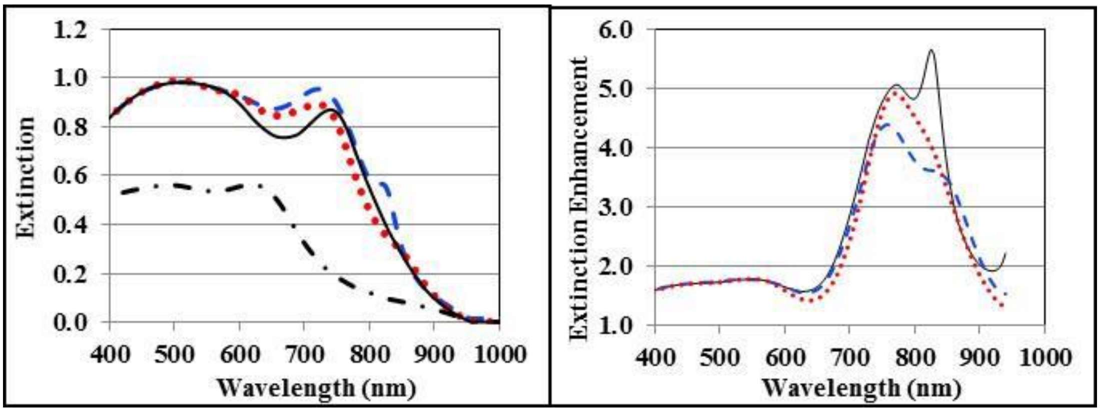

Fig. 8.10 Simulations of extinction spectra (a) and extinction enhancement (b) of flat 150 nm a-Si:H (dashed-dotted black) and plasmonic structure described above integrated to the a-Si:H layer using 0 (solid black), 30 nm (dashed blue), and 60 nm (dotted red) SiNx spacer layer thicknesses

The spectral photocurrent results obtained for sample 2 and sample 5 with no SiNx spacer layers are opposite and appear to oppose the theory. In fact, for the sample 2 with no spacer layers, as indicated in set A, exhibits a pronounced photocurrent. Sample 5 with no spacer layer as indicated in set B, on the other hand, exhibits the smallest photocurrent enhancement even not shown in the considered scale bare of Figure 8.8. This opposite behavior can be illustrated in terms of two competing processes associated with deposition and photocurrents measurements on conductive substrates: 1- When AgNPs are placed in a direct contact with the a-Si:H absorber film, they may induce recombination that reduces the photocurrent and obscure any photocurrent enhancements due to plasmonic interfaces. 2- Photocurrent measurements using coplanar electrodes involve quite different conducting paths for the same a-Si:H thin film deposited on insulating or conducting substrates leading to enormous different results. Figure 8.11 shows a schematic diagram of a typical coplanar contact geometry used for photocurrent measurements. The equivalent circuit for a-Si:H thin film deposited on glass (insulator), see Figure 8.11 (a), and on a conductive substrates, see Figure 8.11 (b).

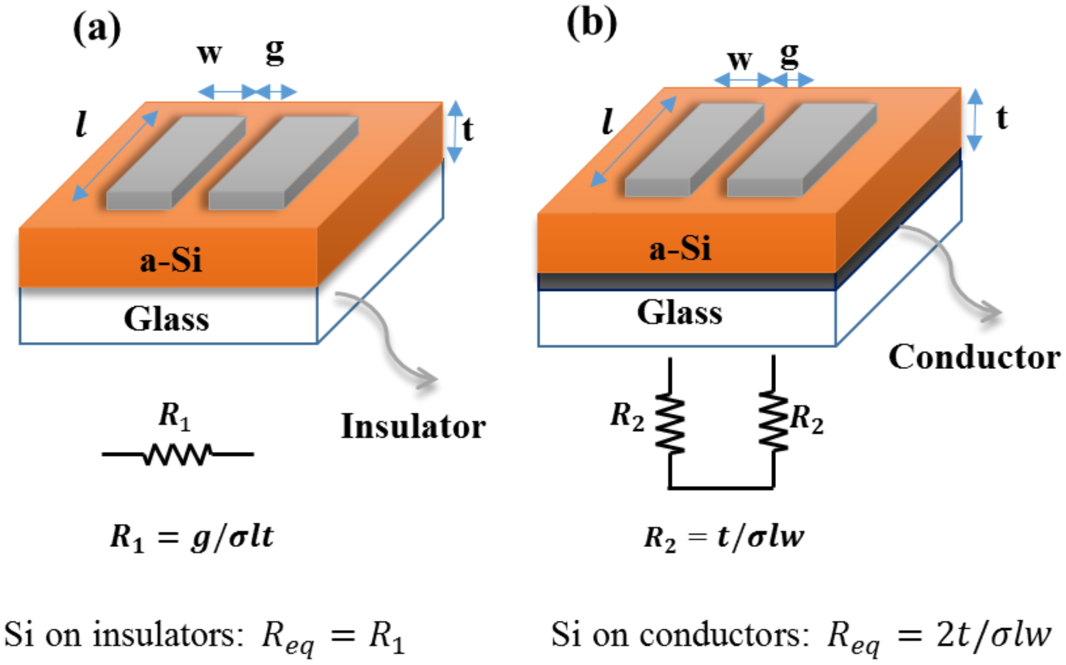

Fig. 8.11 Schematic diagrams of the coplanar geometry of metal contacts on a-Si:H along with its equivalent circuit for a-Si:H deposited on: (a) glass and (b) a conductive surface

Using V = 10 volts as the applied voltage and considering the following quantities:

σ: The conductivity of a-Si:H,

$l = 1\ x 10^{-2}$ m: The length of the coplanar electrodes,

t $= 150\ \times 10^{-9}$ m: a-Si:H thickness,

g $= 0.5\ \times 10^{-3}$ m: The gap separating the two electrodes and,

w $= 2\ \times 10^{-3}$ m: The width of the electrodes.

The photocurrent on a conducting substrate given by $\left(I_{ph}^{c} = V\sigma l w/2t\right)$ can be as high as 10^7 times that of the same film on an insulating substrate $\left(I_{ph}^{i} = V\sigma l t/g\right)$. Yet, this rather large overestimation of the photocurrent is not reflected in the measurements because AgNPs do not constitute a continuous conducting substrate but rather one with conductivity much higher than that obtained for a-Si:H deposited on glass substrate depending on dewetting efficiency.

It is meaningful to attribute to the contradicting results obtained for sample 2 and sample 5 to the nature of insulating and somewhat conductive substrates. The dewetting of Ag thin films leaves some Ag residues on the glass substrate making it slightly conductive and leading to a significant photocurrent enhancement as measured for sample 2. Owing to its lower dewetting temperature at 220 °C, sample 2 is expected to leave more Ag residues making the substrate more conductive and thus larger measured photocurrent (up to 600 times) than that measured in sample 5 prepared by dewetting Ag film at 420 °C. Based on this discussion, it is viable that (i) using no spacer layer makes AgNPs act as recombination centers reducing the photocurrent as the case for sample 5 but (ii) falsely exaggerating the photocurrent as the case for sample 2 with higher Ag residues deeming the results for the no spacer samples meaningless. The low photoconductivity for both samples strongly supports this explanation because the conductive path of Figure 8.11 (b), is shadowed by the electrodes reducing photo-generation of carriers.

Figure 8.12 shows the spectral photocurrent enhancement obtained by dividing the spectral photocurrent of various samples by that of the reference. As can be clearly observed Figure 8.12, a-Si:H deposited on all plasmonic samples, excluding samples 2 and 5, exhibit appreciable enhancements in the 600 – 800 nm spectral range compared to the reference. The largest enhancement is recorded for samples 3 and 6 employing 30 nm thick SiNx spacer layer. The fluctuations present in the data are most likely artificial but the persistent increase in photocurrent in that spectral area for all samples indicates that it is real.

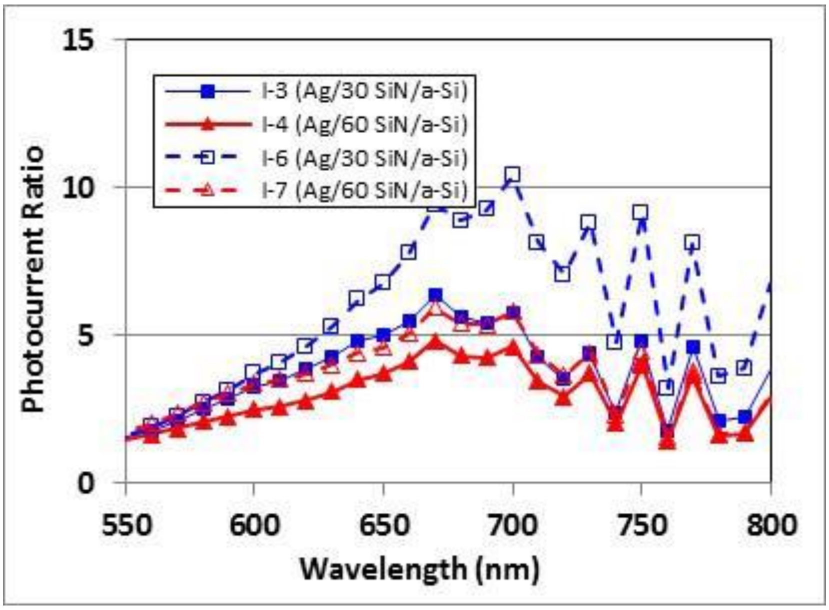

Fig. 8.10 Photocurrent enhancement versus wavelength for samples from set-A (solid symbols) and set-B (open symbols) with 30 nm (squares) and 60 nm (triangles) SiNx spacer layer thicknesses

Excluding samples 2 and 5, the photocurrent results of the remaining samples are surprisingly consistent with the extinction spectra presented in Figure 8.7 and the theoretical calculations given by Catchpole [84]. As we discussed in section 2.2.2.4.4, calculations conducted by Catchpole et al reveals that the maximum absorption by a-Si:H thin film is a compromise between the largest scattering cross section, which increases with increasing spacer layer thickness, and the fraction preferentially scattered into a-Si:H which decreases with increasing spacer layer thickness. It axiomatic that this compromise does not occur at the same spacer layer thickness for different AgNPs sizes.

Indeed, the scattering cross section of AgNPs increases with increasing spacer layer thickness and with increasing nanoparticle size but, according to the calculations by Catchpole et al [84] one expects the compromise for optimum preferential scattering into a-Si:H absorber film to occur at thinner dielectric spacer layer thickness for the larger nanoparticles. For example, sample 3 in set A dewetted at 220 °C and covered by 30 nm thick SiNx spacer layer exhibits a slight photocurrent enhancement, while sample 6 in set B dewetted at 440 °C and covered by the same 30 nm thick SiNx spacer layer shows a 9-fold enhancement. For both sets the enhancements is significantly less for samples employing higher spacer layer thicknesses of 60 nm. Owing to its larger nanoparticle size and less parasitic losses, samples of set B are expected to have a larger enhancement at a given spacer layer thickness in agreement with Equation 2.27.

8.4 Samples Preparation of AgNPs Placed at the Front of a-Si:H Thin Film

To compare the effect of position of AgNPs and thickness of the spacer layer for optimum enhancement in light-trapping using the enhancement in the spectral dependence in photocurrent normalized to incident photon power, we constructed 4 samples with plasmonic interfaces consisting of AgNPs integrated a-Si:H films as indicated in table 8.2. Silver nanoparticles are integrated to the front surface and to both front and back surfaces of a-Si:H thin film. The spectral photocurrent of a-Si:H employing these plasmonic structures are compared to that deposited on the rear of a-Si:H thin film as constructed in sample 6 of set B in table 8.1. Figure 8.11 shows schematic diagram of structures used in this comparison. Interfaces are integrated to a-Si:H using spacer layers of 0, 10 and 30 nm thickness as indicated.

Table 8.2 Plasmonic interfaces consisting of AgNPs integrated at to the front of a-Si:H. Double plasmonic interface in sandwich structure is also indicated

Set	Sample Name	Substrate	1st Ag Dewett	1st SiN_x	a-Si:H	1st SiN_x	2nd Ag Dewett
Set-C	Front-0	Schott Glass	No	No	150 nm	0	220 °C
	Front-10		No	No		10 nm	220 °C
	Front-30		No	No		30 nm	220 °C
Set-D	Double		220 °C	30 nm		10 nm	220 °C

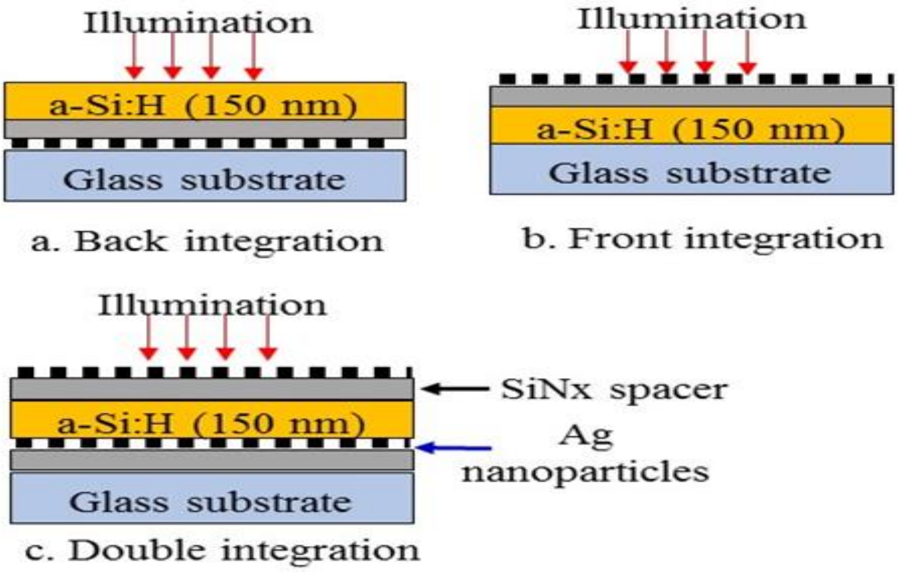

Fig. 8.13 Schematic diagrams for the (a) back (a), (b) front, and (c) double integration configurations of the plasmonic interfaces

Samples Front-0, Front-10, and Front-30 consists of the same a-Si:H films as in table 8.1 followed by SiN_x spacers of 0, 10 and 30 nm, respectively, before the subsequent AgNPs are dewetted on top at 220 °C (front interface). Sample of set D consists of 150 nm thick a-Si:H layer sandwiched between two plasmonic interfaces consisting of AgNPs dewetted at 220 °C with a 30 nm thick SiN_x spacer at the back side and 10 nm SiN_x spacer layer at the front. Formation of AgNPs at 420 °C on top of a-Si:H thin films is not considered because it is not desirable to process a-Si:H thin films at temperatures exceeding their deposition temperature which is typically 220 °C.

8.5 Dewetting of AgNPs on a-Si:H Thin Films

Figure 8.14 shows the SEM images of samples in set C consisting AgNPs dewetted at 220 °C on a-Si:H with SiN_x spacer layer of 0, 10, and 30 nm thickness. The particle size distribution of samples in set C is depicted in Figure 8.15.

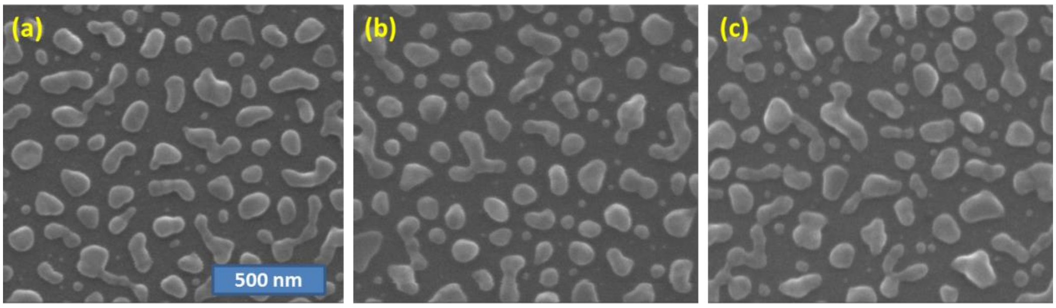

Fig. 8.14 SEM images of AgNPs dewetted at 220 °C on a-Si:H with SiN$_x$ spacer layer of thickness (a) 0, (b) 10 nm, and (c) 30 nm

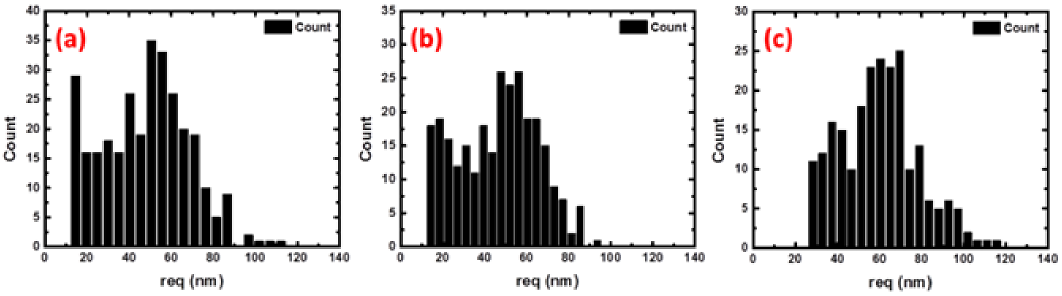

Fig. 8.15 Particle size distributions of AgNPs dewetted at 220 °C on a-Si:H with SiN$_x$ spacer layer of thickness (a) 0, (b) 10 nm, and (c) 30 nm

Particle size distributions of samples in set C are only slightly different. For example, AgNPs fabricated on a-Si:H with 30 nm SiNx spacer layer exhibits the larger number of large nanoparticles and the least number of smaller nanoparticles (see Figure 8.15 (c)) compared to those fabricated on a-Si:H with 0 and 10 nm SiN$_x$ spacer layer. Furthermore, AgNPs fabricated on a-Si:H with 10 nm SiN$_x$ show reduced number smaller nanoparticles as compared to AgNPs fabricated on bare a-Si:H (see Figure 8.15 (a) and (b)). These variations in the number of large and small nanoparticles will affect the position of LSP resonance of AgNPs fabricated on a-Si:H with different SiN$_x$ spacer layer thickness as shown in Figure 8.16. For example, placing a 10 nm SiN$_x$ layer between a-Si:H thin film and AgNPs fabricated at 220 °C (Front-10) results in a blue shift in the LSP from 490 nm for AgNPs formed on bare a-Si (Front-0) to 470 nm for AgNPs formed a-Si:H with 10 nm thick SiN$_x$ spacer layer (Front-19). This blue shift can be attributed to (i) the change in the embedding environment from a-Si:H with high refractive index (~3.8) as indicated in sample Front-0 to SiN_x with low refractive index (~1.8) indicated in sample Front-10, (ii) reduced number of larger particles as seen in Figure 8.15 (a) and (b). Then the LSP resonance shifts to red at 510 nm when the spacer layer thickness is 30 nm due to the increase in the number of larger nanoparticles and the reduction of the number of smaller nanoparticles as shown in Figure 8.15 (c).

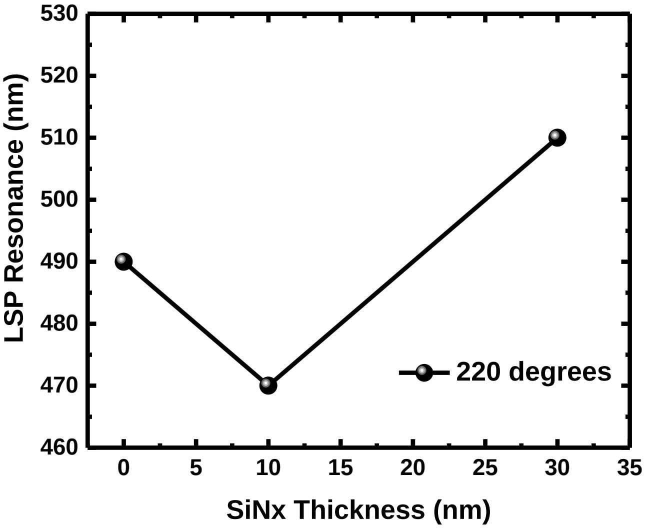

Fig. 8.14 LSP resonance of AgNPs versus SiN_x thickness

Finally, Figure 8.17 shows both planar and cross-sectional SEM images of sample in set D. The lower plasmonic interface appears to roughen the surface of a-Si:H as can be seen in the left part of Figure 8.17. Ag diffusion through a-Si:H is observed due to second dewetting as shown in the right part of Figure 8.17

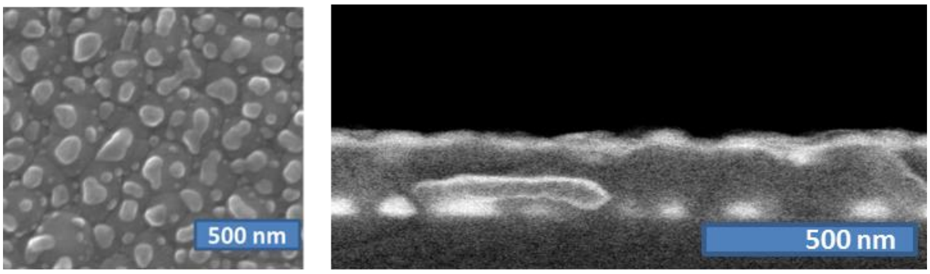

Fig. 8.17 SEM images showing the surface (left) and the cross section Back Scattered Electron (BSE) image (right) of sample in set D

8.6 Perfect AgNPs Position for Enhanced Spectral Photocurrent in a-Si:H Thin Films

Figure 8.18 shows the extinction spectra for samples in set D along with the reference sample consisting of a-Si:H deposited on bare Schott glass (flat sample) as indicated in table 8.1.

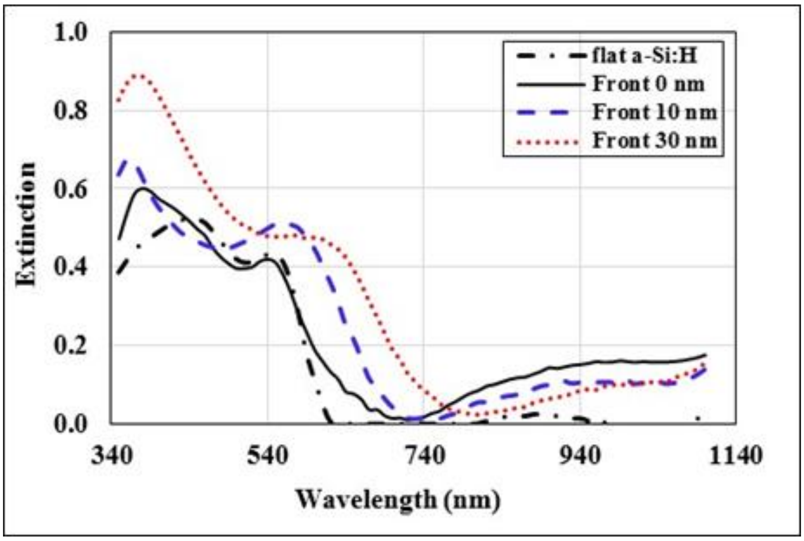

Fig. 8.18 Extinction spectra for flat a-Si:H without plasmonic interface (dashed-dotted line), and with plasmonic interfaces with AgNPs dewetted at 220 °C using 0 nm (solid black), 10 nm (dashed blue) and 30 nm (dotted red) SiN_x integrated to front surface

Extinction spectra of a-Si:H thin film with plasmonic interfaces integrated to the front surface are both broadened and shifted into red compared to the reference sample. The maximum extinction is recorded for a-Si:H thin film separated by 30 nm thick SiN_x spacer layer from the front AgNPs plasmonic layer. This result is consistent with the higher extinction recorded for the same 30 nm thick SiN_x layer separating the a-Si:H thin film from the plasmonic interface integrated at the rear surface (see Figure 8.7).

In Figure 8.19, we compare the extinction spectra for a-Si:H with two plasmonic interfaces consisting of AgNPs dewetted at 220 °C using 10 nm spacer at the front and 30 nm at the back interface (Figure 8.13 (c)) with that of sample 6 with 30 nm SiN_x thick spacer layer integrated to the back (Figure 8.13 (a)) and sample Front-30 with plasmonic interface integrated to the front with 30 nm thick SiN_x spacer layer (Figure 8.13(b)) with the spectra for co-deposited a-Si:H reference with no plasmonic interfaces.

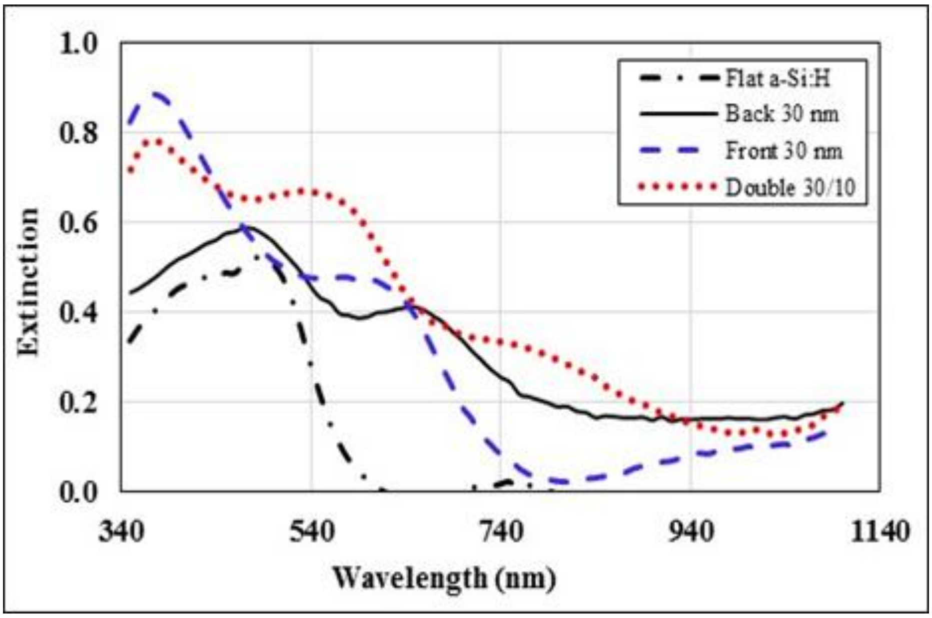

Fig. 8.19 Extinction spectra for flat a-Si:H without plasmonic interface (dashed-dotted line), and with plasmonic interface using Ag nanoparticles dewetted at 220 °C with 30 nm SiN_x integrated to back surface (solid black), front surface (dashed blue), and the double plasmonic interface

The wiggles in the extinction spectra in Figure 8.18 and Figure 8.19 result from the interference between the light reflected off the front and back interfaces of the a-Si:H absorber. Taking a smooth line through these wiggles, we find that all samples exhibit higher extinction in the of 550 – 650 nm wavelength region. Higher extinction implies that more light is scattered or absorbed by the interface. Due to the wiggles in the spectra shown in Figure 8.19, it is not easy to infer a clear trend as to which of these spectra exhibits higher extinction. The previous results obtained on similar interfaces before they are integrated to the a-Si absorber strongly suggest that back interface exhibits higher transmittance and probably higher extinction than the front interface.

Spectral photocurrent measurement of a-Si:H thin film for double plasmonic interface indicated in samples “Double” is not considered samples because Ag diffused from the back integration to the front surfaces during the second annealing to create the second front plasmonic interface as seen in right part of Figure 8.17. Moreover, spectral photocurrent measurement of a-Si:H thin film for plasmonic interface indicated in sample “Front-0” is not considered because plasmonic integration with no spacer layer will exaggerate the measured photocurrent as discussed above.

Figure 8.20 shows the photocurrent enhancement in the a-Si:H absorber versus wavelength over the spectral range of 500 – 800 nm. As in the extinction spectra, all samples with plasmonic interfaces exhibit higher photocurrent compared with the flat a-Si:H reference but the interface integrated to the back of a-Si:H appears to produce the largest enhancement in photocurrent. Again for front integration, the sample Front-30 with 30 nm spacer layer exhibits higher spectral photocurrent enhancement as compared to sample Front-10 with 10 nm spacer layer.

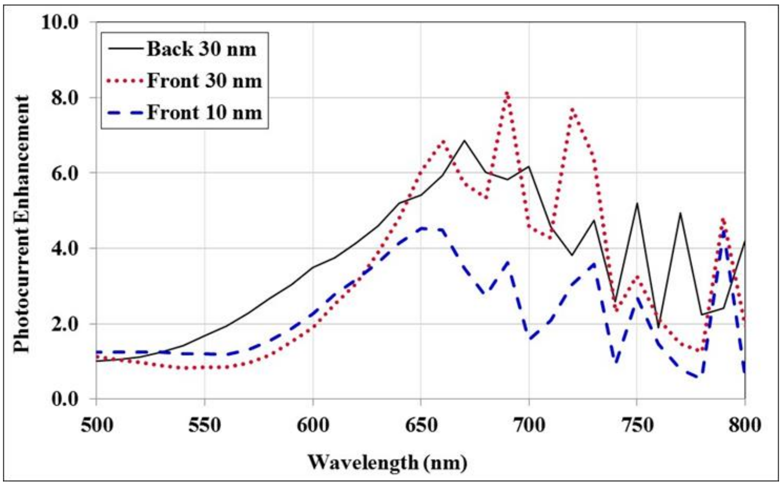

Fig. 8.20 Photocurrent enhancement calibrated to incident light power and normalized to 500 nm wavelength versus wavelength for sample 6 with back plasmonic integration (black), samples with front plasmonic integration Front-10 (blue) and Front-30 (red) with 10 nm and 30 nm SiNx spacer layer thickness, respectively

CHAPTER 9

EFFECT OF SiO_2 SPACER LAYER ON THE LSP RESONANCE OF METAL NANOPARTICLES

Fabrication of MNPs in direct contact with the absorber layer reduces the corresponding photon conversion efficiency of the solar cell due to possible contaminations and carrier recombination induced by the deposited metal islands. Furthermore, it is a prerequisite to passivate surface dangling bonds using dielectric materials such as SiO_2 to attain higher conversion efficiencies. Thus, to integrate MNPs in the fabrication of c-Si solar cells, it is important to fabricate them on a dielectric spacer layer either on the front or back surface of the solar cell. The use of a spacer layer between the absorbing layer of the cell and the nanoparticles is of great interest both from the fabrication and the photon management points of view as discussed in the previous chapters. In this chapter, we investigate the influence of SiO_2 spacer layer thickness on the average AgNPs size and shape, size distribution, and thus on the excitation of localized surface plasmon properties as the optical response of metal nanoparticle can be tuned by varying their size or shape, size distribution, or by modifying the local dielectric environment. The thickness of the dielectric spacer plays an important role in the plasmonic coupling of the incoming photon field into the underlying active device.

9.1 Samples Preparation

Pyrogenic steam oxidation was used to obtain Si wafer of different SiO_2 thicknesses. Silver nanoparticles were prepared by evaporating 15 nm thin film on the Si wafer followed by thermal dewetting of the underlying substrate. The Ag thin films were dewetted at 200 °C for 1 hour in nitrogen flow. Dewetting using temperatures higher than 200 °C degrades the performance of c-Si solar cell [92]. The plasmonic resonance peaks were measured by reflection spectroscopy. The SEM images of the substrates were used to obtain statistical distribution of the particle size.

Silver thin film dewetted of 15 nm in thickness was dewetted on eight different SiO_2 thicknesses as indicated in table 9.1.

Table 9.1 Samples construction: crystalline silicon wafers with 8 different SiO_2 thicknesses

Oxide Thickness (nm)	NO	6.37	9.79	14.9	18.1	49.2	69.9	105.3
Ag thin film	15 nm							
Dewetting temperature	200 °C							

Spectroscopic ellipsometry measurement technique was used to measure different SiO_2 thin films thicknesses. Ag thin film was deposited by the thermal evaporation technique. The thickness of native oxide (NO) was measured to be 1.1 nm.

9.2 SEM images and AgNPs size Distribution

Figure 9.1 shows the SEM images of the dewetted samples used in this study as indicated in table 9.1. AgNPs formed on SiO_2 layers of different thicknesses appears to have spherical shape with different size.

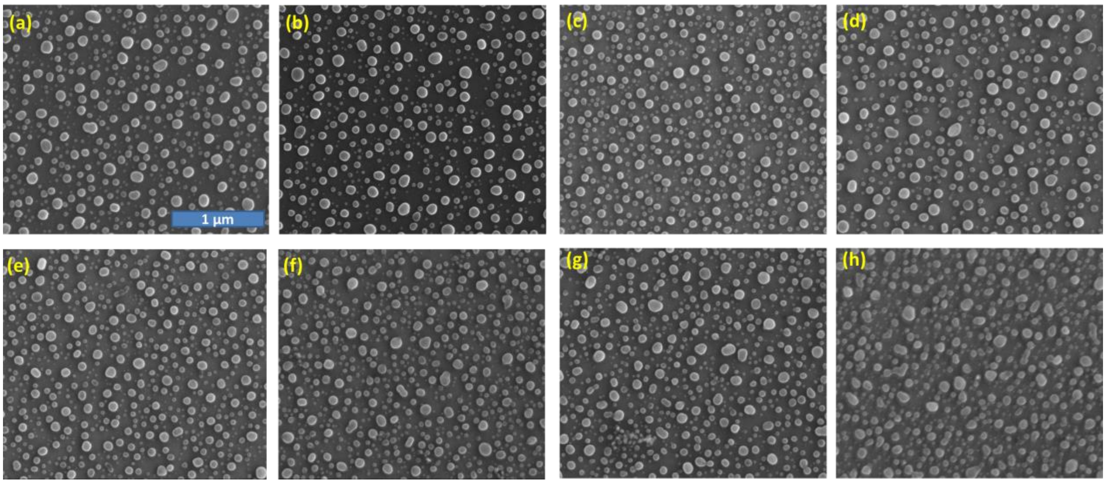

Fig. 9.1 SEM images of AgNPs fabricated on (a) native oxide and on differed SiO2 thicknesses of (b) 6.37 nm, (c) 9.79 nm, (d) 14.9 nm, (e) 18.1 nm, (f) 49.2 nm, (g) 69.9 nm, and (h) 105.3 nm

Figure 9.2 shows the average particle size obtained by analyzing the SEM images using Gwyddion image analysis program. As the substrate is prepared by thermal growth method, we do not expect the surface roughness to be different in different oxide thicknesses. So the driving force behind the AgNP size can be the change of other physical properties or also possibly change of chemical properties. This is in a way similar to surface modification for changing hydrophobicity of the surfaces. If the thermal conductivity alone was the key player in the control of average AgNP size, then we would expect it to change smoothly from the bare Si value to SiO_2 value by continuous increase of SiO_2 thickness. As this is not the case we suspect the changes also to be of chemical origin.

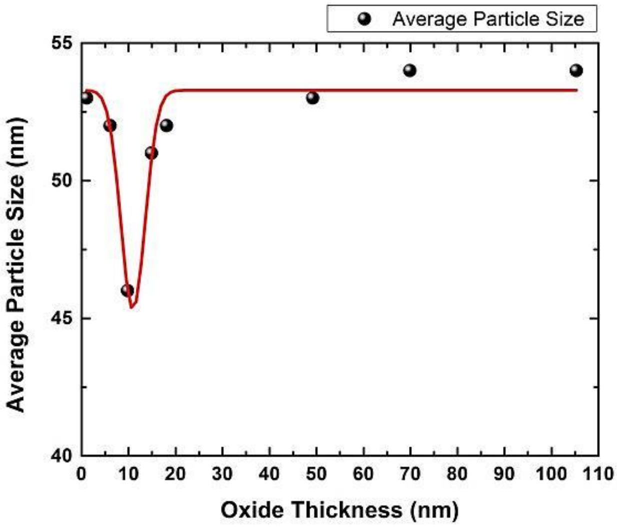

Fig. 9.2 Average AgNPs size versus oxide thickness. Red plot is a Gaussian fit of average particles size

9.3 Effect of SiO_2 thickness on AgNPs Optical Response

Figure 9.3 presents the total reflection of bare SiO_2 films and that of AgNPs fabricated on different SiO_2 spacer layer. The total refection is just identical for all SiO_2 with thickness below 18.1 (see Figure 9.3 (a)). When the oxide thickness increases, the total reflection is reduced as expected and is attributed to the anti-reflection property of SiO_2. The lowest reflection is measured from 105 nm thick SiO_2 film as shown in Figure 9.3 (a), brown curve. When AgNPs are formed on these oxides, the total reflection shows a random behavior where the lowest reflection is now recorded for AgNPs fabricated on 49.2 nm SiO_2 film (see Figure 9.3 (b), olive curve) while for AgNPs formed on the 105.3 nm SiO_2 film we observe a pronounce total reflection (see Figure 9.3 (b), brown curve). These variations in total reflection of AgNPs of SiO_2 reveal the fraction of light scattered into the Si substrate to that reflected off which is highly dependent on the oxide thickness. The lowest reflection of AgNPs formed on 49.2 nm thick SiO_2 film suggests that a larger fraction of incident light couples into Si absorber rather than reflected.

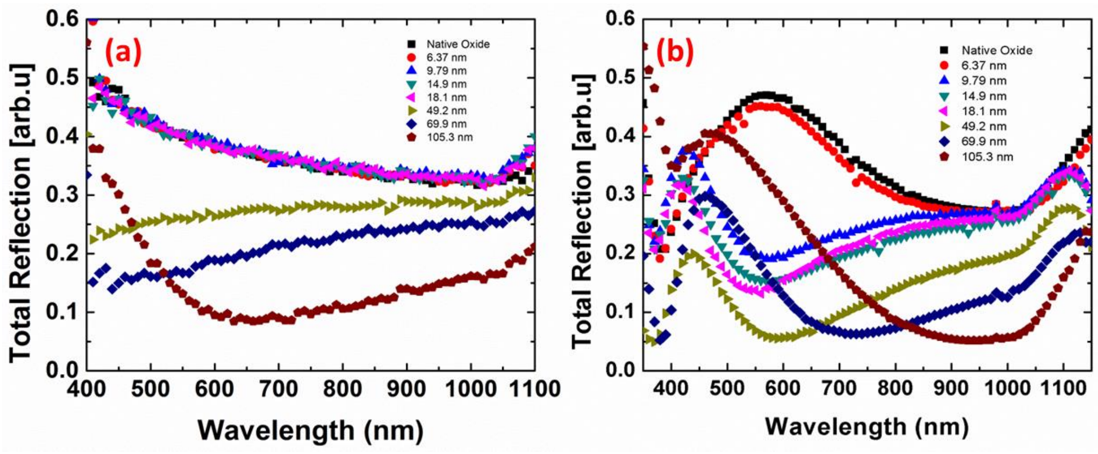

Fig. 9.3 Total reflection of (a) bare SiO_2 of different thicknesses and (b) AgNPs fabricated on SiO_2

Figure 9.4 shows the dependence of LSP resonace of AgNPs on the thickness of SiO_2 dielectric spacer layer. The LSP resonance of AgNPs depicts itself in the form of a maximum in the total reflection curves. We can see that the AgNPs resonate at 570 nm for native oxide because the AgNPs to Si separation is small and higher refractive index medium like Si tends to red shift the resonance due to depolarization effects. As the oxide thickness increases from 1.1 nm to 18.1 nm, the LSP resonance wavelength blue shifts from 570 nm 410 nm. This blue shift is due to the change in the polarizability of the particles arising from the change in AgNPs embedding environment from Si with higher refractive index (n~3.8) when the spacer layer thickness is 1.1 nm to SiO_2 with lower refractive index (n~1.5) when the spacer layer thickness is 18.1 nm. Increasing the oxide thickness to values larger than 18.1 nm red shifts the LSP resonance and the resonance becomes constant for thicknesses larger than 69.9 nm where the anti-reflection property of SiO_2 becomes more pronounced (photonic effect). LSP resonance values of AgNPs at each SiO_2 spacer layer thickness are listed in table 9.2.

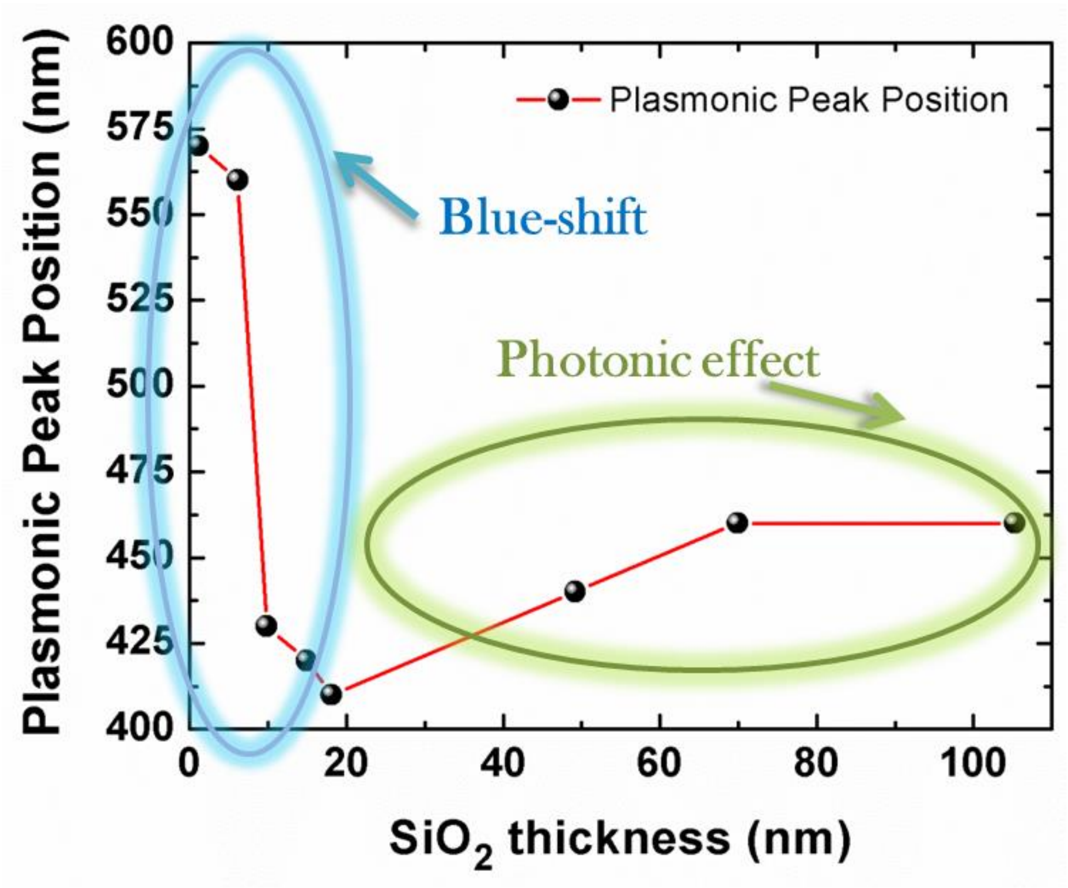

Fig. 9.4 Dependence of LSP resonance on SiO_2 thickness

Table 9.2 LSP of AgNPs at each SiO_2 spacer layer thickness

SiO_2 thickness (nm)	LSP resonance (nm)
1.1 Native Oxide	570
6.37	560
9.79	430
14.9	420
18.1	410
49.2	440
69.9	460
105.3	460

CHAPTER 10

SUMMARY AND DISCUSSIONS

This work has been motivated by the desire to combine plasmonics with thin-film silicon solar cell technology in order to address new light trapping concepts. We have made use of the optical properties of AgNPs embedded in conductive oxide and dielectric spacer layer and AgNPs in combination with textured Al:ZnO to improve the light absorption in a-Si:H thin film as representative case for enhanced light trapping in thin film solar cells. Plasmonic AgNPs were fabricated by the simple dewetting technique. In this technique, AgNP are formed by thermal annealing a continuous thin metal film sputtered or evaporated on a given substrate. Two main advantages of this technique are: i) it is possible to fabricate MNPs on larger scale substrates which is useful for mass production of solar cells; ii) it is possible to control the average particle size and the size distribution by dewetting technique because they strongly depend on the thickness of metal thin film as well as on the annealing temperature. Most studies exploit external quantum efficiency (EQE) in photo-detectors or solar cells to measure enhancement in photocurrent due to the plasmonic interfaces. To minimize complications and sources of errors in device processing, we employ the enhancement in the spectral dependence of photocurrent driven by a constant bias in a standard device-quality a-Si:H layer as an indicator for an effective plasmonic effect.

The first concept investigated in this thesis is based on the fabrication of plasmonically active interfaces consisting of AgNPs embedded in Al:ZnO. This interface has the potential to be used at the front surface and at the back reflector of a thin film solar cell to enhance light trapping and increase the photo-conversion efficiency. Ag can readily dewet on the Al:ZnO surface when annealed at temperatures significantly lower than the melting temperature of Ag, which is beneficial for lowering the thermal budget and cost in solar cell fabrication. Such interfaces fabricated by the simple dewetting technique resulted in plasmonic resonance in the visible and near infrared regions of the solar spectrum, which is important in enhancing the conversion efficiency of thin film solar cells.

Silver nanoparticles of controllable shape and size embedded in Al:ZnO layer in a composite-like structure were fabricated on top of Al:ZnO layers to correlate nanoparticle shape, size and size distribution with the resulting plasmonic peaks. It was found that the starting Ag film thickness, the dewetting temperature and the medium in which nanoparticles are formed, are important parameters in controlling the size and shape of the nanoparticles. Nanoparticles following a random distribution with a mean particle diamter of 50 – 60 nm are obtained by annealing a sputtered 15 nm Ag layer at temperatures of about 200 °C. Larger particles of ~ 120 nm in diameter were obtained by increasing the annealing temperature to 300 °C. We also find that the total encapsulation of Ag film in Al:ZnO inhibits dewetting as was demonstrated in sample set C consisting of sputtered 15 nm Ag thin film sandwiched between two Al:ZnO thin films as indicated in table 5.1, for anneals below 300 °C. Increasing the annealing temperature to over 400 °C appears to produce larger particles outside the Al:ZnO as was shown in Figure 5.4, but not through a conventional dewetting process. The progressive increase in the size of particles that appear to be emerging from the Al:ZnO at 400 °C and 500 °C (Figure 5.4), suggests that the thin Ag is flowing through the top Al:ZnO layer by bulk diffusion. Even though the melting temperature of pure bulk silver is close to 900 °C, it is known that this temperature is drastically reduced at the nanoscale [110]. Furthermore, the process may also involve vertical bulk diffusion of silver through the top Al:ZnO layer followed by lateral surface diffusion leading to the more spherical nanoparticles with narrower size distribution. Surface diffusion leads the emerging particles to reach a more uniform size distribution at these elevated annealing temperatures. The more uniform particle size and more spherical shapes are consistent with the results of the high temperature anneals of 15 nm Ag film sputtered on glass coated Al:ZnO (sample set A presented in table 5.1). To produce nanoparticles embedded in the Al:ZnO, dewetting and particle formation should be performed by annealing before adding the capping Al:ZnO layer. This can be performed with or without exposure to atmosphere depending on the annealing temperature. An alternative method to produce nanoparticles embedded in the Al:ZnO without exposure to atmospheric agents is to sputter the Ag film at higher than room temperature. Our results show that sputtering Ag at 150 °C appears to initiate the dewetting process and allows for the fabrication of encapsulated AgNPs without exposure to atmosphere upon subsequent annealing. The particle sizes obtained at 200 °C and 300 °C anneals produce plasmonic peaks in the visible or near infrared regions of the solar spectrum with expected strong light trapping effects that can be integrated to improve the efficiency of thin-film solar cells. Increasing the annealing temperature to over 400 °C results in the formation of large and pure Ag nanoparticles exceeding 1 µm in diameter and have no detectable peaks in the visible or near infrared regions.

In the second concept, we investigated the effect of single and double plasmonic interfaces using self-assembled AgNPs placed at the interfaces of two different media with various dielectric constants and integrated at the rear of device-quality a-Si:H films to measure improved light-trapping using photocurrent enhancement as an indicator. We conducted an intensive study on the fabrication of single- and double-layered plasmonic interfaces consisting of AgNPs fabricated by the dewetting technique and placed at the interfaces between two media with different thicknesses and refractive indices. The SEM images obtained at various processing stages show successful construction of both single and double layered interfaces. The mean particle size, estimated by the equivalent disk radius analysis, did not change significantly with temperature but that lower annealing temperatures produce more particles with a mean diameter less than 50 nm. In spite of this weak dependence on temperature, significant shifts are observed in their plasmonic resonance frequency as illustrated in Figure 6.6. The single-layer interfaces exhibit one minimum in the transmittance spectrum but significant broadening of the extinction peak into the red. The extinction spectra of the double interfaces appear to consist of two overlapping maxima that may correspond to an interaction between the two constituent nanoparticle layers. The extinction maxima of the a-Si:H films deposited on these interfaces show a clear broadening into the red compared with a-Si:H on glass. This broadening indicates significant increase in scattering and/or absorption by the interface depending on the size of the nanoparticles in the interface. This enhanced extinction by the interface could lead to enhanced photocurrent if scattering dominates the extinction or reduce the photocurrent if absorption dominates. Since the extinction maxima for these interfaces show significant broadening into the red, the enhancement of photocurrent caused by these interfaces may be related to the plasmonic resonance effect and suggests that scattering is significant in the range of 600 – 700 nm. The previous results of Ag and Au plasmonic interfaces integrated to photodetectors and solar cells claim large photocurrent enhancements in different parts of the solar spectrum [50,52]. The different results obtained by these authors may be related to the various differences used in the device structures. These differences include material, size and shape of the nanoparticles, spacer layer material and thickness and other factors related to the device structure itself. The overall enhancement across the entire solar spectrum is difficult to understand while differences in frequency over which the enhancements take place may be explained in terms of these differences in materials and design. Our photocurrent enhancement in the spectral range of 600 – 700 nm is consistent with these results and suggests that the photocurrent enhancement may be controlled more accurately by tuning materials thicknesses and dielectric constants used in the interface. Our particle size for both single and double interfaces show significant portion of particles with sizes less than 50 nm in diameter suggesting that absorption still dominates extinction in these interfaces. We propose that our results may be explained by the far-field effect involving valence band tail (VBT) states. The broadening of the extinction peak into the 600 – 700 nm caused by the plasmonic interface, indicates that further extinction including preferential scattering into the a-Si:H side at these wavelengths is taking place. Preferential scattering enhances absorption by these VBT states relative to the a-Si:H on glass and a corresponding relative enhancement of photocurrent takes place in that spectral region.

The significant reduction in photocurrent across the visible region is not well understood but has previously been attributed to parasitic losses by the plasmonic interface. However, quick calculations suggest that these losses do not account for that significant reduction if only the far field effect is considered. From the transmittance spectra (Figure 6.5), we observe that approximately 30 – 40 % of the visible incident light is transmitted through the 250 nm amorphous silicon film. The rear a-Si:H / glass interface would at most reflect 16 % of that light, which is the maximum enhancement one would expect assuming “clean” a-Si:H/glass interface with no plasmonic effects. Assuming that the plasmonic interface placed at the rear absorbs all that light and does not allow for any reflection through parasitic losses, the result should not decrease by more than 16 % of the 30 – 40 % transmitted light. Based on this, it is difficult to explain the reduction in terms of parasitic losses and the far field effect alone. To explain this reduction, one should consider the near field effect. We recall that the nanoparticles actual size for most interfaces is less than 100 nm which in itself is a major contributing factor for increasing absorption and reducing scattering because the relative ratio of absorption to scattering increases with decreasing actual particle size [111]. Furthermore, the effective absorption and scattering cross-sections are significantly higher than the actual sizes and may extend deep into, and in fact dominates the, a-Si:H absorber layer increasing absorption of carriers in that region. To eliminate this possibility, the plasmonic interface should be placed farther away from the absorber layer. Catchpole and Polman calculate the scattering cross section as a function of nanoparticles' distance from the substrate and find that at 20 nm the scattering cross section is only about 10 % of its value at infinity while the absorption cross-section is significantly higher [81]. Since our spacer layer happens to be about 20 nm, it is not surprising that most of the light is absorbed by the interface and little enhancement in photocurrent is observed. These authors find that the scattering cross-section is maximal at about 60 nm from the interface [84].

In the third concept, we investigated the possible improved scattering potential of a combined scattering interface consisting of AgNPs fabricated on textured Al:ZnO. This interface is placed on the front of a-Si:H thin film in a typical superstrate configuration. In this interface we merge the scattering effects of Al:ZnO surface texturing and AgNPs plasmonics in a single light-trapping interface to investigate their combined light-trapping efficiency on a-Si:H thin film in terms of enhanced spectral photocurrent. We showed that outstandingly high transmittance haze is achieved from single step HCl surface textured Al:ZnO and demonstrate Ag dewetting on textured and flat Al:ZnO surfaces upon annealing at moderate temperatures. Optical response of these plasmonic interfaces clearly display plasmonic resonances in the visible and near infrared, which is crucial for enhancement of photovoltaic conversion efficiency in thin film solar cells. We have experimentally demonstrated that high diffuse transmittance; as well as high transmittance haze, of textured Al:ZnO can be achieved, without reducing the total transmittance, by a single step chemical texturing using HCl only. High diffuse transmittance can be achieved using a combination of HCl and HF. However, using HF assisted etching of glass coated Al:ZnO will affect the surface of glass itself and the resultant high diffuse transmittance is coming from the contributions of textured Al:ZnO as well as textured glass. The advantage of using HCl; but not HF, lies in the fact that the obtained high diffuse transmittance is associated with surface textured Al:ZnO only. Textured Al:ZnO has an average surface roughness of 157 nm which corresponds to the desired thin absorber layer thickness of the SC. We attribute this drastic increase in diffuse transmittance (haze) over the entire spectral range to the vast increase of average surface roughness of textured Al:ZnO.

The AgNPs were again prepared by the simple dewetting technique. Dewetting of AgNP on flat Al:ZnO at 200 °C forms rather interconnected smaller AgNPs where Al:ZnO is sputtered at high temperature resulting in strong surface adherence with consecutive Ag thin film. Increasing the annealing temperature to 300 °C is enough to break the strong adhesion between flat Al:ZnO and Ag thin film leading to a complete coalescence of larger AgNP atop the flat Al:ZnO surface. Still, increasing the annealing temperature to 400 °C or 500 °C do result in larger spherical AgNP; $\geq$ 500 nm in diameter, which does not support LSP upon light excitation. Dewetting of AgNPs on textured Al:ZnO at 200 °C and 300 °C results in well-shaped AgNPs distributed in conformal manner within the Al:ZnO craters as shown clearly in Figure 7.6 (c) and Figure 7.7 (c); respectively. In this case, the Al:ZnO surface is treated with HCl so the consecutive Ag thin film does not adhere to textured Al:ZnO surface. LSP of AgNPs are detected from total transmittance measurements and not from total reflection since the measurements were obtained by illuminating the glass side so the maximum scattering at AgNPs resonance wavelength couples into higher refractive index material; the Al:ZnO. AgNPs resonate closer to the red portion of the solar spectrum which is crucial to enhance the photon path length in this spectral region where the photons are weakly absorbed. The total and diffuse transmittance of AgNPs on flat and textured Al:ZnO are lower than that of bare flat and textured Al:ZnO because most of the light scattered by AgNPs is coupled into optically dense (n~2) and geometrically thick (1.25 μm and 0.81 μm for flat and textured, respectively) Al:ZnO. Thus once those Al:ZnO/AgNPs interfaces are integrated into thin film SCs such as those made of hydrogenated amorphous silicon (n~4), a significant fraction of light scattered by AgNPs is expected to preferentially couple into the absorber layer where the density of optical modes are double that of Al:ZnO.

Transmittance haze of textured Al:ZnO and that of AgNPs on textured Al:ZnO are the comparable because the haze is in the order of unity and whatever the extinction is, the ratio of diffuse transmittance to total transmittance is not affected significanlly where the reduction in total and diffuse transmttance due to extinction by AgNPs is two-fold: scattering based coupling into Al:ZnO and parasitic absorption by AgNPs. It is important to obtain the optical response of the textured and plasmonic interface by cloning the same geometry of such an interface in the desired solar cell application. The application can be performed in two ways: in the case the interface is to be placed on the front surface, then it should be illuminated from glass side; and in the case the interface is to be placed on the back surface, then it is better to shine the light directly to the interface. This is because the optical response is highly sensitive to the surrounding refractive index and hence the density of optical modes as it can be seen in reflection measurements.

Light scattered by textured Al:ZnO and AgNPs decorated and textured interface is optimized by placing a thin SiO_2 spacer layer between the interface and the a-Si:H absorber. Our results indicate that the AgNPs placed at the interface between Al:ZnO and SiO_2 significantly enhance absorption at energies close to the band gap of a-Si:H. Surface texturing by wet etching of ZnO:Al combined with AgNP produces the highest optical extinction of a-Si:H thin films at the band edge. Furthermore, the measured photocurrent in a-Si:H showed a clear increase not only at AgNPs resonance wavelength but over the entire wavelength range. This dramatic enhancement in photocurrent response of a-Si:H on textured Al:ZnO with AgNPs in a single light tapping interface is due to enhanced forward scattering of light into a-Si:H. The textured Al:ZnO surface scatters light obliquely providing another chance for coupling light to a-Si:H. But AgNPs do randomize the incident light in various angles instead of just scattering obliquely in one direction. The plasmonic concentration of light induced by AgNPs near textured AZO increases the scattering into the solar cell and thus the absorption enhancement.

Finally, we studied the influence of SiN_x dielectric spacer layer thickness and the position of AgNPs integrated to a-Si:H thin film on the AgNPs scattering efficiency into a-Si:H as well as on the a-Si:H absorption. The selection of optimum spacer layer thickness and the optimum position of AgNPs were investigated by examining the enhancement in photocurrent in the a-Si:H absorber layer of various thicknesses and at all three possible integration positions of front, back, and both. For this purpose, we successfully constructed plasmonic interfaces by the self-assembled technique of dewetting a 15 nm silver film on glass at 220 °C and 420 °C to produce two sets of different AgNPs sizes and different SiN_x spacer layer thicknesses to study their effects on optical absorption and enhancement of photocurrent. In consistence with the results obtained in chapter 6, the LSP resonance red-shifts appreciably by increasing the dewetting temperature from 220 °C to 420 °C, which increases the particle sizes, and the red-shift as well as the width of the resonance increase with increasing spacer layer thickness. Photocurrent enhancements caused by these interfaces exhibit critical dependence on the spacer layer thickness showing a 9-fold enhancement at a spacer layer thickness of 30 nm for sample 6 of set B as indicated in table 8.1. Since the photocurrent enhancement continues to increase as the thickness of the dielectric spacer layer decreases, we suppose that the compromise for optimum preferential scattering into a-Si:H absorber film to take place at a spacer layer thickness of even lower than 30 nm. However, as discussed in chapter 6, dielectric materials of thicknesses lower than 20 nm may become discontinuous and introduces the complications of a-Si:H exposure to the Ag. Our results do not determine an optimum spacer thickness, but place an upper limit of 30 nm for maximum enhancement and a lower limit of approximately 100 nm on the nanoparticle diameter used in the interface. Again, this large enhancement and its continuing increase with decreasing spacer layer thickness may not be explained in terms of the far-field effect alone. The large electric fields localized near the simulated plasmonic structures and extending into the a-Si layer strongly suggest that the near-field effect may be responsible at small spacer layer thickness [108].

By comparing both optical extinction and photocurrent results obtained for a-Si:H with plasmonic interfaces integrated to the rear or to those at the front surface with the same 30 nm thick SiN_x spacer layer, we conclude that the proper position for the plasmonic interface is the back of the absorber. The good enhancement for the double plasmonic interface integration scheme is probably due to the back surface.

Parallel to the studies related to the integration of various plasmonic and scattering structures in a-Si:H thin films, we studied the influence of SiO_2 dielectric spacer layer on the excitation of LSP of AgNPs fabricated on the front of c-Si wafer with different SiO_2 spacer layer thickness. Dangling bonds passivation obtained by SiO_2 or SiN_x is a prerequisite to achieve high conversion efficiencies in c-Si solar cells. This study aims to build an understanding of what thickness of SiO_2 spacer layer is desirable to integrate AgNPs in c-Si solar cell fabrication. When AgNPs are formed on different oxide thicknesses, the total reflection exhibits a random behavior where the lowest total reflectance is recorded for AgNPs fabricated on 49.2 nm SiO_2 film while for AgNPs formed on the 105.3 nm SiO_2 film exhibit a pronounce total reflection. These variations in total reflection of AgNPs of SiO_2 reveal that the fraction of light scattered into the Si substrate to that reflected off which is highly dependent on the oxide thickness. The lowest reflection of AgNPs formed on 49.2 nm thick SiO_2 film suggests that a larger fraction of incident light couples into Si absorber rather than reflected.

We found that LSP resonance of AgNPs is highly dependent on the spacer layer thickness. For example, AgNPs resonate at 570 nm for native oxide because the AgNPs to Si separation is small and higher refractive index medium like Si tends to red shift the resonance due to depolarization effects. As the oxide thickness increases up to 18.1 nm, the LSP resonance wavelength shift to blue due to change in the embedding medium from high refractive index Si to lower refractive index SiO_2. AgNPs formed on oxide thicknesses larger than 18.1 nm shift into red where the anti-reflection property of SiO_2 becomes more pronounced.

CHAPTER 11

CONCLUSIONS

Several single and double silver nanoparticles (AgNPs) light management architectures were constructed and integrated to device quality a-Si:H thin films to study their light trapping capacities in terms of enhancement in spectral photocurrent in a-Si:H thin films. AgNPs were fabricated by the simple dewetting technique which is compatible with large scale area fabrication of silicon solar cell.

In the first concept, I fabricated various plasmonic interfaces consisting of AgNPs embedded in Al:ZnO. Such interfaces have the potential to be integrated to the front and at the rear of thin film silicon solar cell. In this study, AgNPs of well-controlled size and shape were successfully fabricated ontop of glass coated Al:ZnO. It has been found that increasing the dewetting temperature from 200 °C to 300 °C results in an increase in the average particle size that leads to a red shift in the LSP resonance of the fabricated AgNPs. Annealing above 400 °C produces large AgNPs with diameters exceeding 1 µm which does not support the LSP behavior of metal nanoparticles. I have also found that, it is not possible to produce active plasmonic interface sandwiched between two Al:ZnO thin films i.e., embedded within Al:ZnO and encapsulated by Al:ZnO, when the starting Ag thin film is deposited on top of the bottom Al:ZnO at room deposition temperature. In such structure, Ag diffusion through the top Al:ZnO was observed when the dewetting temperature was increased to more than 400 °C. A convenient route to produce active plasmonic interface of AgNPs sandwiched between two Al:ZnO thin films without exposing the interface to atmospheric agents is to deposit the Ag thin film at 150 °C substrate temperature. All the plasmonic interfaces produced in this study produce plasmonic peaks in the visible and near infrared portions of the solar spectrum which is important because Si thin film solar cells have reduced light absorption in these regions.

In the second concept, I investigated the influence of single and double AgNPs plasmonic interfaces placed at the interfaces of two different media having different dielectric constants and integrated to the rear of a-Si:H thin films to measure enhanced light trapping using spectral photocurrent enhancement in a-Si:H as as indicator. In this study, single-plasmonic interfaes of AgNPs were fabricated on glass substrates by dewetting of Ag thin film at 200 °C and 400 °C. The average particle size did not change significantly with increasing dewetting temperature but 200 °C annealing temperature produces more particles with sizes of less than 50 nm. In spite of this minor difference in average particle size, significant shifts to red are observed in their LSP resonance. I have shown that single-plasmonic interfaces exhibit single minimum in the total transmittance spectrum but significant broadening of extinction peak into red. On the other hand, double-plasmonic interfaces exhibit extinction spectra consisting of two overlapping maxima that may correspond to an interaction between each of the two AgNPs plasmonic layers. The maxima of the extinction spectra of a-Si:H thin films deposited on these single- and double- plasmonic ineterfaces show a clear broadening into the red compared with that of a-Si:H on bare glass substrate. Such broadening suggests that there is a significant increase in scattering and/or absorption by the interface which could lead to enhanced spectral photocurrent if scattering by the interface dominates the extinction spectra. While, the measured photocurrent of a-Si:H thin films deposited on these single- and double- plasmonic interfaces has shown an overall decrease, significant enhancement of photocurrent of a-Si:H is detected near the low energy edge of the bandgap (600–700 nm). These results correlate well with the broadening in the extinction spectra of the interfaces and are interpreted in terms of enhanced absorption of light by a-Si:H thin films due to enhanced scattering by the plasmonic interfaces in that region.

In the third concept, I merged the effects of Al:ZnO surface texturing and AgNPs plasmonics in a single light-trapping interface to investigate their combined light trapping efficiency on a-Si:H thin film. I fabricated plasmonic active interfaces consisting of AgNPs on flat and textured Al:ZnO for use at the front surface of thin film solar cells. I have shown that outstandingly high transmittance haze is achieved by using a single step HCl surface texturing of Al:ZnO and demonstrate Ag dewetting on flat and textured Al:ZnO surfaces upon annealing at 200 °C and 300 °C. The results show that Al:ZnO layers textured by HCl only may provide from 2- to 3-fold enhanced diffuse transmittance over the entire solar spectrum. Optical response of these plasmonic interfaces clearly displays plasmonic resonances in the visible and near infrared regions of the solar spectrum. Light scattered by these interface is optimized by placing a thin SiO_2 spacer layer between AgNPs and a-Si:H absorber layer. The extinction spectra of a-Si:H thin films depostied on these plasmonic interfaces indicate that the AgNPs embedded in SiO_2 significantly enhance absorption at energies close to the band gap of a-Si:H. Surface texturing by wet etching of Al:ZnO combined with AgNP produces the highest optical extinction of a-Si:H thin film at the band edge. Furthermore, the measured spectral photocurrent in a-Si:H shows a clear increase not only at AgNPs resonance wavelength but over the entire wavelength range. This dramatic enhancement in photocurrent response of a-Si:H on textured Al:ZnO with AgNPs in a single light tapping interface is due to the enhanced forward scattering of light into a-Si:H. The textured Al:ZnO surface scatters light obliquely providing another chance for coupling light to a-Si:H. But AgNPs do randomize the incident light in various angles instead of just scattering obliquely in one direction. The plasmonic concentration of light induced by AgNPs near textured AZO increases the scattering into solar cell and thus the absorption enhancement.

In the fourth concept, I have investigated the effect of SiNx dielectric spacer layer thickness and the position of AgNPs plasmonic interfaces on the scattering capacities of AgNPs into a-Si:H as thus on light absorption in a-Si:H. By examining the spectral photocurrent of a-Si:H deposited on two different average AgNPs sizes and separated by various SiNx spacer layer thicknesses, I have placed an upper limit of the optimum dielectric spacer layer thickness of 30 nm thick SiNx for maximum spectral photocurrent enhancement as well as I have placed a lower limit of ~100 nm on the average particle size used in the interfaces. Both optical extinction and spectral photocurrent results recorded in a-Si:H thin films with plasmonic interfaces integrated to the rear or at the front surface with the same 30 nm thick SiNx suggest that the proper position for plasmonic interface is to the rear of the absorber.

Finally, I have studied the effect of SiO_2 dielectric spacer layer thickness on the excitation of LSP resonance of AgNPs fabricated on top of c-Si wafer with different SiO_2 thicknesses. The lowest total reflectance is obtained for AgNPs fabricated on 49.2 nm SiO_2 which suggests that at this particular SiO_2 thickness, a significant fraction of the incident light is scattered into Si absorber. I have found that the LSP resonance of AgNPs is highly dependent on the spacer layer thickness. Increasing the oxide thickness from native oxide to 18.1 blue shifts the LSP resonance due to change in the embedding medium from Si to SiO_2. AgNPs fabricated on oxides with thicknesses larger than 18.1 nm shift into red due to the change is the fraction of embedding medium between SiO_2 and air.

REFERENCES

[1] Jager-Waldau A., PV Status Report, Scientific and Policy Report by the Joint Research Center of the European Commission, 2013.

[2] Franuhofer Institute for Solar Energy (ISE), Annual Photovoltaics Report 2014.

[3] Green M. A., Emery K., King D.L., Hishikawa Y., Warta, W."Solar Cell Efficiency Tables (version 28)", Progress in Photovoltaics: Research and Applications, 14, 455-461 (2006).

[4] Spear W., Le Comber P., "Electronic properties of substitutionally doped amorphous Silicon", Philosophical Magazine, 33, 935–949 (1976).

[5] Carlson D. E., Wronski C. R, "Amorphous silicon solar cell", Applied Physics Letters, 28, 671–673 (1976).

[6] Le Comber P., Spear W., Ghaith A., "Amorphous silicon field effect device and possible applications", Electronic Letters, 15, 179–181 (1979).

[7] Sawada T., Koi Y., Sasaki T., Yoshimi M., Goto M., Yamamoto K., US patent, 2006/0174935, (2006).

[8] Matsui T., Bidiville A., Sai H., Suezaki T., Matsumoto M., Saito K., Yoshida I., Kondo M., presented at the 6th World PVSEC, Kyoto, 2014

[9] Sai H., Matsui T., Koida T., Kondo M., Nakao S., Takeuchi Y., Katayama H., Yoshida I., presented at the 6th World PVSEC, Kyoto, 2014.

[10] Boccard M., Despeisse M., Escarre J., Niquille X., Bugnon G., Hanni S., Bonnet-Eymard M., Meillaud F., Ballif C., presented at the 40th IEEE PVSC, Denver, 2014

[11] Kim S., Chung J.-W., Lee H., Park J., Heo Y., Lee H.-M., "Remarkable progress in thin-film silicon solar cells using high-efficiency triple-junction technology", Solar Energy Materials and Solar Cells, 119, 26–35 (2013).

[12] Feltrin A., Freundlich A., "Material considerations for terawatt level deployment of photovoltaics", Renewable Energy, 33(2), 180 (2008).

[13] Yang J., Banerjee A., Guha S., "Amorphous silicon based photovoltaics—from earth to the "final frontier"", Solar Energy Materials and Solar Cells, 78, 597 (2003).

[14] Tsai C.-Y., Tsai C.-Y., Nanomater J., *http://dx.doi.org/10.1155/2014/ 809261*, (2014).

[15] Applied Materials press release, 20/3/2012, http://www.appliedmaterials.com.

[16] Delft University MOOC, Solar Energy, ET. .3034TU, https://www.edx.org/school/delftx

[17] Green M.A., Emery K., Hishikawa Y., Warta W., Dunlop E. D., "Solar cell efficiency tables (Version 45)", Progress in Photovoltaics: Research and Applications, 22, 701–710 (2014).

[18] Deng X., Schiff E.A., "Amorphous Silicon-based Solar Cells", Handbook of Photovoltaic Science and Engineering from Antonio Luque and Steven Hegedus, John Wiley & Sons, Chichester 505-565 (2003).

[19] Shah, A., Thin-Film Silicon Solar Cells, EPFL Press, Italy, (2010).

[20] Bennett M. S., Rajan K., presented at the 20th IEEE PVSC (Las Vegas, 1988).

[21] Haug F. -J., Ballif C., "Light management in thin film silicon solar cells", Energy and Environmental Science, 8, 824–837 (2015).

[22] Staebler D. L., Wronski C. R., "Reversible conductivity changes in discharge-produced amorphous Si", Applied Physics Letters, 31, 292-294 (1977).

[23] Smirnov V., Reynolds S., Finger F., Carius R., Main C., "Metastable effects in silicon thin films: atmospheric adsorption and light-induced degradation", Journal of Non-Crystalline Solids, 352:1075–1078 (2006).

[24] Atrel A. C., García-Etxarri A., Alaeian H., Dionne J. A., “Toward high-efficiency solar upconversion with plasmonic nanostructures”, Journal of Optics, 14, 024008 (2012).

[25] Kupich M., Grunsky D., Kumar P., Schroder B., “Preparation of microcrystalline single junction and amorphous–microcrystalline tandem silicon solar cells entirely by hot-wire CVD”, Solar Energy Materials and Solar Cells, 81:141–146 (2004).

[26] Zacharias M., Heitmann J., Scholz R., Kahler U., Schmidt M., Blasing J., “Size-controlled highly luminescent silicon nanocrystals: a-SiO/SiO2 superlattice approach”, Applied Physics Letters, 80, 661–663 (2004)

[27] Di D., Perez-Wurfl I., Conibeer G., Green M. A., “Formation and photoluminescence of Si quantum dots in SiO2/Si3N4 hybrid matrix for all-Si tandem solar cells”, Solar Energy Materials and Solar Cells, 94, 2238–2243 (2010).

[28] Nozik A. J., “Quantum dot solar cells”, Physica E, 14, 115–120 (2002).

[29] Beard M. C., Knutsen K. P., Yu P., Luther J. M., Song Q., Metzger W.K., Ellingson R. J., Nozik A. J., “Multiple exciton generation in colloidal silicon nanocrystals”, Nano Letters, 7(8), 2506–2512 (2007).

[30] Gangopadhyay U., Kim K., Mangalaraj D., Yi J., “Low cost CBD ZnS antireflection coating on large area commercial monocrystalline silicon solar cells”, Applied Surface Science, 230, 364–370 (2004).

[31] Soderstromn K., Haug F. J., Escarre J., Pahud C., Biron R., Ballif C., “Highly reflective nanotextured sputtered silver back reflector for flexible high-efficiency n–i–p thin-film silicon solar cells”, Solar Energy Materials and Solar Cells, 95, 3585–3591 (2011).

[32] Ghannam M. Y., Abouelsaood A. A., Alomar A. S., Poortmans J., “Analysis of thin-film silicon solar cells with plasma textured front surface and multi-layer porous silicon back reflector”, Solar Energy Materials and Solar Cells, 94, 850–856 (2010).

[33] Campbell P., Green M. A., “Light trapping properties of pyramidally textured surfaces”, Journal of Applied Physics, 62, 243–249 (1987).

[34] Müller J., Rech B., Springer J., Vanecek M., “TCO and light trapping in silicon thin film solar cells”, Solar Energy, 77, 917–930 (2004).

[35] Franken R. H, Stolk R. L, Li H., Van Der Werf C. H. M., Rath J. K., Schropp R. E. I., “Understanding light trapping by light scattering textured back electrodes in thin film n-i-p-type silicon solar cells”, Journal of Applied Physics, 102, 014503 (2007).

[36] Owen J. I, Hüpkes J., Zhu H., Bunte E., S. Pust S. E., “Novel etch process to tune crater size on magnetron sputtered ZnO:Al”, Physica Status Solidi A, 208, 109-113 (2011).

[37] Lu W. L, Huang K. C., Yeh C. H., CHung C. I., Houng M. P., “Investigation of textured Al-doped ZnO thin films using chemical wet-etching methods”, Materials Chemistry and Physics, 127, 358-363 (2011).

[38] Bunte E., Zhu H., Hüpkes J., Owen J., “Novel texturing method for sputtered zinc oxide films prepared at high deposition rate from ceramic tube targets”, EPJ Photovoltaics, 2, 20602 (2011).

[39] Go B. -N., Kim Y. D., Oh K. S., Kim C., Choi H. -J., Lee H., “Improved conversion efficiency of amorphous Si solar cells using a mesoporous ZnO pattern”, Nanoscale Research Letters, 9, 486 (2014).

[40] Iida H., Shiba N., Mishuku T., Ito A., Karasawa H., Yamanaka M., Hayashi Y., “High efficiency a-Si:H p-i-n solar cell using a SnO2/glass substrate”, IEEE Electron Device Letters, 3, 114–115 (1982).

[41] Sahraei N., Peters M., Venkataraj S., Aberle A., Calnan S., Ring S., Stannowski B., Schlatmann R., Stangl R., “Thin-film a-Si:H solar cells processed on aluminum-induced texture (AIT) glass superstrates: prediction of light absorption enhancement”, Applied Optics, 54, 4366–4373 (2015).

[42] Berginski M., Hüpkes J., Reetz W., Rech B., Wuttig M., “Recent development on surface-textured ZnO:Al films prepared by sputtering for thin-film solar cell application”, Thin Solid Films, 515, 5836-5841 (2008).

[43] Kluth O., Rech B., LHouben L., Wieder S., Schöpe G., Beneking C., Wagner H., Löffl A., Schock H. W., “Texture etched ZnO:Al coated glass substrates for silicon based thin film solar cells”, Thin Solid Films, 351, 247-253 (1999).

[44] Müller J., Schöpe G., Kluth O., Rech B., Sittinger V., Szyszka B., Geyer R., Lechner P., Schade H., Ruske M., Dittmar G., Bochem H. -P., “State-of-the-art mid-frequency sputtered ZnO films for thin film silicon solar cells and modules”, Thin Solid Films, 442, 158-162 (2003).

[45] Yablonovitch E., Cody G. D, “Intensity enhancement in textured optical sheets for solar cells”, IEEE Transactions on Electronic Devices, 29, 300-305 (1982).

[46] Pillai S., Green M. A., “Plasmonics for photovoltaic applications”, Solar Energy Materials and Solar Cells, 94, 1481–1486 (2010).

[47] Trupke T., Green M.A., Wurfel P., “Improving solar cell efficiencies by up-conversion of sub-bandgap light”, Journal of Applied Physics, 92, 4117 (2002).

[48] Temple T. L., Mahanama G. D. K., Reehal H. S., Bagnall D. M., “Influence of localized surface Plasmon excitation in silver nanoparticles on the performance of silicon solar cells”, Solar Energy Materials and Solar Cells, 93, 1978–1985 (2009).

[49] Atwater H. A., Polman A., “Plasmonics for improved photovoltaic devices”, Nature Materials, 9, 205–213 (2010).

[50] Pillai S., Catchpole K. R., Trupke T., Green M. A., “Surface plasmon enhanced silicon solar cells”, Journal of Applied Physics, 101, 093105 (2007).

[51] Schaadt D. M., Feng B., Yu E. T., “Enhanced semiconductor optical absorption via surface plasmon excitation in metal nanoparticles”, Applied Physics Letters. 86, 063106 (2005).

[52] Stuart H. R., Hall D. G., “Island size effects in nanoparticles enhanced photodetectors”, Applied Physics Letters, 73, 3815–3817 (1998).

[53] Eminian C., Haug F. J., Cubero O., Niquille X., Ballif C., “Photocurrent enhancement in thin film amorphous silicon solar cells with silver nanoparticles”, Progress in Photovoltaics, 19, 260 (2011).

[54] Ho C., Yeh D., Su V., Yang C., Yang P., Pu M., Kuan C., Cheng I., Lee S., “Plasmonic multilayer nanoparticles enhanced photocurrent in thin film hydrogenated amorphous silicon solar cells”, Journal of Applied Physics, 112, 023113 (2012).

[55] Redfield D., “Multiple-pass thin-film silicon solar cell”, Applied Physics Letters, 25(11), 647-648 (1974).

[56] Green M. A., Zhao J., Wang A., Wenham S. R., “Very high efficiency silicon solar cells-science and technology”, IEEE Transactions on Electron Devices, 46, 1940–1947 (1999).

[57] Taguchi M., Yano A., Tohoda S., Matsuyama K., Nakamura Y., Nishiwaki T., Fujita K., Maruyama E., “24.7% Record Efficiency HIT Solar Cell on Thin Silicon Wafer”, EEE Journal of Photovoltaics, 4, 96-99 (2014).

[58] Fang X., Li Y., Wang X., Ding J., “Ultrathin interdigitated back-contacted silicon solar cell with light-trapping structure of Si nanowire arrays”, Solar Energy, 16, 100-107 (2015).

[59] Lin C.-C., Chuang Y.-J., Sun W.-H., Cheng C. Chen Y.T., Chen Z.-L., Chien C.-H., Ko F.-H., “Ultrathin single-crystalline silicon solar cells for mechanically flexible and optimal surface morphology designs”, Microelectronic Engineering, 145, 128-132 (2014).

[60] Yu K. J., Gao L., Park J. S., Lee Y. R., Corcoran C. J., Nuzzo R. G., Chanda D., Rogers J. A., “Light trapping in ultrathin monocrystalline silicon solar cells”, Materials Views, 3, 1401-1406 (2013).

[61] Yang Y., Pillai S., Mehrvarz H., Green M. A., “Plasmonic degradation and the importance of over-coating metal nanoparticles for a plasmonic solar cell”, Solar Energy Materials and Solar Cells, 122, 208-216 (2014).

[62] Moulin E., Paetzold U. W., Kirchhoff J., Bauer A., Carius R., “Study of detached back reflector designs for thin-film silicon solar cells”, Physica Status Solidi (RRL)-Rapid Research Letters, 6, 65-67 (2012)

[63] Deckman H. W., Wronski C. R., Witzke H., Yablonovitch E., “Optically enhanced amorphous silicon solar cells”, Applied Physics Letters, 42, 968–970 (1983).

[64] Fay S., Kroll U., Bucher C., Vallat-Sauvain E., Shah A., “Low pressure chemical vapour deposition of ZnO layers for thin-film solar cells: temperature-induced morphological changes”, Solar Energy Materials and Solar Cells, 86, 385–397 (2005).

[65] Lechner P., Geyer R., Schade H., Rech B., Kluth O., Stiebig H., “Optical TCO properties and quantum efficiencies in thin-film silicon solar cells”, 19th European Photovoltaic Solar Energy Conference, Paris, 1591-1594 (2004).

[66] Bennet J. M., Mattson L., “Introduction to Surface Roughness and Scattering”, Optical Society of America, Washington, DC, 51 (1989).

[67] Schade H., Lechner P., Geyer R., Stiebig H., Rech B., Kluth O., “Texture properties of TCO uniquely determining light trapping in thin-film solar cells”, Proc. 31st IEEE Photovoltaic Specialists Conference, Lake Buena Vista, Florida, 1436-1439 (2005).

[68] Shah A. V., Schade H., Vanecek M., Meier J., Vallat-Sauvin E., Wyrsch N., Kroll U., Droz C., Bailat J., “Thin-film silicon solar cell technology”, Progress in Photovoltaics: Research and Applications, 12, 113-142 (2004).

[69] Faraday M., Philosophical Transactions of the Royal Society, London, (1857).

[70] Mie G., “Beitrage zur Optik truber Medien, speziell kolloidaler Metallosungen”, Ann. Phys., 25, 377-452 (1908).

[71] Tayneli I., Nasser H., Es F., Bek A., Turan R., “Effect of surface type on structural and optical properties of Ag nanoparticles formed by dewetting”, Optics Express, 21, A798-A807 (2013).

[72] Guler U., Turan R., “Effect of particle properties and light polarization on the plasmonic resonances in metallic nanoparticles”, Optics Express, 18, 17322-17338 (2010).

[73] Saleh Z. M, Nasser H., Özkol E., Günöven M., Altuntas B., Bek A., Turan R., “Enhanced optical absorption and spectral photocurrent in a-Si:H by single- and double-layer silver plasmonic interfaces”, Plasmonics 9, 357–365 (2014).

[74] Kreibig U., Vollmer M., Optical properties of metal clusters, Springer, Berlin (1995).

[75] Maier S. A., Plasmonics: Fundamentals and applications, Springer US (2007).

[76] Jackson J. D., Classical Electrodynamics, John Wiley & sons, Inc., New York, NY, 3rd edition (1999).

[77] Spectroscopic Ellipsometry Analyzer-SEA (WinElli3), SEMILAB Semiconductor Physics Laboratory Co. Ltd.

[78] Johnson P. B., Christy R. W., “Optical-constants of noble-metals”, 6, 4370-4379 (1972).

[79] Bohren C. F., Huffman D. R., Absorption and Scattering of light by small particles, John Wiley and Sons, Inc., New York, NY, first edition (1983).

[80] Logan N. A., “Survey of Some Early Studies of the Scattering of Plane Waves by a Sphere”, Proc. IEEE., 53, 773-785 (1965).

[81] Catchpole K. R., Polman A., “Design principles for particle plasmon enhanced solar cells”, Appl. Phys. Lett., 93, 191113 (2008).

[82] Sundararajan S. P., Grady N. K., Mirin N., Halas N. J., “Nanoparticle-induced enhancement and suppression of photocurrent in a silicon photodiode”, Nano Lett., 8, 624-630 (2008).

[83] Mie ScatteringTheory, http://nanophotonics.csic.es

[84] Catchpole K. R., Polman A., “Plasmonic solar cells”, Optics Express, 16, 21793-21800 (2008).

[85] Lim, S. H., “Light scattering into silicon-on-insulator waveguide modes by random and periodic gold nanodot arrays”, Journal of applied physics, 105, 073101 (2009).

[86] Pillai S., Beck F. J., Catchpole K. R., Ouyang Z., Green M. A., “The effect of dielectric spacer thickness on surface plasmon solar cells for front and rear side deposisitions”, J. Appl. Phys., 109, 073105 (2011).

[87] Beck F., Catchpole K. R., Polman A., “Red-shifting the surface plasmon resonance of silver nanoparticles for light trapping in solar cells”, In Mater. Res. Soc. Symp. Proc. Vol., volume 1101. Materials Research Society conference, San Francisco, 2008.

[88] Drexhage K. H., “Influence of dielectric interface on fluorescence decay time”, Journal of Luminescence, 1-2, 693-701 (1970).

[89] Beck F. J., Mokkapati S., Polman A., Catchpole K. R., “Asymmetry in light-trapping by plasmonic nanoparticle arrays located on the front or on the rear of solar cells”, Appl. Phys. Lett., 96, 033113 (2010).

[90] Nasser H., Saleh Z. M., Özkol E., Günoven M., Bek A., Turan R., “Fabrication of Ag nanoparticles embedded in Al:ZnO as potential light trapping plasmonic interface for thin film solar cells”, Plasmonics, 8, 1485-1492 (2013).

[91] Nasser H., Özkol E., Bek A., Turan R., “High-haze nature of textured Al:ZnO with Ag nanoparticles for light management in thin film solar cells”, Optical Materials Express, 5, 1147-1155 (2015).

[92] Borra M. Z., Güllü S. K., Es F., Demircioğlu O., Günöven M., Turan R., Bek A., “A feasibility study for controlling self-organized production of plasmonic enhancement interfaces for solar cells,” Appl. Surface Science, 318, 43-50 (2013).

[93] Özkol, E., Modeling and optimization of PECVD Processes and Equipment Used for Manufacturing Thin Film Photovoltaic Devices, PhD Thesis, Middle East Technical University (2015).

[94] Sittinger V., Ruske F., Werner W., Szyszka B., Rech B., Hüpkes J., Schöpe G., Stiebig H., “Al:ZnO films deposited by in-line reactive AC magnetron sputtering for a-Si:H thin film solar cells,” Thin Solid Films, 496, 16-25 (2006).

[95] Willemen J. A., Modelling of Amorphous Silicon Single- and Multi-Junction Solar Cells, Ph.D thesis, Delft University of Technology (1998).

[96] Carius R., Finger F., Backhausen U., Luysberg M., Hapke P., Otte M., Overhof H., “Electronic properties of microcrystalline silicon,” Mat. Res. Soc. Symp. Proc., 467, 283-294 (1997).

[97] Doyle J. R., Doughty D. A., Gallagher A., “Silane dissociation products in deposition discharges,” Journal of Applied Physics, 68, 4375-4384 (1990).

[98] Es F., Fabrication and Characterization of Single Crystalline Solar Cells, Master Thesis, Middle East Technical University (2010).

[99] Würfel P., Physics of Solar Cells from Basic Principles to Advanced Concept, Wiley-VCH (2009).

[100] Poortmans J., Arkhipov V., Thin Film Solar Cells, Fabrication, Characterization and Applications, , John Wiley and Sons, Ltd (2006).

[101] Fujiwara H., Spectroscopic ellipsometry: principles and applications, Wiley, (2007).

[102] Abdellaoui T., Bennaceur J., Chtourou R., “Effect of nanostructured porous n+ GaAs substrates on the energy band gap of nanocrystalline TiO2 thin films analyzed by spectroscopic ellipsometry,” Physica E, 43, 239-247 (2010).

[103] Jellison G. E., Modine F. A., “Parameterization of the optical functions of amorphous materials in the interband region,” Applied Physics Letters, 69, 371 (1996).

[104] Lükermanna B., Heinzmanna U., Stiebig U., “Plasmon induced NIR response of thin-film a-Si:H solar cells,” Proc SPIE, 8471, 84710S-84711S (2012).

[105] Nasser H., Saleh Z. M., Ozkol E., Bek A., Turan R., “Advanced light trapping interface for a-Si:H thin film,” Physica Status Solidi (c), In Press (2015).

[106] Schmid M., Klenk R., Lux-Steiner M. Ch., Topič M., Krč J., “Modeling plasmonic scattering combined with thin-film optics,” Nanotechnology, 22, 025204 (2011).

[107] Sardana S. K., Chava V. S. N., Thouti E., Chander N., Kumar S., Reddy S. R., Komarala V. K., “Influence of surface plasmon resonances of silver nanoparticles on optical and electrical properties of textured silicon solar cell,” Appl. Phys. Lett. 104, 073903 (2014).

[108] Hugonin J. P., Lalanne P., Reticolo software for grating analysis (Orsay, Institut d'Optique Paris (2005).

[109] Johnson P. B., Christy R. W., “Optical Constants of the Noble Metals,” Phys. Rev., B6, 4370 (1972).

[110] SF X., WY H., JY Y., “Melting behaviors of nanocrystalline Ag,” J. Phys Chem, B109:20339 (2005).

[111] Moulin E., Sukmanowski J., Luo P., Carius R., Royer F. X., Stiebig H., “Improved light absorption in thin-film silicon solar cells by integration of silver nanoparticles,” J Non-Cryst Solids, 354, 2488–2491(2008).

CURRICULUM VITAE

HISHAM NASSER

Academic Affiliation: Micro and Nanotechnology Graduate Program of Natural and Applied Sciences (MNT) and
The Center for Solar Energy Research and Applications (GÜNAM), Middle East Technical University

Date/Place of Birth: 19.01.1985 / Lebanon

Postal Address: ODTÜ, Fizik Bölümü, Z-14, 06800, Ankara-Turkey

Phone: +90-312-210-5076

E-mail: hisham.nassser@yahoo.com

EDUCATION

2015 **Middle East Technical University, Turkey**

PhD-Micro and Nanotechnology Graduate Program (CGPA:4.00/4.00, High Honor Student)

2010 **Middle East Technical University, Turkey**

MSc-Physics (CGPA:3.57/4.00, High Honor Student)

2008 **Middle East Technical University, Turkey**

BSc-Physics (GPA:3.23/4.00, Honor student)

SUMMER SCHOOLS

The NATO Science and Security Programme-Advanced Study Institute (ASI), Nanomaterials and Nanoarchitectures workshop and summber school consisting of 40 lectures given by distinguished scientists in the field of Nanoscience. Cork, Ireland, 30th June-7th July 2013

WORK EXPERIENCE

Institution	Title	Dates
METU, Physics Dept, GÜNAM	Project Specialist	2015-...
METU, Physics Dept, GÜNAM	Research Assistant	2008-…

AREAS OF EXPERTISE

Light trapping in amorphous and wafer-based Si, and Si Heterojunction solar cells. Surface texturing and plasmonic metal nanoparticles. Non-linear optical behavior of multi-layered metal nanoparticles. Solid state electronic devices. Semiconductor engineering Opto-electronic characterization of various semiconductors and metals used in solar cell applications. Spectroscopic Ellipsometry (SE) and Scanning Electron Micrsoscope (SEM)

PROFESSIONAL EXPERIENCE

2010-... **The Center for Solar Energy Research and Applications (GÜNAM)**

Fabrication and characterization (optical and electrical) of thin film amorphous silicon solar cells and mono crystalline silicon solar cells, Light trapping in amorphous and wafer-based Si, and Si Heterojunction solar cells. Surface texturing and plasmonic metal nanoparticles. Optical and electronical characteriazations of various semiconductors and metals used in solar cell applications, Photo-Lithography, ultraviolet-visible spectroscopy (UV-

Vis), profilometry, Raman Spectroscopy, energy-dispersive X-ray spectroscopy (EDX), atomic force microscopy (AFM), optical spectroscopy, conductivity measurements, X-ray diffraction spectroscopy (XRD), grazing incidence X-ray diffraction spectroscopy (GIXRD). Principal superuser of Spectroscopic Ellipsometry (SE) and Scanning Electron Micrsoscope (SEM) instruments. Physical vapor deposition (PVD), Sputtering.

2008-2010 **Department of Physics,Middle East Technical University, Turkey**

Thermally Stimulated Current (TSC) measurement of traps distribution for some quaternary layered single crystals

PUBLICATIONS IN JOURNALS

1. **H. Nasser,** F. Es, A. Bek, M. Can, O. Gulseren, R. Turan, Effect of SiO_2 dielectric spacer layer on the excitation of Localized Surface Plasmons of Silver Nanoparticle for Potential Integration in cSi Solar Cells. (Manuscript under preparation)
2. M. Saleh, **Hisham Nasser**, Engin Özkol, Mete Günöven, Kurtuluş Abak, Sedat Canli, Alpan Bek, Raşit Turan. Spacer layer position and thickness for dramatic enhancement of photocurrent in a-Si:H due to Ag plasmonic interfaces. (Under Review, Journal of Nanoparticles Research)
3. **Hisham Nasser**, Zaki M. Saleh, Engin Özkol, Alpan Bek, Raşit Turan, Advanced light trapping interface for a-Si:H thin film, Physics Status Solidi (c), 2015, **Accepted**, *In Press*
4. Zeynep Demircioğlu, Engin Ozkol, **Hisham Nasser**, and Raşit Turan, Low termperature aluminum doped zinc oxide thin film deposition on ultra-thin flexible glass and PET substrates by RF magnetron sputtering, Physics Status Solidi (c), 2015, **Accepted**, *In Press*

5. Mustafa Ünal, **Hisham Nasser**, Mete Günöven, Ilkay Sökmen, Aydın Tankut, and Raşit Turan, Effect of aluminum thickness and etching time of aluminum induced texturing process on soda lime glass substrates for thin solar cell applications, Physics Status Solidi (c), 2015, **Accepted**, *In Press*
6. Zaki M. Saleh, **Hisham Nasser**, Engin Özkol, Alpan Bek, Raşit Turan, Dependence of enhancement of photocurrent in a-Si:H on the position and thickness of SiNx spacer layer. (Under Review, Physica Status Solidi (a))
7. **Hisham Nasser**, Engin Özkol, Alpan Bek, Raşit Turan. High-haze nature of textured Al:ZnO with Ag nanoparticles for light management in thin film solar cells. Optical Materials Express (2015), Vol. 5. 1147-1155
8. Zaki M. Saleh**, Hisham Nasser**, Engin Ozkol, Mete Gunoven, Alpan Bek, Rasit Turan. Enhanced optical absorption and spectral photocurrent in a-Si:H by single- and double-layer silver plasmonic interfaces. Plasmonics (2014) 9:357-365
9. **H. Nasser**, Z. M. Saleh, E. Ozkol, M. Gunoven, A. Bek, R. Turan. Fabrication of Ag nanoparticles embedded in Al:ZnO as potential light-trapping plasmonic interface for thin film solar cells, Plasmonics (2013) 8:1485–1492, *Selected as a Feature article at LabScholars, http://labscholars.com/item/49247*
10. I. Tanyeli, **H. Nasser**, F. Es, A. Bek, R. Turan. Effect of surface type on structural and optical properties of Ag nanoparticles formed by dewetting. Optics Express (2013) Vol. 21, No. S5
11. T. Yıldırım**, H. A. Nasser** and N.M. Gasanly (2010), Determination of trapping center parameters of Tl2Ga2S3Se layered crystals by thermally stimulated current measurements, International Journal of Modern Physics B (2010) Vol. 24:2149-2161

REFEERED CONFERENCE PAPERS

International Conferences

C1. Mustfa Ünal, **Hisham Nasser**, Mete Günöven, İlkay Sökmen, Raşit Turan. Aluminum induced glass texturing process for thin film solar cell application.

Abstract accepted in the 31st European PV Solar Energy Conference and Exhibition (EU PVSEC), Hamburg, Germany, 14 Sep- 18 Sep 2015

C2. Mona Zolfaghari Borra, **Hisham Nasser**, Bilge Can Yildiz Karakul, Mehmet Emre Tasgin, Rasit Turan, Alpan Bek. Nonlinear optical response of double plasmonic interface for potential use in solar cells. Abstract accepted in the 31st European PV Solar Energy Conference and Exhibition (EU PVSEC), Hamburg, Germany, 14 Sep- 18 Sep 2015

C3. **Hisham Nasser**, Zaki M Saleh, Alpan Bek, Raşit Turan. Plasmonic Large Area Thin Film Interfaces for Potential Solar Cell Applications. ***Oral*** Presentation, TMS Middle East - Mediterranean Materials Congress on Energy and Infrastructure Systems (MEMA 2015), Doha, Qatar 2015

C4. **Hisham Nasser**, Engin Ozkol, Alpan Bek, Raşit Turan. High Haze Nano-Textured Aluminum doped Zinc Oxide with Plasmonic Silver Nanoparticles for Enhanced Optical Absorption and Photocurrent of a-Si:H thin film. TMS Middle East - Mediterranean Materials Congress on Energy and Infrastructure Systems (MEMA 2015), Doha, Qatar 2015, **Best Poster Award**

C5. **Hisham Nasser**, Firat Es, Alpan Bek, Mehmet Can, Oguz Gulseren, Rasit Turan. Effect of SiO_2 Dielectric Spacer Layer on the Excitation of Localized Plasmon Resonance of Silver Nanoparticles for Potential Integration in c-Si Solar Cells. ***Oral*** Presentation, European Materials Research Society (E-MRS Spring Meeting), Syposia Y, Lille France 2014

C6. Zaki M. Saleh, **Hisham Nasser**, Mete Gunoven, Engin Ozkol, Burju Altuntas, Alpan Bek, Rasit Turan. Enhancement of optical absorption in a-SI:H films by silver nanoparticle plasmonic interface. 28th European PV Solar Energy Conference and Exhibition (EU PVSEC) Proceedings (2013) P. 371 - 374

C7. **H. Nasser**, E. Ozkol, M. Gunoven, F. Es, R. Turan. Influence of the underlying SiO_2 spacer on the properties of silver nanoparticles for potential application in solar cell. 28th European PV Solar Energy Conference and Exhibition (EU PVSEC 2013), Paris, France, 30 Sep-04 Oct 2013 P. 109

C8. E. Ozkol, G. Nogay, **H. Nasser**, G. Yilmaz, H. Cansever, S. Kincal, M. Gunes, R. Turan. Effect of plasma properties on doping a-Si in a capacitively coupled plasma system. 28th European PV Solar Energy Conference and Exhibition (EU PVSEC 2013), Paris, France, 30 Sep-04 Oct 2013 P. 215

C9. Z. M. Saleh, **H. Nasser**, M. Gunoven, E. Ozkol, P. Altuntas, A. Bek and R. Turan. Enhacement of optical absorption in a-Si:H films by silver nanoparticle plasmonic interface. 28th European PV Solar Energy Conference and Exhibition (EU PVSEC 2013), Paris, France, 30 Sep-04 Oct 2013 P. 111

C10. **H. Nasser**, R. Turan. Variations in the optical response of silver nanoparticles self-assembled on silicon wafer covered with different SiO2 spacer layer thickness. NATO-Advanced Study Institute “Nanomaterials and Nanoarchitectures (NATO ASI), Cork, Ireland, 30 June-07 July 2013

C11. Irem Tanyeli, **Hisham Nasser**, Firat Es, Alpan Bek, Rasit Turan. Effect of surface type on structural and optical properties of Ag nanoparticles formed by dewetting. Conference Proceedings European Materials Research Society (E-MRS 2012 Spring Meeting), Symposia N and Symposia O

C12. **Hisham Nasser**, Irem Tanyeli, Firat Es, Engin Ozkol, Alpan Bek, Rasit Turan. Plasmonic Light Scattering from Ag Nanoparticles Fabricated on ITO and ZnO Thin Films. Photovoltaic Technical Conference, Aix En Province, France 06-08 June 2012, P. 45

C13. Irem Tanyeli, **Hisham Nasser**, Firat Es, Alpan Bek, Rasit Turan. Formation of and Light Scattering from Plasmonic Ag Nanoparticles on Solar Cell Thin Film Materials. European Materials Research Society (E-MRS 2012 Spring Meeting), Strasbourg, France, 14-18 May 2012, p. 118

C14. T. Yildirim**, H. Nasser**, N. M. Gasanly and H. Ozkan. Traps distribution in TlGaSeS single crystals from thermally stimulated current measurements. Second International Conference Scientific-Technical Progress and Modern Aviation, Baku, Azerbaijan, 10-14 February 2009, p. 177-179

National Conferences

C15. **H. Nasser**, E. Özkol, Z. Saleh, A. Bek, R. Turan, Textured Al:ZnO with Ag Nanoparticles for Enhanced Photon Absorption of a-Si:H Thin Film. Nano TR11, Ankara, 22-25 June, 2015, PS3/P66

C16. Z. Demircioğlu, E. Özkol, **H. Nasser**, R. Turan, Comparison of Optical and Electrical Properties of AZO Thin Films Deposited on PET and Ultra-Thin Glass Substrates by RF Magnetron Sputtering**.** Nano TR11, Ankara, 22-25 June, 2015, PS3/P68

C17. **Hisham Nasser**, Zaki M Saleh, Engin Özkol, Alpan Bek, Raşit Turan, Advanced Light Trapping Interface for a-Si:H Thin Film. 3rd Turkish Solar Electricity Conference and Exhibition (SolarTR-3), Ankara, Turkey, 27-29 April 2015, P. 49

C18. Mustafa Ünal, **Hisham Nasser**, Mete Günöven, İlkay Sökmen, Raşit Turan, Effect of Aluminum Thickness and Etching Time of Aluminum Induced Texturing Process on Soda Lime Glass Substrate for a-Si:H Solar Cell Applications. ***Oral*** presentation, 3rd Turkish Solar Electricity Conference and Exhibition (SolarTR-3), Ankara, Turkey, 27-29 April 2015, P. 15

C19. Zaki M Saleh, **Hisham Nasser**, Engin Özkol, Sedat Canli, Alpan Bek, Raşit Turan, Dependence of Plasmonics Enhancement of Photocurrent in a-Si:H on the Position and Thickness of Spacer Layer. ***Oral presentation***, 3rd Turkish Solar Electricity Conference and Exhibition (SolarTR-3), Ankara, Turkey, 27-29 April 2015, P. 7

C20. Tahir Çolakoğlu, Engin Özkol, **Hisham Nasser**, Zeynep Demircioğlu, Raşit Turan, Evolution and Elamination of Bubbling Induced Delamination of PECVD Grown Amorphous Silicon Thin Films. 3rd Turkish Solar Electricity Conference and Exhibition (SolarTR-3), Ankara, Turkey, 27-29 April 2015, P. 44

C21. Engin Özkol, **Hisham Nasser**, Zeynep Demircioğlu, Mete Günövn, Raşit Turan, Characterization and Optimization of Aluminum Dope Zinc Oxide (AZO) Thin Films Deposited via RF Magnetron Sputtering Technique. 3rd Turkish Solar

Electricity Conference and Exhibition (SolarTR-3), Ankara, Turkey, 27-29 April 2015, P. 56

C22. Zeynep Demircioğlu, Engin Özkol, **Hisham Nasser**, Raşit Turan, Low Temperature Aluminum Doped Zinc Oxide (AZO) Thin Film Deposition on Flexible Glass and PET Substrates by RF Magnetron Sputtering. 3rd Turkish Solar Electricity Conference and Exhibition (SolarTR-3), Ankara, Turkey, 27-29 April 2015, P. 66

C23. **Hisham Nasser**, Engin Özkol, Alpan Bek, Rasit Turan, Extreme Spectral Photocurrent Enhancement of a-Si:H Thin Film by Exploiting the Scattering Potentials of Textured Al:ZnO and Silver Plasmonic Nanoparticles. ***Oral*** presentation, The 29th Şişecam Glass Symposium, Kadir Has University Cibali Campus, Istanbul, 7 November 2014

C24. Mustafa Ünal, **Hisham Nasser**, Raşit Turan, Aluminum Induced Texturing of Soda-Lime Glass Substrates for Thin Film Solar Cells. ***Oral*** presentation, The 29th Şişecam Glass Symposium, Kadir Has University Cibali Campus, Istanbul, 7 November, 2014

C25. **H. Nasser**, E. Özkol, A. Bek, R. Turan, Optimized Textured Al:ZnO and Silver Nanoparticles as a Single Front Light Trapping Interface for a-Si:H Solar Cells. The Turkish-German Conference on Energy Technologies, METU, Ankara, Turkey, 13-15 October, 2014

C26. **Hisham Nasser**, Fırat Es, Alpan Bek, Mehmet Can, Oguz Gulseren and Raşit Turan, Effect of SiO2 Spacer Layer Thickness on the Optical Response of Silver Nanoparticles Used as a Light Trapping Interface for Thin Film c-Si Solar Cells. IONS-15, Bilkent University, Ankara, Turkey, 2-5 July, 2014

C27. Mustafa Unal, **Hisham Nasser**, Engin Ozkol, Zeynep Demircioglu, Rasit Turan. Aluminum Induced Nanotexturing of Glass Superstrate for Enhanced Photo-response of a-Si:H Thin Film. ***Oral*** Presentation, Nano TR10, Istanbul 2014

C28. Mona Zolfaghariborra, **Hisham Nasser**, İrem Tanyeri, Alpan Bek, Raşit Ruran. Exploring control mechanisms on the self-organized fabrication of Ag nanoparticles for plasmonic solar cells. ***Oral*** Presentation; 20. Yoğun Maddi Fiziği, Izmir Toplantisi, Izmir, Turkey, 05 April 2013, P. S01

C29. İrem Tanyeli, **Hisham Nasser**, Firat Es, Alpan Bek, Raşit Turan. Structural and optical properties of Ag nanoparticles formed by dewetting on various substrates. ***Oral*** Presentation; Solar Electricity Conference and Exhibition (Solar-TR-2), Antalya, Turkey, 07-09 November 2012, P. 56

C30. Engin Özkol, Gizem Nogay, **Hisham Nasser**, Zeynep Demircioğlu, Serkan Kınca. New Cluster PECVD system at GÜNAM. ***Oral*** Presentation; Solar Electricity Conference and Exhibition (Solar-TR-2), Antalya, Turkey 07-09 November 2012, P. 31

C31. T. Yıldırım, İ. Küçük, M. Kabaer, **H. A. Nasser**, İ. Güler, M. Işık, K. Ertürk, N. Hasanli, H. Özkan. Katmanlı Yapıya Sahip Yarıiletken Kristallerde Tuzak Dağılımının Modellenmesi. Metal, Yarıiletken ve Oksit Materyallerin Üretilmesinde Kullanilan Sistemler ve Analiz Teknikleri Kongresi (MYOMAT 2009), Eskişehir, Türkiye, 15-16 June 2009, p. 59

C32. T. Yildirim, **H. Nasser**, İ. Kucuk, İ. Guler, M. Isik, H. Özkan and N. Hasanli. Determination of trapping centers parameters and their distribution in Tl2Ga2S3Se layered crystals by thermally stimulated current measurements. 26th International Physics Conference, Bodrum, Turkey, 24-27 September 2009, p. 521

C33. İ. Kucuk, T. Yildirim, M. Isik, **H. Nasser**, N. Hasanli. Katmanlı Yapıya Sahip Yarıiletken Kristallerde İzotermal Azalma Eğrilerinin Modellenmesi. 16. Yoğun Madde Fiziği – Ankara Turkey, 6 November 2009, p. 38